Investigation of Co Decorated N, S Doped Reduced Graphene Oxide (Co/NS-rGO) Catalysts For Oxygen Reduction Reaction (ORR) and NH_3 Electrosynthesis through Nitrate Reduction Reaction (NO_3RR)

by

Kaan Şimşek

A Dissertation Submitted to the
Graduate School of Sciences and Engineering
in Partial Fulfillment of the Requirements for
the Degree of

Master of Science

in

Materials Science and Engineering

KOÇ
ÜNİVERSİTESİ

September 6, 2024

Investigation of Co Decorated N, S Doped Reduced Graphene Oxide (Co/NS-rGO) Catalysts For Oxygen Reduction Reaction (ORR) and NH_3 Electrosynthesis through Nitrate Reduction Reaction (NO_3RR)

Koç University

Graduate School of Sciences and Engineering

This is to certify that I have examined this copy of a master's thesis by

Kaan Şimşek

and have found that it is complete and satisfactory in all respects,
and that any and all revisions required by the final
examining committee have been made.

Committee Members:

_____

Assoc. Prof. Sarp Kaya

_____

Prof. Can Erkey

_____

Prof. Adem Tekin

Date: _____

ABSTRACT

Investigation of Co Decorated N, S Doped Reduced Graphene Oxide (Co/NS-rGO) Catalysts For Oxygen Reduction Reaction (ORR) and NH_3 Electrosynthesis through Nitrate Reduction Reaction (NO_3RR)

Kaan Şimşek

Master of Science in Materials Science and Engineering

September 6, 2024

One of humanity's most challenging problems in our century is enabling sustainable and carbon-zero energy, chemical, and fuel production and minimizing the use of fossil fuel sources to reduce CO_2 emissions and decelerate climate change. Two crucial routes to decarbonize energy consumption are the widespread commercialization of proton exchange membrane fuel cells (PEMFC) for transportation and the environment-friendly NH_3 electrosynthesis. It is essential to understand reaction kinetics, adsorption tendencies, and current performance of feasible catalysts to actualize the use of affordable and high-performance catalysts for oxygen reduction reaction (ORR) at PEMFCs' limiting cathode compartment and to provide a pathway for zero-emission NH_3 electrosynthesis that compensate for NH_3 production of carbon-intensive Haber-Bosch process. Comparably cheap and abundant Co and high-surface-area graphene-based Co decorated N, S Doped Reduced Graphene Oxide (Co/NS-rGO) catalysts with different metal compositions and heat treatments are investigated for NH_3 electrosynthesis through nitrate reduction reaction (NO_3RR) and ORR for their activity and selectivity.

In the first part of the thesis, it is unraveled that the optimum composition of Co enables the formation of ORR-active CoS species and homogenous distribution of Co Single Atoms (SAs) steer the selectivity towards $4e^-$ pathway that is desired for PEMFC and provide the lowest overpotential with the highest current output. With the help of rotating disk electrode (RDE) and rotating ring-disk electrode (RRDE) techniques that eliminate the effect of mass-transfer limitations the number of electrons transferred (n_{e^-}) is measured for Co/NS-rGO as $4e^-$ throughout the studied potential range as of industrial PEMFC catalyst of Pt/C while the 2Co/NS-rGO catalyst that has higher Co composition with CoO species, favored more HO_2^- production. Furthermore, the origin of the catalysts' kinetic activity and the materials' electronic properties are investigated using

electrochemical impedance (EIS) techniques. Co/NS-rGO catalyst that has the highest performance obtained a higher density of states ($D(E_F)$) around the Fermi level for the electroreduction, higher charge carrier density concentration (N_D) and the flatband potential. Also, electrochemical surface area (ECSA) normalized RDE and RRDE figures indicate the maximum utilization of electrochemically active sites for the Co/NS-rGO catalyst, which has the highest charge storage properties detected by EIS capacitive measurement.

In the second part of the thesis, the electrochemical NO_3RR-to-NH_3 activity of NS-rGO and its Co incorporated and/or 900 °C pyrolyzed counterparts are investigated. It is observed that NS-rGO is inclined to generate high amounts of NO_2 while unable to convert NO_3 to NH_3 with high efficiency. On the other hand, pyrolysis facilitates hydrogen evolution reaction (HER) for both metal and non-metal catalysts. Co incorporation is claimed to promote NH_3 yield rate and Faradaic Efficiency (F.E.) significantly at lower overpotentials with higher current outputs. A mechanistic approach using X-ray Absorption Spectroscopy (XAS), EIS, EIS-driven Distribution of Relaxed Species (DRT), and Tafel analysis enabled us to find that the Co/NS-rGO follows a mass transfer limited mechanism. At the same time, Co/NS-rGO 900 is driven by charge transfer limitations and protonation properties. Furthermore, mechanistic studies show that NO_2 desorption plays a significant role in NO_3RR. To modulate and increase NH_3 yield and F.E., a pulsed electrolysis strategy is inherited at both mass-transfer and charge-transfer limited potential regimes. Pulsed electrolysis results show that Co/NS-rGO catalyst with a very high NH_3 yield rate and F.E. for NO_2RR can increase its NH_3 F.E. by two-fold and yield rate by 3-fold through pulsed electrolysis. In contrast, the pulsed strategy facilitates HER and suppresses NH_3 production efficiency for the Co/NS-rGO 900 catalyst.

ÖZETÇE

Kobalt Gömülü Azot ve Kükürt Katkılanmış İndirgenmiş Grafen Oksit (Co/NS-rGO) Katalizörlerin Oksijen İndirgenmesi ve Nitrat İndirgenmesi Reaksiyonları İçin İncelenmesi

Kaan Şimşek

Malzeme Bilimi ve Mühendisliği, Yüksek Lisans

6 Eylül 2024

Çağımızda insanlığın en zorlayıcı problemlerinden birisi sürdürülebilir ve karbon-sıfır enerji, kimyasal ve yakıt üretimini sağlamak ve fosil yakıt kaynaklarının kullanımını azaltarak karbon dioksit salınımını düşürmek ve iklim krizini yavaşlatmaktır. Enerji tüketimini dekarbonize edebilmek için iki önemli yol proton değişim membranı yakıt pillerinin ve çevre dostu amonyak elektrosentezinin yaygın ticarileşmesini sağlamaktır. Katalizörlerin reaksiyon kinetiklerini, bağlanma isteklerini ve akım performanslarını anlamak proton değişim membranı limitleyici kompartmanında olan oksijen indirgenmesi reaksiyonunda kullanılmak için satın alınabilir ve yüksek performanslı katalizörlerin kullanmını sağlamak ve sıfır emisyonlu amonyak elektrosentezini Haber-Bosch sürecini tazmin edebilecek kadar ilerletebilmek adına çok önemlidir. Ucuz ve yaygın kobalt yüksek yüzey alanlı grafen bazlı Co/NS-rGO katalizörlerinin farklı metal kompozisyonlarında ve farklı ısıl işlemlere tabi tutulmuş halleri nitrat indirenmesiyle amonyak elektrosentezi ve oksijen indirgenmesindeki seçicilikleri ve aktiviteleri için test edilmiştir.

Tezin ilk bölümünde, kobaltın optimum kompozisyonunun oksijen indirgenmesi aktif CoS türlerinin ve kobalt tekli atomlarının homojen dağılmasının katalizörün proton değişim membranı yakıt pilleri için de istenen 4 elektron yönünde seçici olduğunun ve en az aşırıgerilim ve en yüksek akım çıkışına sahip olmasını sağladığı görülmüştür. Katı-transferi limitlerini yok eden dönen disk elektrot ve dönen halka-disk electrot tekniklerinin transfer edilen elektron sayısının Co/NS-rGO için çalışılan potensiyal aralığında endüstriyel katalizörler gibi 4 elektrob olduğu bulunmuştur. Aynı zamanda daha çok kobalt içeren ve kobalt oksit içeriği olan 2Co/NS-rGO katalizörlerinin peroksit formasyonuna yol açtığı bulunmuştur. Sonrasında, katalizörlerin kinetik aktivitelerinin

orijinini bulmak için materyallerin elektronik özellikleri elektrokimyasal impedans spektroskopisi teknikleri kullanılarak incelenmiştir. En yüksek performansa sahip Co/NS-rGO katalizörününün Fermi seviyesi etrafında en yüksek durum yoğunluğuna, en fazla yük taşıyıcı yoğunluğuna ve en yüksek düz bant potansiyeline sahip olduğu bulundu. Ayrıca, elektrokimyasal yüzey alanıyla normalize edilen dönen disk elektrot ve dönen halka-disk elektrot deneyleri sonuçlarının normalize edilmeyen halleri gibi yine elektrokimyasal aktif alanlarının maksimum kullanılabilirliğinde olduğu gözlenmiştir. Ayrıca, elektrokimyasal impedans teknikleri Co/NS-rGO katalizörünün kapasitif özelliklerinin en yüksek olduğunu bulmuştur.

Tezin ikinci bölümünde, elektrokimyasal nitrattan amonyağa aktivitesi kobaltlı veya kobaltsız; ısıyla eritilmiş veya eritilmemiş kükürt ve azot katkılı indirgenmiş grafen oksit katalizörleri için incelenmiştir. Bulgular kobaltsız katalizörün nitrit üretimini desteklediği ve nitratı amonyağa dönüştürmekte çok etkin olmadığını göstermiştir. Aynı zamanda, ısıl eritmenin hidrojen oluşumu reaksiyonunu desteklediği ve kobalt gömülmesinin de amonyak seçiciliğini ve verimini arttırdığı gözlenmiştir. Mekanizma yaklaşımı XAS, EIS, DRT modeli ve Tafel nalizinin Co/NS-rGO için katı-transferi limitli bir mekanizmaya sahip olduğunu gösterir. Aynı zamanda, ısıyla iretilmiş kobaltlı katalizörün ise yük transferi limitlemelerinin olduğu ve protonlama özelliklerinin düşük olduğu gözlenmiştir. Üstelik, mekanizma çalışmaları nitrit desorpsiyonunun nitrat indirgenmesinde önemli bir rolü olduğunu gösteriyor. Nitriti modüle etmek ve amonyak verimi ve seçiciliğini arttırmak için, kısa aralıklarla elektroliz stratejisi seçilmiştir katı-transferi limitli ve yük transferi limitli rejimlerde. Kısa aralıklı elektroliz sonuçları çok yüksek amonyak verim hızı ve seçiciliğiyle nitrit indirgenmesini gerçekleştiren Co/NS-rGO katalizörünün nitrat indirgenmesi için amonyak seçiciliğini 2 kat ve verimini 3 kat arttırdığı gözlenmiştir. Fakat, ısıyla eritilmiş kobaltlı katalizör hidrojen oluşumu reaksiyonunu takip etmiş ve amonyak üretimi bastırılmıştır.

TABLE OF CONTENTS

LIST OF TABLES

LIST OF FIGURES

Chapter 1:
INTRODUCTION

1.1 Catalyst Design for the Electrochemical Energy Applications: Co decorated N, S Doped Reduced Graphene Oxide (Co/NS-rGO)

After the Industrial Revolution, people's need for energy increased exponentially, and to meet this demand, high amounts of fossil resources needed to be utilized [1]. The high consumption of fossil fuels has caused a significant increase in CO_2 emissions, which has caused climate change and is threatening the habitats of many living species, including humans. The need for energy increases every day and causes the use of more fossil fuels, which can cause the earth to be unhabitable in the foreseeable future [2]. To prevent these disasters from happening, sustainable energy production needs to be put to use in a rapid, affordable, and effective way in the shortest time. Much industrial and academic research is carried out to balance and limit fossil-fuel-driven systems' use [3], [4]. Recently, electric cars powered by lithium-ion batteries, hydrogen-fueled automobiles with proton exchange membrane fuel cells (PEMFC), and large-scale CO_2 electrolysis to produce $C_XH_YO_Z$ and NH_3 electrosynthesis through N_2 (NRR) and NO_3^- reduction (NO_3RR) are some of the crucial steps to decarbonize energy production [5], [6], [7], [7], [8], [9].

The cost and operability of sustainable energy systems heavily depend on the catalyst design. Pt/C catalysts are used in the performance-limiting compartment of PEMFC systems to supply enough energy for oxygen reduction reaction (ORR) to carry out and ensure system durability [10], [11], [12]. On the other hand, to this day, there is no definitive catalyst for NH_3 electrosynthesis, while the energy-intensive Haber-Bosch process primarily depends on industrial Fe catalysts[13]. It is essential to synthesize durable, cost-effective, high-performance, and selective catalysts to actualize widespread use of these sustainable energy technologies to replace fossil-driven energy production [14], [15].

By definition, catalysts are materials in the surface reaction that happens on the surface without the catalyst remaining unchanged. To enable efficient electrocatalysis with a high yield of the target product, the catalyst must have a high surface area and moieties

that are selective for the desired catalysis process[8], [12]. The catalyst's activity can be evaluated by its number of active sites and the intrinsic activity or turnover frequency of these active sites for the catalysis[16], [17]. A tremendous amount of effort is put into synthesizing high-surface area electrocatalysts that have a significant amount of active sites and active sites that are active for the selective catalysis process such as N sites such as pyridinic N[18], atomically dispersed metal atoms of Pt, Fe, Co in high-surface-area Metal-N-C catalysts[19], [20], catalytic pairs of Metal-S, Metal-P in chalcogenides[21], [22] and tandem electrolysis on core-shell structures of noble and non-noble metals[23], [24].

Graphene is selected as catalyst support to provide a high surface area and enhance the number of active sites[25]. It holds superior properties owing to its unique electronic[26], [27], [28], thermal[29], and optical properties[30]. The high surface area of graphene allows the dispersion of a high amount of nanoparticles or single atoms on its surface[31], [32], [33] and makes an efficient platform for heterogeneous catalysts. It is impossible to actualize large-scale graphene production using methods such as epitaxial growth[34] or mechanical exfoliation of graphite (Scotch tape)[35], which provides single or few-layer graphene[36]. However, the chemical route to synthesize graphene oxide (GO) [36], [37] follows the exfoliation of graphite through strong oxidation and can enable bulk manufacturing of graphene-like materials with defects and oxygen functionalities[38], [39] through reduction. The production of contamination-free GO, i.e., using phosphoric acid to eliminate Mn content61, through chemical reduction, enables graphene production on a bulk scale, and oxygen functionalities in GO enable manipulation and engineering through doping and heat treatment for different applications[40]. Even though the aforementioned superior properties of graphene exist, zero band gap energy or defect-free structure of the material makes it insufficient for energy applications[26], [41]. Also, metal incorporation to pristine graphene is not favored due to weak bonding[42]. When graphene is functionalized upon doping, its open structure, high surface area, conductivity, and stability make it an excellent catalyst support[43], [44]. Properties that can be attained by doping of graphene and other carbon derivatives, i.e., nanotubes and amorphous materials, are investigated primarily with N-doping[45], [46], [47], [48] and multi-heteroatom doping[49] with different elements, such as S[42], [50], [51], P[52], [53], [54] and B[55].

N-doped graphene[45], [56] is thoroughly investigated for the ORR and found to have high activity, durability, and low overpotential during catalysis. N-doping changes the atomic charge distribution on the material[57] and introduces multiple active sites, higher surface area, disorder, and defects, which become anchoring sites for metals[58], [59]. N changes the surface electronic distribution of solely sp^2 hybridized graphene through partial charge difference. During the process, C and N induce partially negative and positive charges ($C^{\delta+}$ $N^{\delta-}$) by C-N bonding[47]. Doping can provide different N active sites, such as pyrrolic, pyridinic, and graphitic N[45]. There is no clear conclusion about the active center for oxygen electroreduction. In many studies, it is proposed that high ORR activity emerges from existing pyridinic N sites[60], [61]. In contrast, Yang et al. claim that electron-donating quaternary N sites are responsible for high ORR activity[62]. Also, carbon atoms adjacent to pyridinic N or sp^2 carbons next to oxide regions are proposed to be active sites for ORR. Since pyridinic N can impact the electronic structure of surrounding atoms, it is claimed to generate more active sites for ORR compared to its counterparts (pyridinic, graphitic N)[18], [63], [64], [65]. According to another report, limiting current density is determined by graphitic N, while the reduction in overpotential and $4e^-$ selectivity is dependent on the presence of pyridinic N.[61]. On the other hand, Li. et al. investigated Cu_xO/N-doped Graphydiyne material enriched with pyridinic, pyrrolic, and graphitic N sites. They found that the synergistic effects between pyridinic N and Cu_xO achieve 85% F.E. with a high NH_3 production rate [66]. Similarly, Zhu et al. introduced that the interactions between pyridinic N and adjacent carbon atoms steer the selectivity towards NH_3 by 99.24 % and enhance the production yield [67].

Even though not as frequently investigated as N-doping, heteroatom doping of graphene materials boosts the kinetics of electrochemical reactions and improves the adsorption abilities of the material[25], [49]. Heteroatom doping involves different S, F, or B atoms studied in different electrochemical processes[50], [52]. The high oxophilic character of S[68] and its ability to form catalytically active metal sulfide species lower the energy barrier for adsorption [69], [70] and subsequent steps of various electrochemical reduction reactions[71], [72]. Surprisingly, while phosphorus is used intensively for high-activity NO_3RR catalysts[21], [73], [74], S is not used as a doping element, or its role for the catalysis is studied for NO_3RR. Although it is not investigated for NO_3RR, N, S doped

carbon-based catalyst and catalyst supports are thoroughly examined for ORR[53], [75]. Doping of graphene with S can introduce additional defects due to its larger atomic size and more stable structure[76], [77]. Opposed to N, the electronegativity difference between S and C is lower, and it is claimed to have a positive effect on the ORR by facilitating oxygen chemisorption[78]. The presence of sulfur is postulated to facilitate the protonation transfer step in ORR. It alleviates the reduction of adsorbed oxygen ($O_{2,aq}$) to superoxide ($O_2^{\bullet-}$), which is claimed to be the rate-determining step of ORR[76], [79]. Also, it is proposed that co-doping of graphene with N and S can present defects, more active sites, asymmetrical charge, and spin density distribution on graphene, which results in higher electrical conductivity[50], [80], [81], [82]. Since the electronegativities of C and S are very close, instead of adjacent C becoming positively charged for N-doped C, S is positively charged through a mismatch in the outermost orbital of S and becomes an active site for the ORR[50], [78]. High ORR activity emerging from S and N co-doped graphene-based catalysts relates to synergistic effects between dopants[50], [76], [83], [84]. It is found that heteroatom doping can also enhance metal/support interactions [85], [86].

Co is a cheap and abundant catalyst and is used in different electrochemical reactions such as oxygen reduction reaction (ORR)[87], [88], oxygen evolution reaction (OER)[89], and carbon dioxide reduction reaction (CO_2RR)[90] thanks to its partially filled d orbital and the improvability of many catalytic sites[91]. Co incorporation to heteroatom-doped graphene matrix is further investigated to increase ORR catalysts' activity and durability[44], [59], [92], [93], [94], [95]. Liang et al. synthesized a Co_3O_4/N-rGO hybrid, where he explained the high ORR activity with the synergistic coupling between Co_3O_4 and N-doped reduced graphene[59]. Yang et al. claimed that both Co-N-G and Co-N, S-G, and Co-N_X sites act as the active sites for the ORR. Higher activity of Co-N and S-G is associated with better mass transport and electron-rich characteristics of N due to the presence of S[92]. Also, it is proposed that metal incorporation to carbon ends up with non-metal ORR active sites. In another study, a metal composite catalyst subjected to heat treatment with impregnation of Co-Fe-N chelate complex is synthesized, showing low overpotential and no degradation in 480 h of continuous fuel cell conditions. It is found that the decomposition of a metal chelate complex during heat treatment accelerates the formation of ORR active N species at lower temperatures[96], [97]. Co

catalysts are extensively used in NO_3^- and NO_2^- reduction reactions as atomically dispersed Co metal-nitrogen-carbon[20] or Co-P catalytic pair[21], Co_3O_4 nanoarray[98], core-shell CoP@Co[74] and Cu/CuOx – Co/CoO phases[99], and Co metallopeptide[98]. Murphy et al. found that despite the high NH_3 F.E. of the Co-N-C catalyst for NO_2RR, the Co-N-C catalyst suffers from low selectivity towards ammonia due to the inability of NO_3^- activation for NO_3RR. Furthermore, they signified the different effects of bulk NO_2^- and locally channeled NO_2 by examining NO_2^- F.E. after NO_3RR and NH_3 yield after NO_2RR, eventually telling that rather than a direct $8e^-$ mechanism for NO_3RR, a complex mechanism might have been driven by the NO_2 desorption[20]. In another article, Ni et al. show that the Co sites in Co-P catalytic pairs favor the activation of NO_3^- and P sites, allowing water disassociation to take place to supply H^+ needed for proton-coupled electron transfer for NO_3RR [21].

Single-atom catalysts (SACs) offer maximum atomic utilization, high activity, selectivity, and stability as an emerging frontier in heterogeneous catalysis. Instead of metallic bonding, SACs form through bonds between metal and heteroatoms on support surfaces[100], [101]. SACs are found to have low overpotential and high activity towards ORR[102], [103], [104]. Yin et al. found out that Co SAs/N-C(900), which has dominant reactive sites of $Co-N_2$ followed near the four-electron pathway and onset potential of 0.881 V[104].

It has been shown recently in operando studies[105], [106] that as claimed active sites, i.e., $Co-N_4$ moieties[105] and Co SACs[106], tend to show higher F.E. for H_2O_2 production via $2e^-$ transfer pathway while $Co-N_2$ moieties favor $4e^-$ mechanism[105]. It can be postulated that $Co-N_2$ moieties and cobalt sulfide species in a catalyst as tandem ORR active sites can accelerate the $4e^-$ mechanism. A theoretical study uses quantum computations that cobalt sulfide surfaces show ORR activity similar to platinum. S^{2-} ions in cobalt sulfide surfaces can be an adsorption site for oxygen, facilitating O-O bond cleavage and initiates $4e^-$ mechanism[107]. Furthermore, for NO_3RR, Ren et al. used a bioinspired approach where they studied Cd single-atom anchored $Mo_2TiC_2T_x$ catalyst to achieve >95% Faradaic efficiency (F.E.) and 48.5 mg h^{-1} cm^{-2} NH_3 yield rate by activating NO_3^- by Mo active center as of nitrate reductase and suppressing HER simultaneously[108]. Murphy et al. utilize a FeMo-N-C atomically dispersed catalyst that follows a cascade NO_3RR pathway through associative and disassociative adsorption of

NO_3^-. They could effectively adsorb and reduce NO_3^- at Mo-N_4 sites to desorbable NO_2^- and *NOOH to NH_3 on Fe-N-C. The catalyst achieved 94% F.E. and a high stability of 90% F.E. for 60 h[109].

Cobalt sulfides, i.e., Co_9S_8, CoS, CoS_2, show robust electrochemical activity for different applications owing to their accessible high surface area, high capacitive behavior, and intrinsic activity[110]. CoS is used in different areas, such as lithium-ion batteries[111], [112], [113], oxygen evolution reaction (OER)[89], [93], [114], hydrogen evolution reaction (HER)[115], [116], and ORR[93], [94], [95]. CoS_2(400)/N, S-GO catalyst was synthesized using cobalt, thiourea, and GO with solid-state thermolysis at 400 °C. High ORR performance of the catalyst where cobalt sulfide nanoparticles dispersed on N, S doped graphene oxide is correlated with strong coupling between CoS_2 and N, S-GO. XPS could detect the formation of CoS_2[93]. Ma et al. also associated high ORR activity with synergistic effects between Co_3O_4 and N, S dual-doped graphene foam[44] whereas Liu et al. related superior ORR activity to synergistic effects between $NiCo_2S_4$ nanoparticles and N/S-rGO[94]. To our knowledge, NO_3RR studies do not comprehensively examine the activity and selectivity of cobalt sulfide or metal sulfide catalysts. One study only included metal sulfides as a synthesis intermediate to produce their primary catalyst[99].

1.2 Investigation and Elucidation of Electrochemical Reactions

Understanding and enhancing the aforementioned electrochemical reactions is essential due to the design and operation of catalysts and systems that can make their respective applications economically viable worldwide[91]. The performance of a catalyst can be categorized by its tendency to follow (1) favorable adsorbable and desorbable intermediates by the catalyst along the associative or disassociative chemisorption processes[117], (2) the slowest reaction step is for the catalyst to drive the reaction: rate-determining step (RDS)[118], [119], (3) the potential loss to perform the reaction concerning reaction's thermodynamic onset potential: overpotential[117], [120], (4) how fast the catalyst carries out the electron transfer step: Tafel analysis[121], [122], (5) number of electrons transferred (n_e^-) for the reaction in which potential range[123], [124], [125] and (6) the selectivity of the catalyst towards the desired electrochemical reaction to facilitate the specific energy application[126], [127], [128]. On the other

hand, a catalyst must be durable and preserve its desired performance during the projected operation lifetime.

Some of the most studied and crucial electrochemical reactions can be listed as hydrogen evolution reaction (HER), carbon dioxide reduction reaction (CO_2RR), NRR, oxygen evolution reaction (OER), ORR and NO_3RR -to-NH_3. The scope of this thesis focuses on the investigation of ORR and NO_3RR using Co/NS-rGO catalysts.

1.2.1 Oxygen Reduction Reaction (ORR)

Hydrogen fuel cells are expected to acquire widespread commercial use soon due to their advantages such as high efficiency, no environmental pollution, and unlimited source of reactants. One of the main challenges for fuel cells in replacing thermal engines is the sluggish kinetics of oxygen reduction reaction (ORR) at the cathode. The cathode requires ~0.4 mg cm^{-2} of Pt loading for the commercial Pt/C catalyst to achieve the desired performance[129]. Considering scarcity and high cost, intensive research is being done to develop a non-noble metal catalyst that can replace Pt/C catalysts[72]. Performance-limiting cathode reaction ORR (eq.1) and hydrogen oxidation reaction (HOR) (eq. 2) equations at the anode are shown below:

$$\frac{1}{2}O_2 + 2(H^+ + e^-) \rightarrow H_2O \ (E_0 = 1.23\ V\ vs.RHE) \quad (eq.1.1)$$

$$H_2 \rightarrow 2(H^+ + e^-) \ (E_0 = 0\ V\ vs.RHE) \quad (eq.1.2)$$

According to Nørskov et al., The mechanism of ORR can be categorized into two different mechanisms: dissociative and associative mechanisms. The steps of the associative mechanism can be listed as follows[117]:

$$\frac{1}{2}O_2 + * \rightarrow O \quad (eq\ 1.3.1)$$

$$O^* + H^+ + e^- \rightarrow HO^* \quad (eq\ 1.3.2)$$

$$HO^* + H^+ + e^- \rightarrow H_2O + * \quad (eq\ 1.3.3)$$

* stands for sites on the surface.

Further decompositions of H_2O for associative mechanism can be equated as:

$$H_2O + * \rightarrow HO^* + \frac{1}{2}H_2 \quad (eq\ 1.3.4)$$

$$H_2O + * \rightarrow O^* + H_2 \quad (eq.\ 1.3.5)$$

The disassociative mechanism does not consider the O_2 disassociation and leads to either peroxy intermediates or the end-product of water. The steps of the disassociative mechanism can be listed as follows[117]:

$$O_2 + * \rightarrow O_2^* \quad (eq\ 1.4.1)$$

$$O_2^* + (H^+ + e^-) \rightarrow HO_2^* \quad (eq\ 1.4.2)$$

$$HO_2^* + (H^+ + e^-) \rightarrow H_2O + O^* \quad (eq\ 1.4.3)$$

$$O^* + (H^+ + e^-) \rightarrow HO^* \quad (eq\ 1.4.4)$$

$$HO^* + (H^+ + e^-) \rightarrow H_2O + * \quad (eq\ 1.4.5)$$

ORR can acquire separate n_e^- along different reaction pathways in alkaline environments, the $4e^-$ to HO^-, $2e^-$ HO_2^- to, and $2e^-$ + $2e^-$ HO^- pathways[11]. The former produces HO^-, which is more desirable for fuel cell applications, while the latter produces HO_2^-, which can lead to fuel cell poisoning and activity loss but can be utilized to produce industrial chemical hydrogen peroxide[125]. Different ORR electron transfer pathways in alkaline media are shown in the figure below[130]:

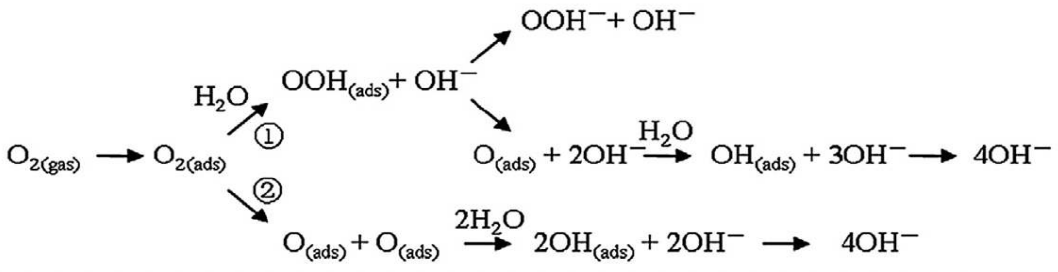

Figure 1-1: ORR Electron Transfer Pathways in Alkaline Media[130]

The origin of the ORR activity of materials can be investigated by examining their electronic properties[131]. Gerischer proposed that determining parameters for electron-

transfer kinetics of semiconductors is the position of electrons or holes and their density of states (DOS) near the Fermi level[124]. N-doping not only enhances the ORR activity of the catalyst but allows zero-band gap semiconductor graphene to change its band and electronic structure and obtain n-type semiconductor properties[26], [63], [131], [132]. Also, it is found that N-doping not only induces electronic states around the Fermi level in its bandgap but is the primary reason for the increase in DOS on the carbon surface near the Fermi level. Since the electrocatalytic activity of the material is claimed to depend on DOS near the Fermi level, it increases with an increase in DOS[131]. For the ORR mechanism, it is postulated that O_2 reduction occurs by filling empty or half-filled anti-bonding orbitals of O_2 by donating electrons from the catalyst surface. Electron transfer ends up with O-O bond cleavage and H_2O_2 and/or H_2O forms. The presence of electronic states around the Fermi level introduced by doping enables the filling of anti-bonding orbitals of O_2 that are needed for reduction and lower the energy barrier for ORR[131].

1.2.2 Nitrate Reduction Reaction (NO_3RR)

Electrochemical nitrate reduction (NO_3RR) to NH_3 is a complex 8 e^- and 9 H^+ transfer process with many intermediates with different adsorption and desorption characteristics[7], [133]. The reaction begins with the adsorption of NO_3^- and, consequently, 2 e^- reduction to the NO_2^-, commonly recognized as the rate-determining step (RDS)[20]. Afterward, suppose NO_2^- is not desorbed to the solution[99], [134], [135], [136]; in that case, it is reduced to NO and further to its possible products of NO_2, NO, N_2O, N_2, NH_2OH, N_2H_4, and NH_3 (Fig 1.2), which is classified as a selectivity-determining step[137], [138]. The binding strength of the reaction intermediates differ from each other, i.e., the binding affinity of NO_3^- to transition metal surfaces is limited owing to its favorable adsorption to H_2O and its symmetrical (D_{3h}) resonant structure[139]. Furthermore, it is possible to modulate the adsorption of the intermediates by changing the electronic structure[140], [141], whereas tailoring the binding affinity of NO_3^- can become counterproductive for the adsorption of *H, and high negative potentials are needed to provide multiple *H atoms in multiple steps of NO_3RR[119], [142]. An insufficient amount of *H species for the deoxygenation step will cause a high NO_2^- concentration in the electrolyte. Also, it is essential to note that

H_2O provides the H^+ ions necessary for NO_3RR, and H^+ concentration is very low ($\leq 10^{-7}$ M) in alkaline media[143], [144]. At the same time, the concentration of NO_3^- ions is considered low due to the negative bias on the electrode[145]. The NO_3RR and HER are competing reactions and NO_3RR has many possible by-products[146], so the material should disassociate water to get protons and activate the NO_3^-. Different reactions of the nitrate reduction with their n_e^- and thermodynamic potentials are shown below equations, along with different side-products of the reactions (Figure 1.2) [137]:

$$NO_3^- + 6H_2O + 8e^- \rightarrow NH_3 + 9OH^- \; E^0 = -0.12 \; vs. RHE \quad (eq\ 1.5.1)$$

$$NO_3^- + H_2O + 2e^- \rightarrow NO_2^- + 2OH^- \; E^0 = 0.01 \; vs. RHE \quad (eq\ 1.5.2)$$

$$NO_2^- + 5H_2O + 6e^- \rightarrow NH_3 + 2OH^- \; E^0 = -0.165 \; vs. RHE \quad (eq\ 1.5.3)$$

$$NO_3^- + 3H_2O + 5e^- \rightarrow \frac{1}{2}N_2 + 6OH^- \; E^0 = 0.26 \; vs. RHE \quad (eq\ 1.5.4)$$

$$NO_2^- + 2H_2O + 3e^- \rightarrow \frac{1}{2}N_2 + 6OH^- \; E^0 = 0.406 \; vs. RHE \quad (eq\ 1.5.5)$$

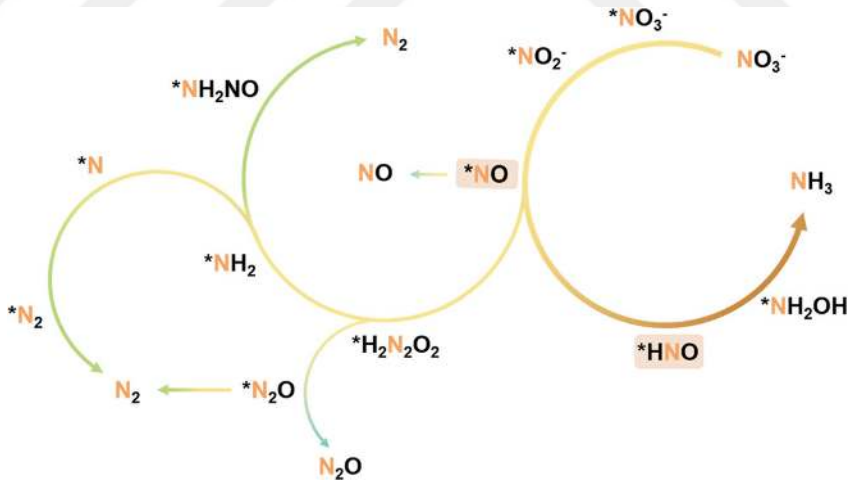

Figure 1-2: Electrochemical Nitrate Reduction (NO_3RR) Pathways

As seen in the above figure and equations, electrochemical NO_3RR is a reaction that becomes a reaction that depends heavily on selectivity if one considers more thermodynamically feasible HER at 0 V vs. RHE, too. Therefore, for NH_3 electrosynthesis, a catalyst should not be a suitable HER catalyst like MoS_2[146] while not favoring N_2 production like Pd[147]. The catalyst must be selective towards the NH_3 production pathway with intrinsic properties that favor the pathway rather than being only a catalyst that exhibits high current loads.

1.3 *Aim of the Study*

This study aims first to characterize and understand the structural, morphological, and elemental properties of Co/NS-rGO catalysts with different metal loadings and heat treatments. After identifying the material, its activity and selectivity towards ORR and NO_3RR are thoroughly investigated. Rather than only unraveling the superior activity of Co/NS-rGO catalysts towards electrochemical reactions, its electron transfer mechanism and adsorption tendencies are also examined. Electrochemical methods such as EIS, RRDE, DRT model, and Tafel analysis are studied to understand the reaction pathways. For NO_3RR, activity and the selectivity of the catalyst are investigated using both NO_3 and NO_2 species in a wide potential range. This potential range is adapted to identify the catalysts' mass-transfer limited and kinetic behaviors in different potentials. After these identifications, through XAS, EIS, DRT, and Tafel analysis, the NO_3RR mechanism of the catalyst is elucidated. For ORR, after studying the activity of the catalyst using cyclic voltammetry (CV) and RDE techniques, we analyzed the electron transfer mechanism of the catalyst using RRDE techniques. Mechanistic studies were followed by experiments to understand the origin of the ORR activity of the catalysts through electronic property analyses. The density of states, charge carrier concentration, and flatband potential of the catalyst are studied to understand the number of electronic states available for ORR around the fermi level, to understand the density of the carriers to drive the reaction and its semiconductor properties' allegiance with ORR performance respectively.

Chapter 2:
Synthesis and Experimental / Characterization Techniques

2.1 Synthesis of the GO, NS-rGO, NS-rGO 900, Co/NS-rGO, 2Co/NS-rGO, and Co/NS-rGO 900 materials

2.1.1 Synthesis of Graphene Oxide (GO)

GO is synthesized using the improved Hummer's method[37]. The synthesis starts with the preparation of the acid mixture by stirring 180 mL of H_2SO_4 (Sigma-Aldrich, cat #339741, ACS reagent, ≥99.999%) and 20 mL of H_3PO_4 (Sigma-Aldrich, cat #695017, ACS reagent, ≥99.999%) for 15 min. Then, the prepared acid mixture is added to 1.5 g of graphite powder (Sigma-Aldrich, cat #282863, powder, <20 μm, synthetic) and stirred overnight. In the next step, 9 g of $KMnO_4$ (Sigma-Aldrich, cat #223468, ACS reagent, ≥99.0%) is added to the prepared solution very slowly where solution temperature is kept between 0-5 °C using an ice bath to prevent the production of any strong exotherms. Afterward, the mixture is stirred for 12 h in an oil bath while the temperature is kept at 50 °C. Later, the solution temperature is lowered to 25 °C, and 200 mL of ultrapure water is added to the mixture conditions very slowly to prevent any sudden temperature increase. Finally, in stirring conditions, 1.5 mL of 30% H_2O_2 (Supelco, cat #107298) is added to the mixture very slowly, and the solution color changes to yellowish brown. Then, the obtained solution is centrifuged (Orto Elresa Digicen 21) at 2500 rpm for 30 min to decant the supernatant. The remaining product is washed with ultrapure water, 1.0 M of HCl (Supelco, cat #HX0607, 34-37% Omni *Trace*), and ethanol three times successively; after each wash, the solution is centrifuged, and the supernatant is decanted away. Finally, the product is freeze-dried to maintain the exfoliated nature of GO. GO is preserved in DI water to protect its unique structure[37].

2.1.2 Synthesis of NS-rGO and NS-rGO catalysts

Synthesis of NS-rGO starts with preparing a dispersion of 0.3 g of GO and 1.5 g of thiourea (Sigma-Aldrich, cat #527084, ReagentPlus®, ≥99.0%) in 150 mL of ultrapure water. The mixture is then autoclaved at 190 °C for 18 h. Also, to synthesize NS-rGO

900, NS-rGO is pyrolyzed at 900 °C for 1 h in an N2 atmosphere with a ramp rate of 5 °C/min.

2.1.3 Synthesis of Co/NS-rGO, 2Co/NS-rGO and Co/NS-rGO 900 catalysts

To synthesize DMF-protected Co precursor solution, N, N-dimethylformamide (DMF)(Sigma-Aldrich, cat #319937, ACS reagent, ≥99.8%) is heated up to 140 °C, and 1 mL of 0.1 M $CoCl_2$ (Sigma-Aldrich, cat #255599, ACS reagent, ≥98.0%) solution is added to DMF at 140 °C in vigorous stirring conditions. Then, the mixture is refluxed for 12 h in an oil bath while maintaining its temperature at 140 °C. After 12 h, the refluxed solution is halved using a rotary evaporator to remove excess DMF. Co/NS-rGO synthesis begins with dispersing 5 mg of NS-rGO in 5 mL of DMF to prepare 1 M NS-rGO/DMF solution. Afterward, a mixture of 5 mL of DMF-protected Co precursor solution and 1 M NS-rGO/DMF solution is sonicated for 30 minutes. Then, the mixture is dried at low pressure at 80 °C for 8 h using a rotary evaporator, and finally, Co/NS-rGO is obtained. 2Co/NS-rGO is prepared using the same protocol except for adding a two-fold volume of DMF-protected Co precursor solution used to synthesize Co/NS-rGO. Furthermore, for the synthesis of Co/NS-rGO 900, Co/NS-rGO is pyrolyzed at 900 °C for 1 h in an N2 atmosphere with a ramp rate of 5 °C/min.

2.2 Structural Characterizations

2.2.1 X-ray diffraction (XRD)

XRD is a structural characterization technique that adopts the principle of inspecting a material's elastic scattering capabilities excited by X-ray photons. The analysis of XRD data is often qualified and interpreted through the XRD patterns that the material exhibits through the constructive interference of X-ray photons excited by the material characteristics[148]. Crystallographic properties of the materials, such as lattice spacing and crystallite size, can be unraveled using XRD analyses. Lattice spacing provides information about the orientation of crystalline planes concerning each other, i.e., a specific plane being compact and reduced through lower lattice spacing or the exfoliated nature of the plane through higher lattice spacing. Crystallite size enables us to analyze the size of a crystallite or a particle assigned for that specific plane, such as metal oxides or carbon planes. Also, to identify the different planes of XRD patterns, one should

utilize the Powder Diffraction File (PDF) database and analyze the compatibility of one's XRD pattern with PDF results. Essential information of XRD can be listed as:

$$\text{Bragg's Law: } 2\ d\ sin\theta = n\lambda \quad (eq.2.2.1)$$

$$\text{Scherrer Equation: } D = n\lambda\beta cos\theta \quad (eq.2.2.2)$$

λ: X-ray wavelength; d: lattice spacing; θ= angle between the X-ray and the plane; β: Peak width half maximum.

2.2.2 Raman Spectroscopy

Raman spectroscopy is a method based on the concept of elastic scattering of monochromated photons that induces inelastic scattering on the material, also known as Raman scattering. Regarding this study, Raman spectroscopy can be used to determine the number of graphene planes using the following equation[149], [150]:

$$\omega_G(\text{G} - \text{peak wavelength number})(cm^{-1}) = 1581.6 + \frac{11}{1+n^{1.6}} \quad (eq.2.2.3)$$

$$\omega_G = (\text{G} - \text{peak wavelength number})(cm^{-1});\ n = number\ of\ graphene\ planes$$

2.2.3 X-ray Photoelectron Spectroscopy (XPS)

XPS is a surface-sensitive method that extracts essential information about the elemental composition, elemental bondings within the orbital, and the composition of the surface species on the material's surface. The XPS technique is based on Einstein's photoelectric effect concept, where the excitation of a photoelectron through interaction with incident photons and photoelectron attain kinetic energy associated with its binding energy[151], [152]. The equation for the photoelectric effect that XPS inherits from its foundations is:

$$E_k = hv - E_b - \varphi \quad (eq.2.2.4)$$

E_k: kinetic energy of the photoelectron; h: Planck's constant; E_b= Binding energy of the photoelectron ; φ= Work function loss between a sample and the device.

2.2.4 X-ray Absorption Spectroscopy (XAS)

XAS is a soft X-ray spectroscopy technique that provides information about the material's electronic and local geometric structure. In XAS, the photon energy is set so that the core electrons are excited to an unoccupied state where the significant

excitations of electrons introduce a region called an edge. Absorption edges of K, L, and M correspond to the principal quantum numbers of n=1, 2, and 3. XAS spectra contain two different regions emerging from excitations to the lowest occupied state: the main edge and rising edge, where the former is for transitions from the Fermi level and the latter is for transitions induced by photon energies lower than the lowest unoccupied states[153]. With higher photon energies, two different spectral of X-ray Absorption Near-Edge Structure (XANES) and Extended X-ray Absorption Fine Structure (EXAFS) can be studied, providing valuable insights about electronic structures through symmetry analyses for the former and atomic distance and coordination environment for the latter.

Synchrotron facilitates that have an XAS device

XAS results can be quantified using Beer's Law:

$$I_t = I_0 e^{-\mu(E)t} \quad (2.2.5)$$

I_t: X-ray intensity by transmission; I_0:Incident X-ray intensity; t:sample thickness; $\mu(E)$: absorption coefficient

2.3 *Electrochemical Tests*

2.3.1 Linear Sweep Voltammetry (LSV)

LSV is an electrochemical method where a specific potential range concerning a reference potential, i.e., vs. RHE vs. Ag/AgCl, is scanned with a selected scan rate using a potentiostat device, a two or three-electrode cell with respective acidic, basic, or neutral electrolytes with or without gas saturation. LSV results can be used to analyze reaction kinetics, current output, or electrode durability. LSV is a mass-transfer limited technique[154].

2.3.2 Cyclic Voltammetry (CV)

CV and LSV do not differ in how the experiment is performed. Unlike LSV, CV measurements are two-way measurements, meaning that a consecutive cathodic and anodic or anodic or cathodic scan direction is used. CV can be used to analyze the reversibility of redox reactions effectively by analyzing specific behaviors in given potentials after numerous cathodic and anodic cycles. CV measurements can also

introduce essential information about the charge storage properties of the material through electrochemical surface area (ECSA) and double-layer capacitance (C_{dl}) analyses. Furthermore, CV can be a vital electrochemical tool for analyzing the durability of materials and batteries through hours- or days-long cyclic experiments[154].

2.3.3 Rotating Disk Electrode (RDE)

RDE is a hydrodynamic electrochemical method that evaluates the performance of an electrode in a fixed potential range with a given scan rate as of LSV while eliminating mass-transfer limitations through the forced convection driven by rotation at a given rate. RDE plots give information about three different regions: (1) kinetic region, (2) mixed region, and (3) mass-transfer limited region. In the kinetic region, one can identify the efficiency of the reaction concerning side reactions through electron transfer number analysis[155]. By looking at the slope at the beginning of the mixed region, one can measure the material's Tafel slope, which shows how fast the reaction in the specified region is. Also, the mass-transfer limited region presents information about the mass-transfer limiting current of the catalyst and elucidates Levich analysis. Levich analysis equation is given below:

$$\text{Eq. 2: } i_l = 0.62nFAD^{\frac{2}{3}}v^{-\frac{1}{6}}c_0w^{\frac{1}{2}} \quad (eq.\,2.2.6)$$

i_l: limiting current; n number of electrons transferred; A: area of the electrode

F: Faradaic Constant; D: diffusion coefficient; v: kinematic viscosity of the electrolyte

c_0: solubility of O_2 in electrolyte; ω: rotation rate

2.3.4 Rotating Ring Disk Electrode (RRDE)

The RRDE technique utilizes the same method regarding the experiment, whereas the electrode design differs significantly from RDE's. In RDE, a glassy carbon working electrode is used, while in RRDE, a Pt or Gold ring is used to oxidize the material to the desired potential. By this method, one can measure the decomposition rate of specific

species, i.e., H_2O_2, or determine the number of electrons transferred in a wide potential range[122], [156].

For RRDE measurements, first, a collection efficiency must be obtained using a potassium ferricyanide solution. The equation for collection efficiency ($N_{empirical}$) is given below:

$$N_{empirical} = \left| \frac{i_{L,RING}}{i_{L,DISK}} \left(\frac{n_D}{n_R}\right) \right| \quad (eq.\ 2.2.7)$$

$N_{empirical}$: collection efficiency; $i_{L,RING}$: disk current; $i_{D,RING}$: ring current; n_D: number of electrons exchanged at the disk; n_R: number of electrons exchanged at the ring where $n_D = n_R$

The number of electrons transferred during ORR is calculated using the equation below:

$$n_e^- = \frac{4\left|i_{L,DISK}\right|/N_{empirical}}{i_{L,DISK} + i_{L,RING}/N} \quad (eq.\ 2.2.8)$$

The selectivity of the peroxide species is found as shown below:

$$H_2O_2\% = 2 \times \frac{i_{L,RING}/N_{empirical}}{i_{L,DISK} + i_{L,RING}/N} \times 100 \ \ (eq.\ 2.2.8)$$

2.3.5 Chronoamperometry (CA) and NH_3, NO_2, and H_2 quantification using the Indophenol Blue Method, Griess' Test, and Gas Chromatography

CA measurements are carried out by applying a desired constant potential for a given duration. NH_3, NO_2, and H_2 quantification are carried out using the equations below:

$$F.E._{NH_3} = \frac{8 \times F \times C_{NH_3} \times V}{\left(MW_{NH_3} \times Q\right)} \quad (eq.\ 2.2.9)$$

$$F.E._{NO_2^-} = \frac{2 \times F \times C_{NO_2^-} \times V}{\left(MW_{NO_2^-} \times Q\right)} \quad (eq.\ 2.2.10)$$

$$F.E._{H_2} = \left(n_{H_2\,flow} \times n_e \times F \times n \times V_{H_2\,flow}\right) \quad (eq.\ 2.2.11)$$

$$r_{NH_3,\,NO_2^-,\,H_2} = \frac{C_{NH_3,\,NO_2^-,\,H_2} \times V}{t \times m_{cat}} \quad (eq.\ 2.2.12)$$

F: Faradaic constant; C_{NH_3}: NH_3 concentration; V: volume of the catholyte; MW_{NH_3}: molecular weight of NH_3; Q: amount of charge accumulated; C_{NH_3}: NH_3 concentration; $C_{NO_2^-}$: NO_2 concentration; $MW_{NO_2^-}$: molecular weight of NO_2; $n_{H_2\,flow}$:

H_2 molar flow rate; n_e: number of electrons transferred; t: duration of CA; m_{cat}: the mass of catalyst loading

2.3.6 Electrochemical Analysis

2.3.6.1 Electrochemical Surface Area (ECSA)

ECSA analysis begins with a determination of double-layer capacitance (C_{dl}) by taking CV measurements in a specified non-Faradaic potential range with different scan rates and taking the slope of the graph between half of the difference between anodic and cathodic current at the middle potential of CV range[157]. Then, ECSA is calculated as follows:

$$\text{ECSA} = \frac{C_{dl}}{C_s} \quad (eq.\,2.2.13)$$

C_{dl}: Double layer capacitance; $C_S = Specific\ Capacitance = 0.022\ mF/cm^2$

2.3.6.2 Electrochemical Impedance Spectroscopy (EIS)

The EIS technique uses disturbances induced by applied potentials in electrochemical systems through sinusoidal waves and an analysis of the input's sinusoidal responses. EIS can be used to determine the material's charge transfer resistance (r_{ct}), perform capacitive analyses, or investigate the material's electronic properties[158]. Total layer capacitance and space-charge capacitance of the material can be found using EIS techniques as such:

$$C_{tot} = -\frac{1}{2\pi f Z_{img}} \quad (eq.\,2.2.14)$$

C_{tot}: Total double-layer capacitance; f: frequency; Z_{img}: the imaginary part of the Nyquist plot; C_{SC}: space-charge capacitance

$$Eq.\,5\text{: } C_{tot,ECSA} = \frac{C_{tot}}{ECSA} \quad (eq.\,2.2.15)$$

$$Eq.\,6\text{: } \frac{1}{C_{tot,ECSA}} = \frac{1}{C_H} + \frac{1}{C_{SC}} \quad (eq.\,2.2.16)$$

$$C_H = Helmholtz\ capcitance = 0.02\ mF/cm^2$$

Furthermore, the density of states of a material ($D(E_F)$), charge carrier density (N_D), and flatband potential (V_{fb}) can be measured using EIS techniques by taking an impedance measurement around the onset potential of the catalyst towards the reaction of interest, then carrying out the following algebra[159]:

$$D(E_f) = \frac{{C_{SC}}^2}{\varepsilon\varepsilon_0 {e_0}^2}$$

$C_{SC} = Space - charge\ capacitance$; $\varepsilon = Dielectric\ constant = 3.3$

$\varepsilon_0 = Vacuum\ permittivity = 8.854 \times 10^{-1} \frac{F}{m}$

$e_0 = Electronic\ charge = 1.602 \times 10^{-19}$

$$Eq.8: D(E_f) = \frac{{C_{SC}}^2}{\varepsilon\varepsilon_0 {e_0}^2}$$

$$\text{Eq. } 9: N_D = \frac{2}{\varepsilon\varepsilon_0 e_0 ECSA^2 MS_{slope}}$$

$$\text{Eq. } 10: \frac{1}{C^2} = \frac{2}{\varepsilon\varepsilon_0 e_0 ECSA^2 N_D} (V - (V_{fb} + \frac{kT}{e}))$$

MS_{slope}: Mott-Schottky slope; k: Boltzmann constant; T: absolute temperature

Chapter 3:

Elucidation of Activity and Selectivity of Co/NS-rGO Catalysts Towards ORR Using In-Depth Kinetic and Electronic Property Analysis

3.1 Introduction

3.1.1 Importance of ORR for Sustainable Energy Future

To reduce global fossil fuel dependence, robust and cost-effective renewable energy technologies should be widely used to meet increasing energy demand[2]. Proton exchange membrane fuel cells (PEMFCs) hold great importance because they compensate for the bottlenecks of recently emerging lithium-ion batteries and further enable full electrification of vehicle transportation[14], [160], [161], [162], [163]. It is widely known that PEMFC activity is primarily limited by sluggish oxygen reduction reaction (ORR) kinetics at the cathode despite the high loading of active expensive platinum group metal (PGM) electrocatalysts, i.e., Pt, at both cathode and anode[164], [165]. Scarcity and the high price of Pt are some of the most prominent issues facing the large-scale commercialization of PEMFCs[72], [79], [129], [166]. It is proposed that for economically advantageous PGM-free materials to replace Pt, they must have optimum durability, many available active sites[167], turnover frequency (intrinsic activity)[146], mass transport, and charge/electron transfer properties[168], [169]. Also, PGM-free catalysts need to avoid degradation during hours of continuous PEMFC operation[170]. Over the years, intensive effort has been put into synthesizing either low-PGM catalysts with alloying[24], [168], [171], [172], [173], [174], [175], atomically dispersed PGM catalysts[176], core-shell structures[23], [24], [177], [178], PGM-free catalysts, N-doped carbon materials[47], [63], atomically dispersed metal nitrogen carbon catalysts[62], [179], [180], [181], [182], [183], [184], [185], [186], [187] and heteroatom-doped metal catalysts[51], [188], [189].

PGM catalysts have activity setbacks such as demetallation, degradation, aggregation[190], sulfur deactivation[191], and the inability of superoxide protonation in fuel cell conditions[192]. High surface area metal nitrogen carbon (M-N-C) catalysts are proposed to overcome these setbacks as alternative ORR catalysts[186]. Previously, Fe-

N-C catalysts were proposed as an alternative to PGM catalysts due to their high stability and activity[179], [182], [187], [193]. Wu et al. synthesized PANI-Fe-C catalyst using ketjen black and polyaniline (PANI) as the carbon and nitrogen sources mixed with iron salts and then subjected to heat treatment[179]. Catalyst has shown 0.3 V of overpotential, 99% $4e^-$ selectivity, and durability of 700 hours at 0.4 V, a relatively low potential for PEMFC operations. However, like other Fe-N-C catalysts[194], PANI-Fe-C catalyst suffered from significant performance loss at 0.6 V, which can be due to the amorphous nature of the material[179] and demetallation during fuel cell operation in an acidic environment[194], [195], [196]. It is claimed that using Co instead of Fe for the catalyst would make ORR less dominated by Fenton reactions detrimental to PEMFC activity.

3.1.2 Aims of Study

Herein, we develop Co/NS-rGO and 2Co/NS-rGO catalysts with 1:2 Co content, CoS presence, and Co SA(single-atom) distribution along the graphene plane. The effect of Co amount in both catalysts is investigated in terms of overpotential R_{ct} (charge-transfer resistance), ECSA, current density, and capacitance values. Furthermore, the electronic properties of the catalysts are examined using EIS techniques, including the semiconductor properties of the material, flatband potential, density of states (DOS), and carrier concentration. The synergy between CoS, Co-N_x moieties, and Co SAs is studied to understand the origin of the superior ORR activity. Also, the benefits of using S as a co-dopant are studied to unravel its intervention in forming ORR-active structures, electronic properties, and superior kinetic assets.

3.2 Experimental Methods

3.2.1 Structural Characterizations

200 kV aberration-corrected FE-TEM/STEM Hitachi HF5000 equipment is used to perform transmission electron microscopy (TEM) images, where a 20 kV Zeiss Ultra Plus microscope is utilized to obtain the scanning electron microscopy (SEM) images. Bruker D2 Phaser X-ray Diffractometer records X-ray diffraction (XRD) results for the powder samples with Cu Kα radiation having potential and current of 10 kV and 30 mA, respectively. The Renishaw INVIA instrument was used for Raman spectroscopy, performed at 532 nm of laser excitation wavelength. X-ray photoelectron spectroscopy

(XPS) was performed using a Thermo K-alpha with monochromatized Al Kα (1486.7 eV) radiation.

3.2.2 Electrochemical Screenings

The electrochemical characterizations of the rotating disk electrode (RDE) and rotating ring disk electrode (RRDE) were carried out using a Pine Research WaveDriver 40 DC Biopotentiostat in an N_2 or O_2-purged 0.1 M KOH electrolyte with standard three-electrode cell configuration. H_2O^- selectivity measurements were performed using a rotating ring disk electrode (RRDE) with Pt ring, and a collection efficiency value of 27% is determined in potassium ferrocyanide ($K_3[Fe(CN)_6]$) (Sigma-Aldrich, cat #244023, ACS reagent, ≥99.0%) solution considering red-ox reaction between $Fe(CN)_6^{3-}$ and $Fe(CN)_6^{4-}$ species. The three-electrode cell configuration comprised a graphite rod or platinum coil used as a counter electrode, an Ag/AgCl reference electrode calibrated by a standard hydrogen electrode, and a coated glassy carbon electrode as the working electrode. The working electrodes were prepared by drop-casting the as-prepared ink onto the glassy carbon electrodes. The catalyst inks consisted of 5 mg of the regarding catalyst, 120 µl of pure ethanol (Sigma-Aldrich, cat #32221-M, absolute, ≥99.8%), and 5 µl Nafion™ perfluorinated resin solution (Sigma-Aldrich, cat #510211). The mass loading of catalysts on the glassy carbon electrode was set to 0.204 mg cm^{-2}. The iR compensation for all electrochemical measurements was performed at 85% and 100 kHz using either a Biologic SP-200 or a VSP-300 Potentiostat. All the other electrochemical impedance spectroscopy (EIS) and voltammetric measurements are carried out using a Biologic VSP-300 Potentiostat. The double-layer capacitance (C_{dl}) values were calculated by taking half of the slope for the anodic and cathodic current density differences ((j_a-j_c/2)) versus the potential scan rate (mV/s) plot. Then, C_{dl} is divided by specific capacity (C_s) of 0.022 mF/cm^2 to find the electrochemical surface area (ECSA). Tafel analysis was carried out by plotting potential versus log (j) in the kinetic region.

3.3 Characterizations Of The Catalysts Using Imaging, Spectroscopy And Crystallographic Techniques

As described in the experimental methods part, first, NS-rGO is synthesized by autoclaving 1:5 %w/w thiourea, GO aqueous solution for 18 h at 190 °C. Then, cobalt

loading is carried out by intercalating Co/DMF precursor to NS-rGO/DMF dispersion at 80 °C for 12 h. We pursued a low-pressure, low-temperature, and long-duration approach to preserve graphene's defect-rich, porous, and layered structure (Fig. 3-1)[197]. Thiourea, as a doping reagent, is claimed to facilitate the interaction between GO and N/S due to its ability to provide the heteroatoms to the graphene plane simultaneously[76], [198]. For Co/NS-rGO, an excess amount of cobalt incorporation into the NS-rGO matrix is avoided; hence, the formation of neither large chunks of nanoparticles nor clusters is observed, which can be seen in high-resolution scanning transmission electron microscopy (HR-STEM) results (Fig. 3-3 a-d). Determination of the optimum Co-to-NS-rGO ratio has enabled the anchoring of many cobalt SAs and actualized even distribution of Co, N, and S atoms throughout the NS-rGO matrix, which is shown in EDX mapping (Fig. 3-2). It is speculated that during the incorporation of Co, the presence of S prevented the formation of CoO_x by facilitating Co-S interactions to form CoS.

The HR-STEM image (Fig. 3-3a) shows that we could preserve the layered, exfoliated, and porous nature of NS-rGO and obtain a wrinkle-like structure intrinsic to doped rGO materials[199]. Co SAs, which are homogeneously distributed throughout the graphene material, are claimed to boost ORR activity (Fig. 3-3 b, c, d). Also, HR-STEM images for 2Co/NS-rGO indicate the abundance of Co_xO_y species in the material (Fig. 3-3 e, f, g, h).

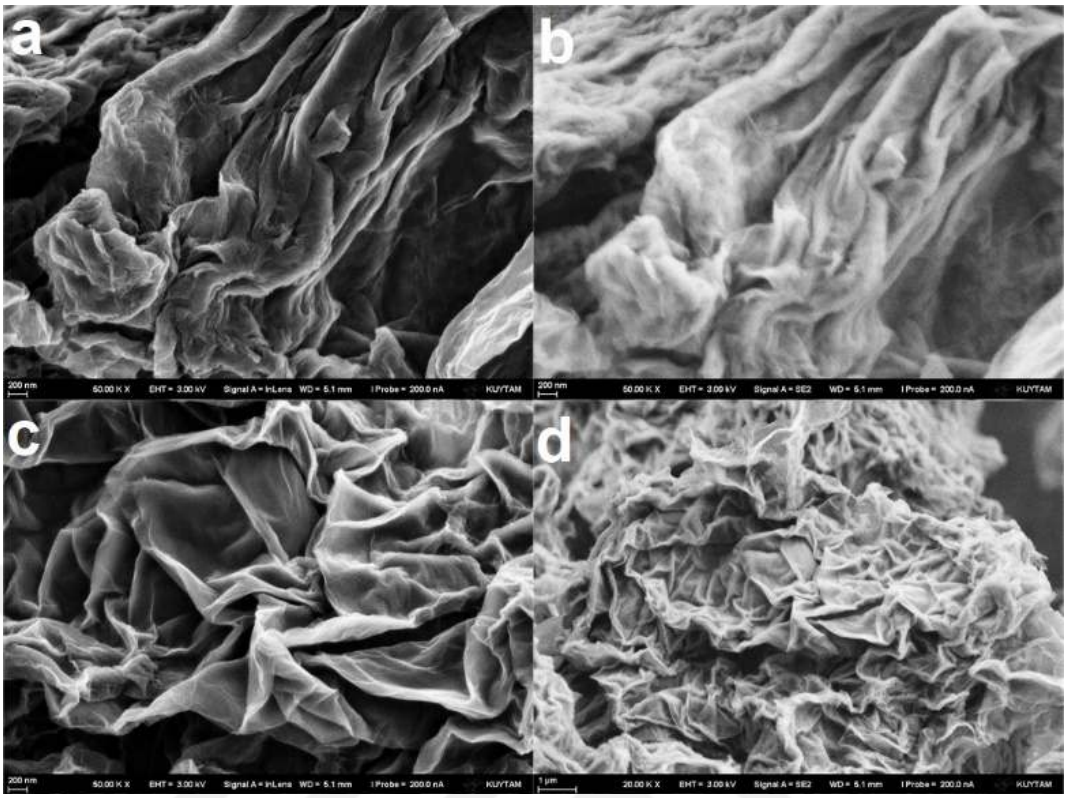

Figure 3-1 Scanning Electron Microscopy (SEM) images for NS-rGO

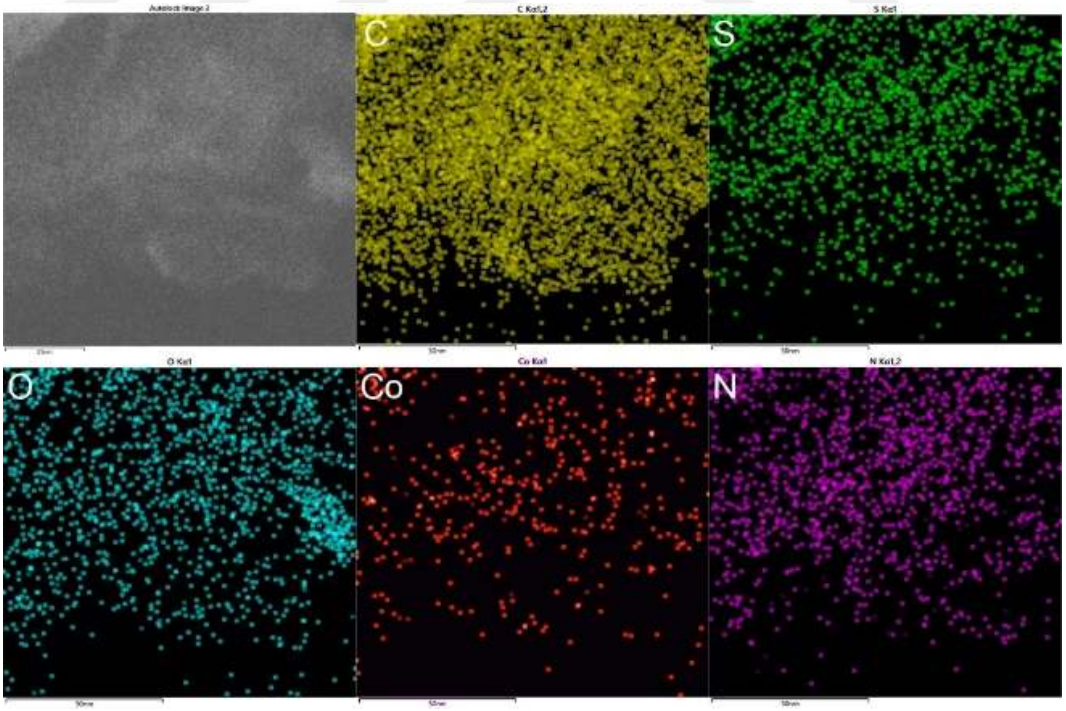

Figure 3-2 HR-STEM EDX Mapping for Co/NS-rGO

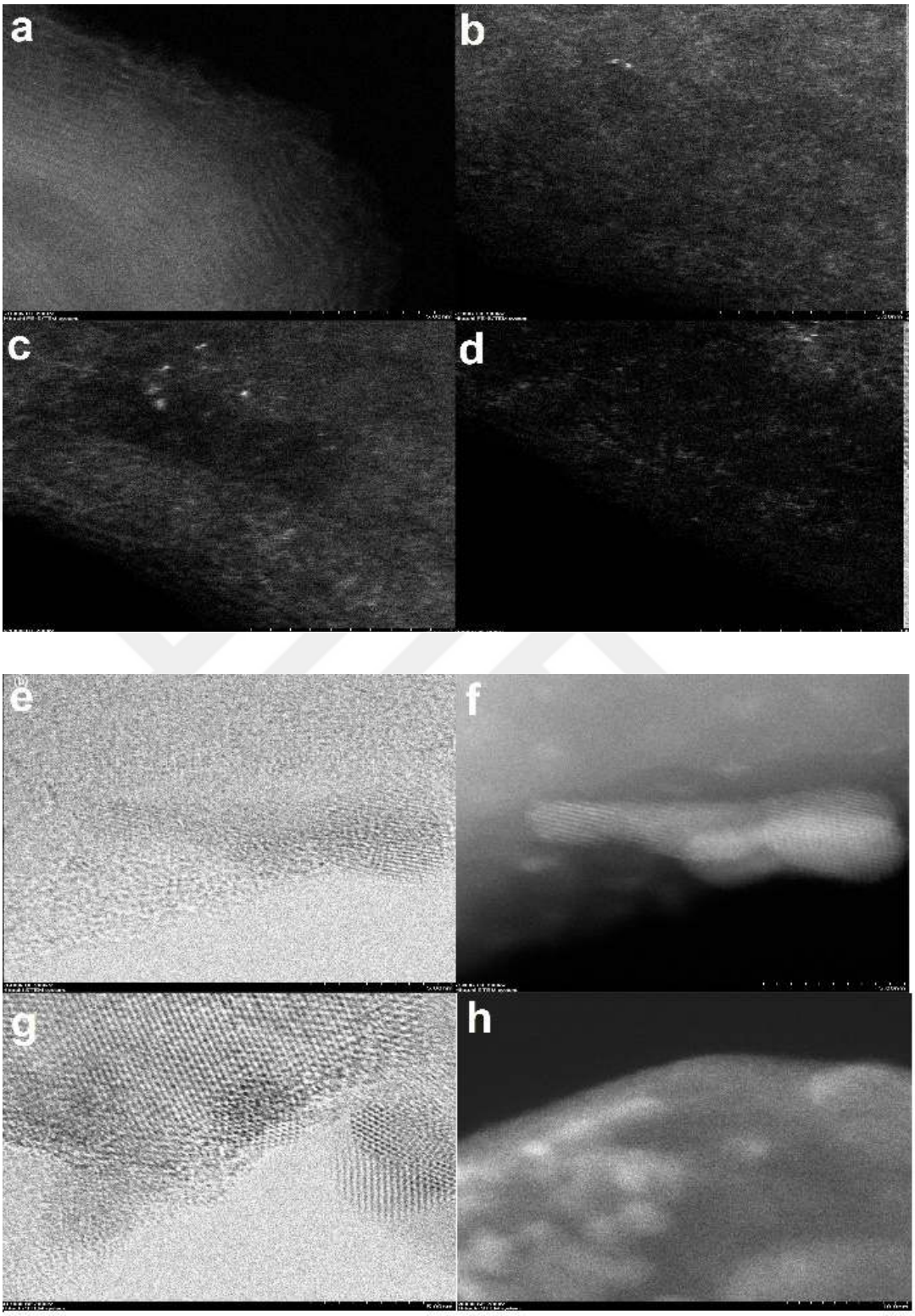

Figure 3-3. HR-STEM images. a, b, c, d) Co/NS-rGO. e, f, g, h) 2Co/NS-rGO

EDX analysis (Fig. 3-2) demonstrates the chemical bonding nature of Co SAs distributed over the region with a similar S, N, and O species distribution throughout the graphene plane. Interestingly, despite the relatively high amount of oxygen in the material, there is

no visible formation of cobalt oxide nanoparticles for Co/NS-rGO. Still, cobalt oxide formation is commonly observed in oxygen-containing cobalt catalysts[44], [59] and is present for 2Co/NS-rGO. X-ray photoelectron spectroscopy (XPS) S 2p (Fig. 3-4d) spectra show that S favors sulfate formation for Co/NS-rGO and suppresses cobalt oxide formation, possibly due to lower formation energy of SO_4^{2-} while the 2Co/NS-rGO exhibits low SO_4^{2-} formation, indicating the possibility of cobalt oxide presence. The presence of abundant, homogenously distributed single atoms in Co/NS-rGO (Fig. 3-2) and the simultaneous occurrence of CoS particles (Fig. 3-4d) is speculated to be the cause of the catalyst's superior ORR performance. CHNS results show that S and N content is 17% (Fig. 3-5b) and 9% in the catalyst Co content is found as 1.8% for Co/NS-rGO and 5.11% for 2Co/NS-rGO using ICP-MS (Fig. 3-5c)

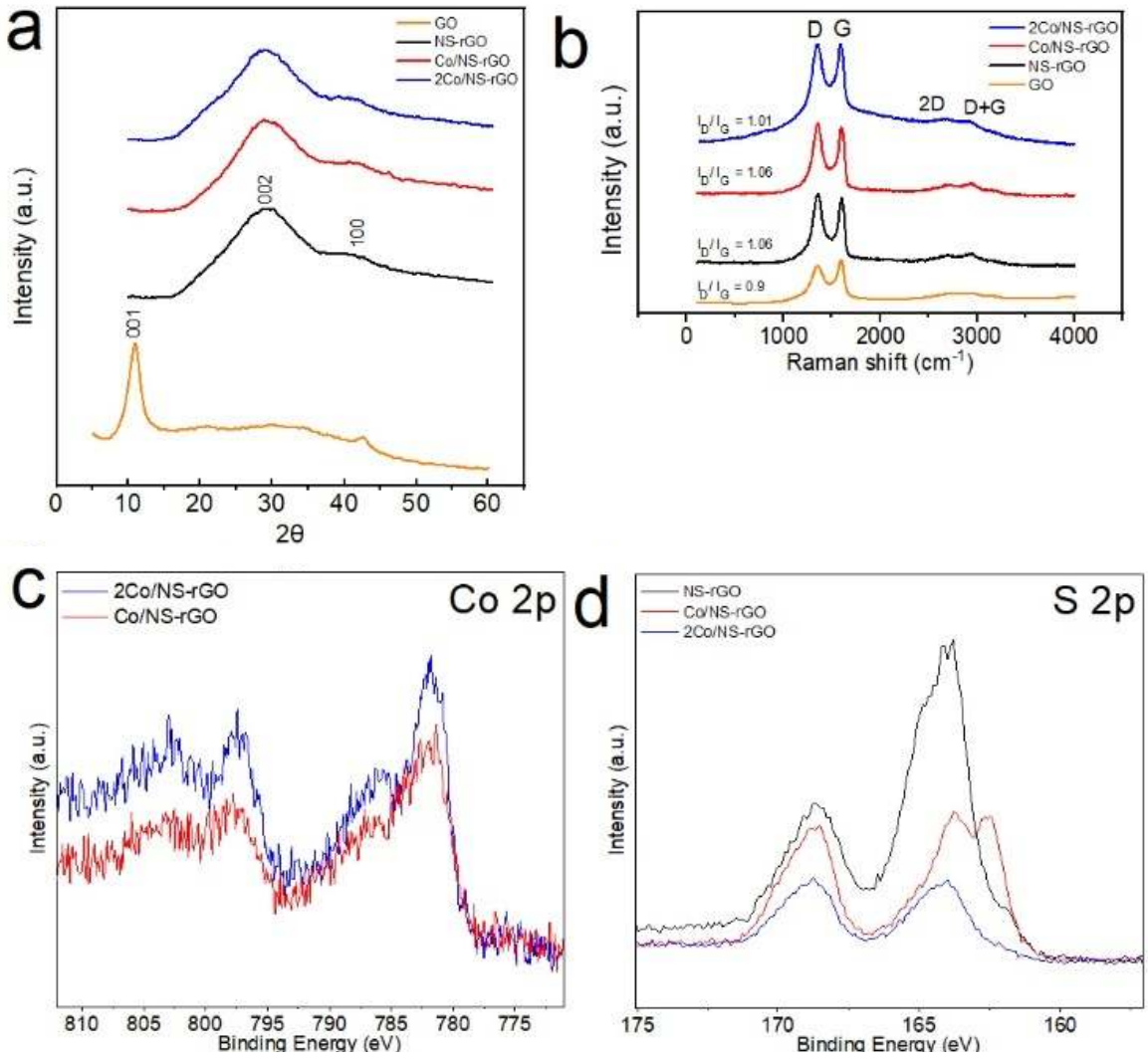

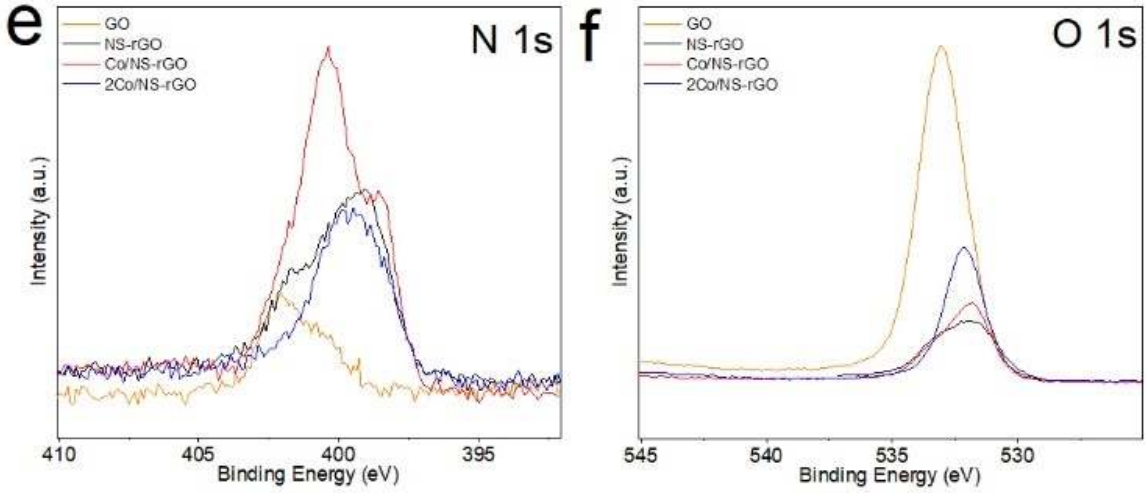

Figure 3-4 Structural Characterizations. a) XRD. b) Raman Spectra. c) XPS Co 2p. d) XPS S 2p. e) XPS N 1s. f) XPS O 1s.

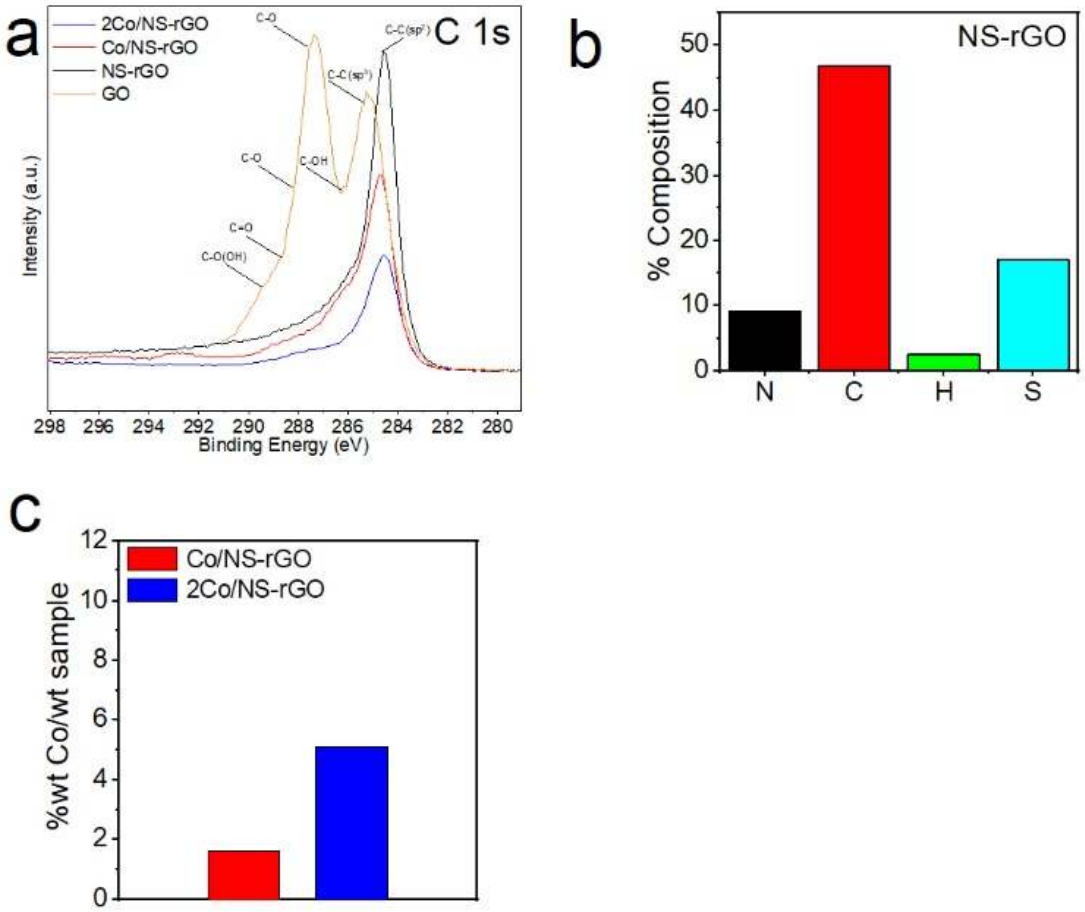

Figure 3-5 Structural Characterizations. a) XPS C 1s. b) CHNS for NS-rGO. c) ICP-MS for Co/NS-rGO and 2Co/NS-rGO

X-ray diffraction (XRD) patterns (Fig. 3-4a) show the emergence of a sharp peak at 2θ = 10.9° for GO (001), suggesting successful oxidation of graphite (characteristic peak at 2θ = 26°). GO XRD reflections indicate that a significant fraction of graphite to GO

conversion has succeeded; however, a small peak at 2θ = 43° attributed to a graphite impurity is still visible[200], [201]. The peak assigned to the (001) plane in GO appears in NS-rGO and Co/NS-rGO (Fig. 3-4a), manifesting a substantial reduction for both materials[202]. Crystalline planes of (002) and (100) present in graphene-like carbon materials are aligned at 2θ = 28.8° and 41.5° values, respectively[76], [92], [203]. The reflections from (002) and (100) planes are deviated to 2θ = 26° and 43°. This shift is possibly due to the presence of oxygen in the sample and convolution due to the presence of CoS species[76]. Weak intensity and broad peaks at crystalline planes of carbon (002) and (100) in both Co/NS-rGO and NS-rGO show the formation of loosely stacked graphene layers that are different from graphite, which has narrow and sharp peaks[92], [204]. Nearly the same XRD pattern of Co/NS-rGO and NS-rGO and the same d-spacing values (d_{002}) of the carbon planes suggests that the Co incorporation did not cause a change in crystalline properties of NS-rGO in large size and further actualized formation of CoS moieties.

Raman spectra (Fig. 3-4b) show carbon's disorder-induced D and G bands at 1354 cm^{-1} and 1598 cm^{-1}, respectively[205]. Higher intensity ratio for D and G bands (I_D/I_G) of Co/NS-rGO and NS-rGO (1.06) compared to GO (0.9) proves the reduction of GO, incorporation of N and S to graphene lattice, and increase in defect density induced by the two atoms for Co/NS-rGO and NS-rGO[95], [203] while the 2Co/NS-rGO lacks defect-rich properties possibly linked to its inferior activity. I_D/I_G ratio for NS-rGO (1.06) does not change after cobalt incorporation, which emphasizes the inability of Co to induce carbon-related defects. It is proposed that the G band in Raman spectra arises from the presence of sp^2 rings in the material, and G-peak intensity increases with increased doping levels; we verify the presence of sp^2 rings in each sample by existing G band and successful doping with the increased G-peak intensity[206]. For the analysis, we used intensity ratios (I_D/I_G) rather than area (A_D/A_G) ratios due to the high disorder of the materials in this study[149]. Therefore, we did not carry out any peak deconvolutions deriving from the area of each band and stuck to intensity values in Raman analysis. Also, the number of graphene layers is calculated using G peak position values[207], and it is found to be approximately 4 in all three of the samples, which verified the preserved nature of layered graphene[207]. The 2D peak claimed to be affected by doping levels, and the number of graphene layers is present at 2678 (cm^{-1}) for all three samples[206],

[208]. Considering peak intensity at D + G combination mode (2950 cm^{-1}), induced by disorder, CoNS-rGO and NS-rGO have the same and higher disorder than GO, which is the observed pattern throughout the size of the $\sqrt{\frac{I_D}{I_G}}$ value is proportional to the average size of sp^2 ring clusters (L_A) ($L_a(nm) = \frac{560}{E_{laser}^4}(\frac{I_G}{I_D})$). L_A for NS-rGO does not change after cobalt incorporation, which lets us suggest that either pyridinic and graphitic N (Fig. 3-4e) substitutions to sp^2 hybridized graphene do not cause a significant size change due to similar size of C/N or low pyridinic, graphitic N / total N ratio or binding of nitrogen to deoxygenated sites to form pyrrolic N sp^3 hybridization is the reason for keeping the of sp^2 species with the same size [65], [205]. Finally, Raman spectroscopy results (Fig. 3-4b) show that C-$(S-S)_n$ bonds exist in NS-rGO, verified by the corresponding peak at 660 cm^{-1}[93]. In contrast, in Co/NS-rGO, the regarding peak does not exist, which allows us to suggest that C-S bonds in NS-rGO are broken and the remaining sulfur atoms are either bound to oxygen to form sulfate or bound to Co to form atomic scale CoS moieties.

Co 2p spectra (Fig. 3-4c) results also show a higher amount of Co is present on the material's surface, which agrees with ICP-MS measurements for bulk. Co 2p peaks characteristic of CoO are present for 2Co/NS-rGO, which supports our findings in HR-STEM.

In S 2p spectra (Fig. 3-4d), peaks of 168.7, 165.4, 163.8, and 162.4 eV are attributed to sulfate or thiosulfate (SO_4^{2-}, $S_2O_3^{2-}$) thiolic S (C-S-H), thiophenic-S (C-S-C), and S_n^{2-} (surface) respectively for both sulfur-containing samples[78], [94], [209], [210]. Shift to lower binding energies after incorporation of cobalt suggests the emergence of new functional groups and species[211]. Interestingly, in Co/NS-rGO, a single peak at 162.4 eV appears, and its emergence is derived from Co-S bonding[209]. It is claimed that S_n^{2-} (surface) species react first, and its corresponding CoS formation is achieved through the breaking up of the S-S bond, i.e., the peak intensity at 165 eV decreases and stabilization of S^- through electron transfer from Co to S_n^{2-} (surface) [212]. Also, peaks at 168.7 to 170.8 eV are assigned to sulfate species formed with exposure to air[213]. The most apparent difference between NS-rGO and Co/NS-rGO in S 2p spectra is the decrease in peak intensity of thiophenic (C-S-C) and thiolic S (C-S-C) with Co incorporation. This result agrees with Raman's results, where C-S bonding is only observed for NS-rGO.

These results support the hypothesis that C-S bonds are broken down with Co introduction to the catalyst, and the remaining sulfur is bound to Co to form CoS. Also, thiophenic-S (C-S-C), along with pyrrolic and pyridinic N species, is claimed to be another factor indicating that N and S doping on graphene is carried out effectively[94].

The peaks in XPS N 1s (Fig. 3-4e) at 398.4, 399, 400.4, and 401.8 eV are assigned to pyridinic N, amide N, pyrrolic N, and quaternary N[64], [214]. Along with CoS formation, the lower amount of Co incorporation enables the formation of pyridinic N, contributing to the superior ORR activity of Co/NS-rGO. Amide N formation for NS-rGO originated from heating thiourea and sulfuric acid at 190 °C. Also, the peak at 400.5 eV for pyrrolic N emerges for Co/NS-rGO. However, pyrrolic N is claimed not to be a ORR-active species since its presence does not affect the carrier concentration of graphene[63], [215]. Furthermore, the peak intensity for quaternary N is similar for both GO and NS-rGO, while Co/NS-rGO has a higher and 2Co/NS-rGO has a lower quaternary N content. It is claimed that the oxygen content in Co/NS-rGO is bound to N-species and suppresses CoO formation. At the same time, the low concentration of quaternary N for 2Co/NS-rGO could have promoted the CoO formation for the catalyst. Also, O 1s spectra (Fig. 3-4f) show that after the hydrothermal treatment, oxygen content in the material decreases while 2Co/NS-rGO obtains high oxygen content, which could be attributed to CoO formation.

XPS C 1s spectra (Fig. 3-5a) of GO show different high-intensity peaks starting from 286.2 eV to 290 eV that are attributed to C-OH, C-O, C=O, and C-O(OH) species, which shows the abundance of oxygen and oxygenated groups in GO. However, peaks of these oxygenated groups in NS-rGO, Co/NS-rGO, and 2Co/NS-rGO samples shift to lower binding energies but do not disappear after reduction, which shows the partial reduction and presence of pre-doped oxygenated species in all samples. We observe broader and more asymmetric C 1s peak of sp^2 C towards higher binding energies from NS-rGO to Co/NS-rGO due to increasing functional groups with Co introduction, such as CoS. The graphene-like structure is achieved, which is observed considering the presence of sp^2 hybridization in C-C bonds. We see a clear reduction in peak intensity of C-O / C-OH bonds after reduction to NS-rGO. We see that the peak for C=C sp^2 bonds obtain high intensity in NS-rGO, whereas after Co incorporation, regarding double bond peak intensity decreases and the relative intensity of single-bonded carbon increases, which is

most probably due to breaking of the double bond, functionalization of the surface species with their interaction with Co and alignment of pyridinic, pyrrolic and quaternary N. However, according to Raman Spectra analysis, we should also note that the size of sp^2 ring clusters stays the same after cobalt incorporation. This enables us to propose that the alignment of pyridinic and graphitic N does not cause a size change in graphene. Also, the significant increase in pyrrolic N content for Co/NS-rGO in N 1s spectra (Fig. 3-4e) causes us to suggest that the size of sp^2 hybridized ring clusters does not change since N species do not preferentially locate through sp^2 hybridization. Still, nitrogen may bind to edge sites of graphene where -COOH and -OH groups are left, and pyrrolic N is formed, which claims the fixed size of sp^2 ring clusters.

3.4 Electrochemical Activity and Selectivity Analysis: Unraveling Kinetic and Electronic Properties of the Catalyst

Cyclic voltammetry (CV) measurements in N_2 and O_2-purged electrolytes show the presence of two peaks at 0.4 V and 1.1 V, which can be assigned to CoS or quinone red-ox peaks[179], [216]. However, these peaks' irreversibility eliminates the possibility of quinone presence and allows us to assign them to CoS peaks. Bănică et al. showed the presence of CoS by showing the reduction in labile CoS peaks in time[216]. After several cycles, N_2-purged CV measurements (Fig. 3-7a) show a similar reduction trend in assigned CoS peaks of Co/NS-rGO. Also, N_2 CV (Fig. 3-6a) results indicate the superior capacitive/pseudocapacitive behavior after cobalt incorporation for Co/NS-rGO. In contrast, the excessive cobalt loading resulted in lower capacitance values for 2Co/NS-rGO, possibly due to agglomeration and cobalt oxide (CoO) formation. O_2 CV (Fig. 3-6b) measurements show the same CoS peaks for Co/NS-rGO, which aligns with N_2 CV. Also, the exact figure shows that 2Co/NS-rGO has $Co^{2+} \Leftrightarrow Co^{3+}$ peaks at 0.9 V at both anodic and cathodic scans[217], [218]. These oxidation-reduction peaks are present in CoO-derivative electrocatalysts[217], [218], [219], and we suggest that the relatively high cobalt loading leads to the formation of CoO for 2Co/NS-rGO. In contrast, a lower amount of Co in Co/NS-rGO leads to CoS formation for Co/NS-rGO.

O_2-purged rotating disk electrode (RDE) voltammetry results show a pseudo-limiting current plateau for all three samples. The materials studied in this work have porous characteristics. It is claimed that the supply of reactant (O_2) for porous materials is not the limiting parameter, but the product (HO_2^-) decomposition rate[220], [221]. It is observed that Co/NS-rGO has the highest current density at -0.15 V, followed by NS-rGO and 2Co/NS-rGO, where the high current of Co/NS-rGO possibly originated from better oxygen adsorption on the catalyst surface[122]. Since 2Co/NS-rGO, Co/NS-rGO, and NS-rGO give -3.8, -5.6, and -5.8 mA/cm^2 current density at the potential of pseudo-limiting current, Co/NS-rGO and NS-rGO approach to 4e$^-$ transfer whereas 2Co/NS-rGO is closer to 2e$^-$ transfer because at given 1600 rpm rotation rate and 0.196 cm^2 surface area 4e$^-$ transfer requires -58 mA/cm^2 of current density according to Levich equation[222] (eq. 2 Supplementary). As discussed by Chlistunoff, we do not link the comparingly high Tafel slope (150-210 mV/dec) of our catalysts with either non-efficient catalyst utilization, conductivity problems, or mass transport losses. Still, we associate it with their intrinsic ORR activities[122]. It is postulated that the porous electrodes can exhibit a two-fold Tafel slope of the non-porous electrodes, and peroxide presence can promote high Tafel slope values, too[122], [223]. Considering the high porosity of our materials and current density limitation by peroxide decomposition rate, we postulate that the Tafel slopes of our materials either need to be compared to other porous electrodes or evaluated with an internal reference. We observed the lowest Tafel slope (Fig. 3-7b) for Co/NS-rGO, which refers to the fastest electron transfer rate and better oxygen adsorption properties[122], [224]. In contrast, the low Tafel slope of NS-rGO negligibly changes with Co incorporation to 2Co/NS-rGO.

To elucidate the electron-transfer mechanism (n_e^-) for the reaction, the rotating ring disk electrode (RRDE) method is utilized, considering the critical role of RRDE on kinetic investigations in porous electrodes (Fig. 3-6d)[145]. RRDE technique uses the principle of oxidizing and quantifying HO_2^- that is produced during ORR by setting the ring potential to 1.1 V. RRDE results (Fig. 3-6d, 3-7c) show that NS-rGO requires high current loads to drive 4e$^-$ electron transfer whereas Co/NS-rGO shows Pt/C-like behavior, and the number of transferred electrons is in the 4e- vicinity for all the studied potential range for this catalyst, which makes it a competitive catalyst for PEMFC operations[156]. Also, while the ring current decreases for NS-rGO and Co/NS-rGO below 0.5 V, it increases

for 2Co/NS-rGO, indicating that the catalyst facilitates HO_2^- production in this potential range (Fig 3-7c). Also, 2Co/NS-rGO produces neither a high amount of HO_2^- nor follows a 4e$^-$ pathway in the whole potential range, making it an insufficient catalyst for PEMFC operation and peroxide generation. Since Co/NS-rGO behaves like an n-type semiconductor and is not dominated by metallic properties, the catalyst may follow a non-coupled proton-electron transfer (non-CPET) mechanism. Also, on the semiconducting surface, the initial reduction of $O_{2(aq)}$ to $O_{2(aq)}^-$ through the outer-sphere mechanism might be the rate-determining step followed by adsorption of O_2^- on a semi-metallic surface[65].

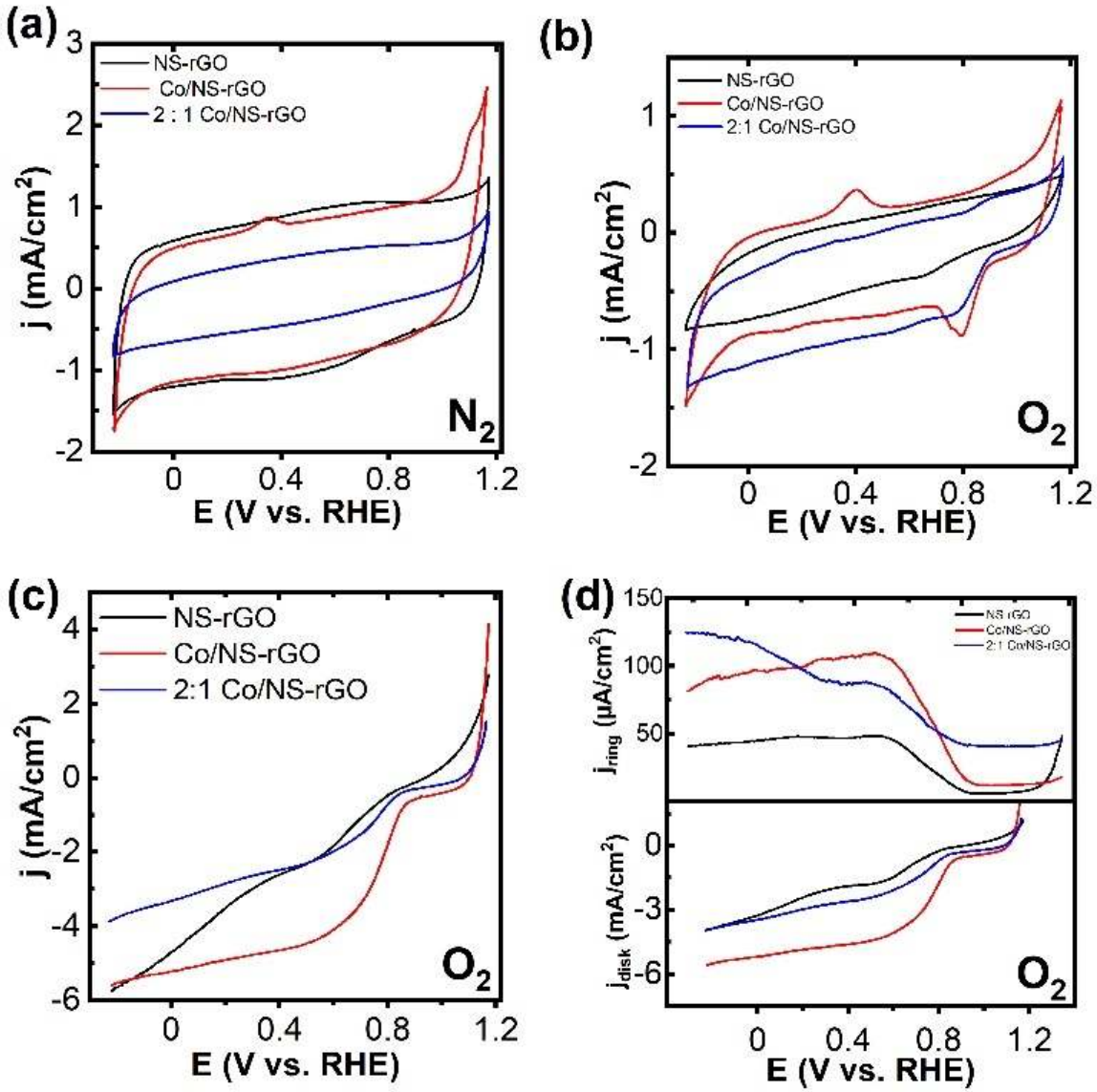

Figure 3-6 Electrochemical Characterizations. Electrochemical Characterizations. a) CV in N_2-saturated electrolyte. (b) CV in O_2-saturated electrolyte. (c) RDE in O_2-saturated electrolyte. (d) RRDE in O_2-saturated electrolyte..

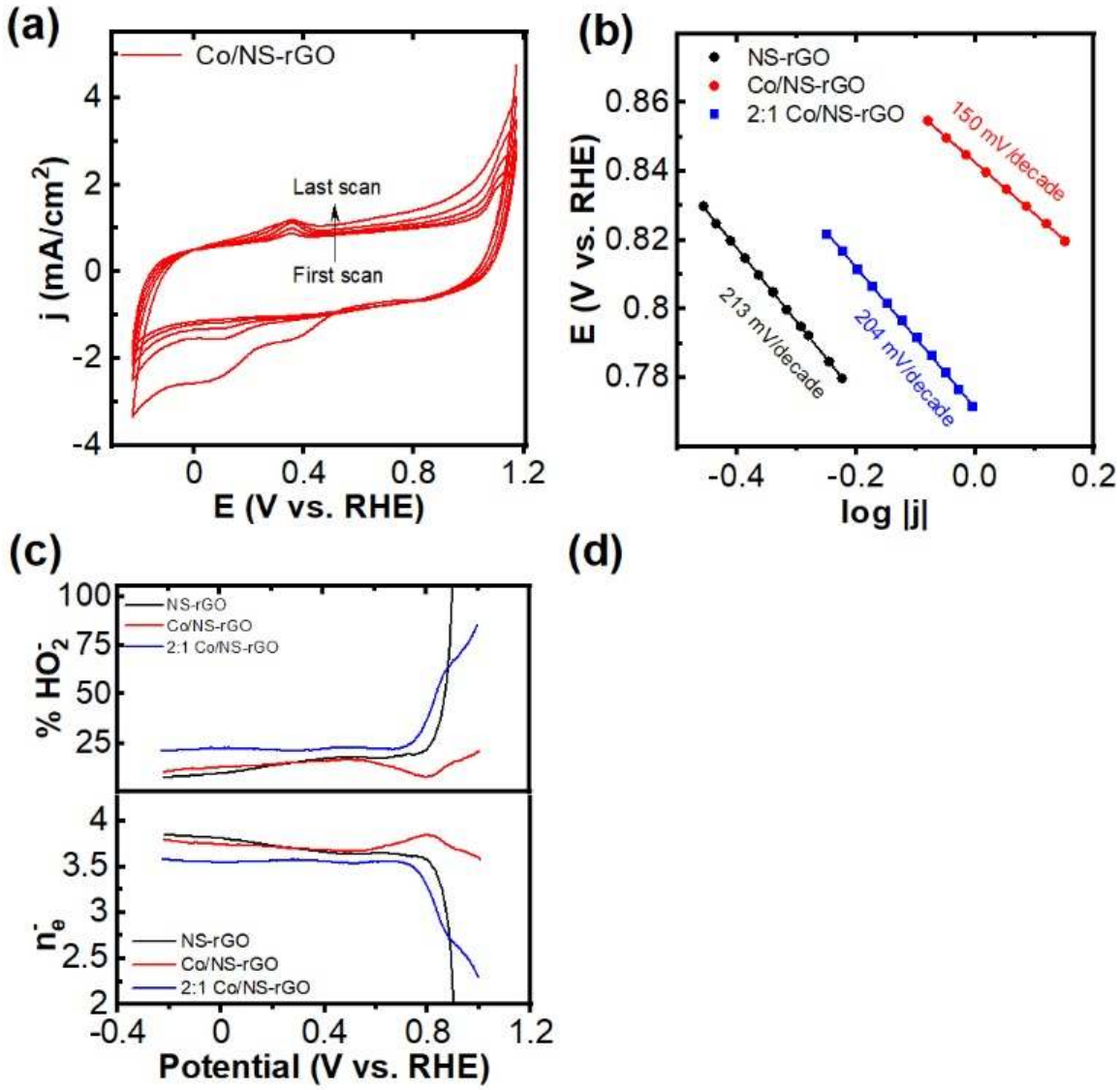

Figure 3-7 Electrochemical activity tests. a) CV in in O_2-saturated electrolyte. b) Tafel slope analysis of RDE in O_2-saturated electrolyte. c) RRDE in O_2-saturated electrolyte.

Capacitive measurements further unravel the electrocatalysts' high porosity and unique ORR behavior. Double-layer capacitance (C_{dl}) values are measured with different scan rates, and the materials' electrochemical surface area (ECSA) is calculated by taking the C_s value as 0.022 mF/cm^2 [157]. We observed that the ECSA after cobalt incorporation is decreased for both catalysts (Fig. 3-8a). Still, Co/NS-rGO obtains a higher ECSA than 2Co/NS-rGO, which can be linked to its superior ORR activity (Fig. 3-9a). Furthermore, the ECSA normalized RDE and RRDE results show that the Co/NS-rGO has the superior intrinsic activity for ORR (Fig. 3-9a, b). In contrast, despite NS-rGO having the highest ECSA, the worst ECSA normalized ORR activity indicates poor ORR performance.

Furthermore, metal mass activity normalized RDE and RRDE graphs (Fig. 3-9 c, d) show that the Co/NS-rGO catalyst has far superior ORR activity compared to 2Co/NS-rGO originating from the superior metal utilization of the catalyst. Since ORR activity originates from the electronic properties of the material, change in ORR behavior of the electrodes is elucidated by the density of states (DOS), flat-band potential (V_{fb}), and doping density (N_D) values, which are derived from electrochemical impedance spectroscopy (EIS) measurements[131], [159].

EIS measurements in Fig. 4b are performed around the onset potential in N_2-saturated electrolytes. R_1 is assigned to equivalent series resistance (ESR), which emerges from solution resistance and electrical connections. Constant-phase element (CPE) Q is used for modeling instead of C owing to the non-ideal behavior of the materials[158]. Q_1 is assigned to the total double-layer capacitance build-up in the electrode-electrolyte interface, where R_2 is the corresponding resistance. Bending in the high-frequency region is denoted as equivalent distributed resistance (EDR) that arises from ion transport to the electrode surface[225]. 2Co/NS-rGO holds a significantly higher EDR value than other samples, possibly due to the stacking emerging from the high amount of cobalt in the catalyst. W_1, Warburg impedance, is assigned to the low-frequency behavior of the samples associated with the mass transfer process in the catalysts[158]. Since the selected potential is in close vicinity with the potential of electron transfer for ORR, the density of states around the Fermi level ($D(E_F)$) is calculated for each catalyst at a given potential (eq. 8 supplementary) [159], [226], [227]. The highest ($D(E_F)$) value of 2.75×10^{22} eV^{-1} cm^{-3} (Table 1) is observed for Co/NS-rGO, indicating the highest concentration of electronic states around the Fermi level possibly due to the presence of CoS species[228] and agrees with the superior kinetic behavior of the sample towards ORR. However, a high amount of Co for 2Co/NS-rGO decreased $D(E_F)$, which led to slower ORR kinetics.

Mott-Schottky measurement is carried out to analyze the samples' capacitive behavior further (Fig. 3-8c). Firstly, it is found that all the materials show n-type semiconductor behavior. Materials have attained n-type semiconductor properties, possibly due to the presence of N, S, and O species along the graphene basal plane[65]. N_D normalization uses ECSA instead of BET surface area to include active sites specific to electrochemical activity. It is observed that the Co/NS-rGO has the highest N_D value, indicating that the catalyst obtains the highest carrier concentration to perform ORR,

which signifies its superior ORR kinetics (Table 3-1). According to eq. 10, the highest V_{fb} is observed for Co/NS-rGO, whereas a sharp decrease in V_{fb} is detected for 2Co/NS-rGO (Table 3-1). The V_{fb} trend agrees with RDE results, which show the lower overpotential of Co/NS-rGO required to perform oxygen electroreduction[159].

The capacitance versus potential graph (Fig. 3-8d) shows the highest total double-layer capacitance (C) for Co/NS-rGO and the lowest C value for 2Co/NS-rGO. A decrease in capacitance in potentials positive of V_{fb} verifies the materials' n-type semiconductor properties[132].

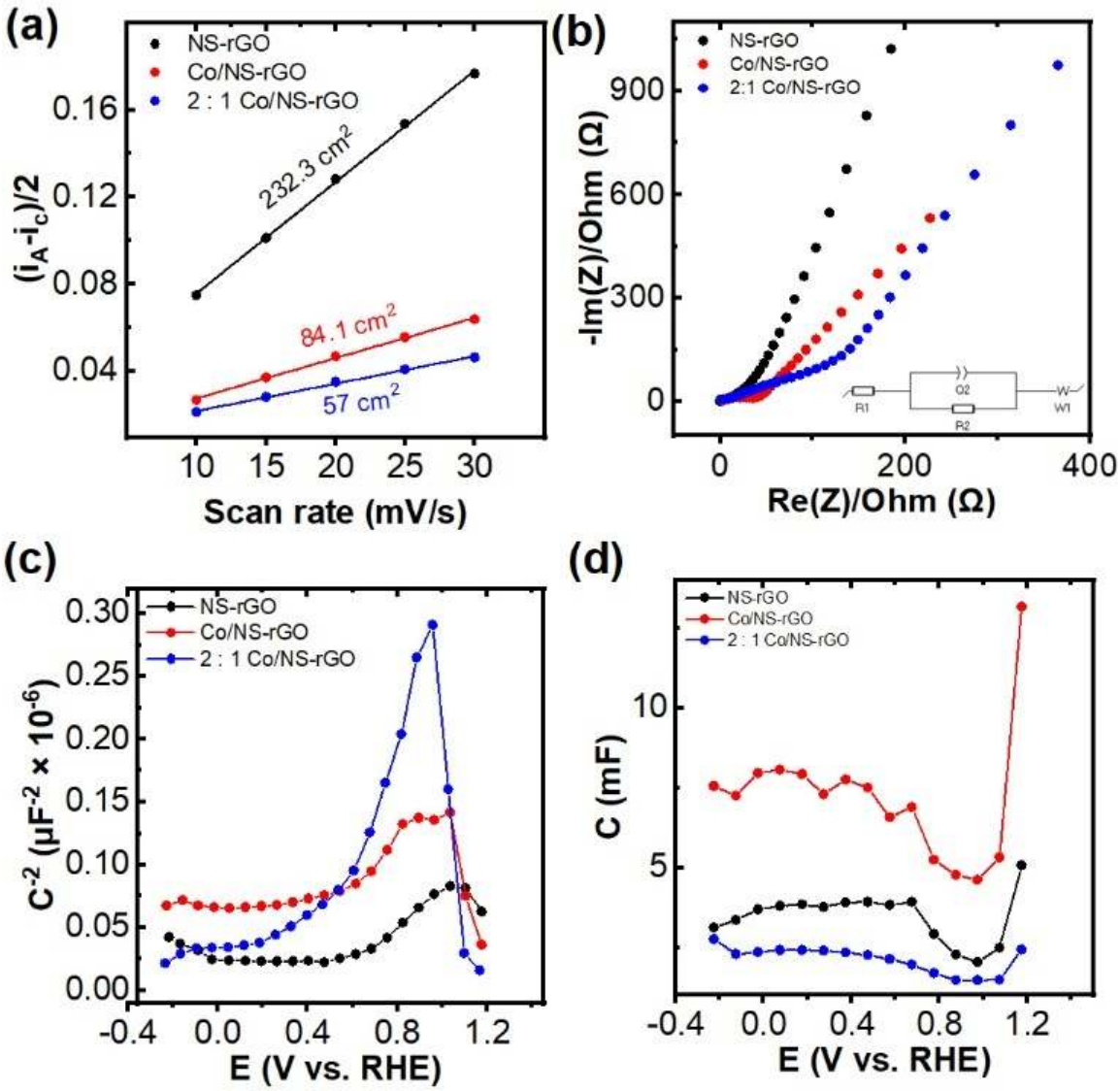

Figure 3-8 Electrochemical screenings using voltammetry and impedance techniques. a) ECSA in N_2-saturated electrolyte. b) EIS in N_2-saturated electrolyte. c) Mott-Schottky in N_2-saturated electrolyte. d) Capacitance measurements in N_2-saturated electrolyte.

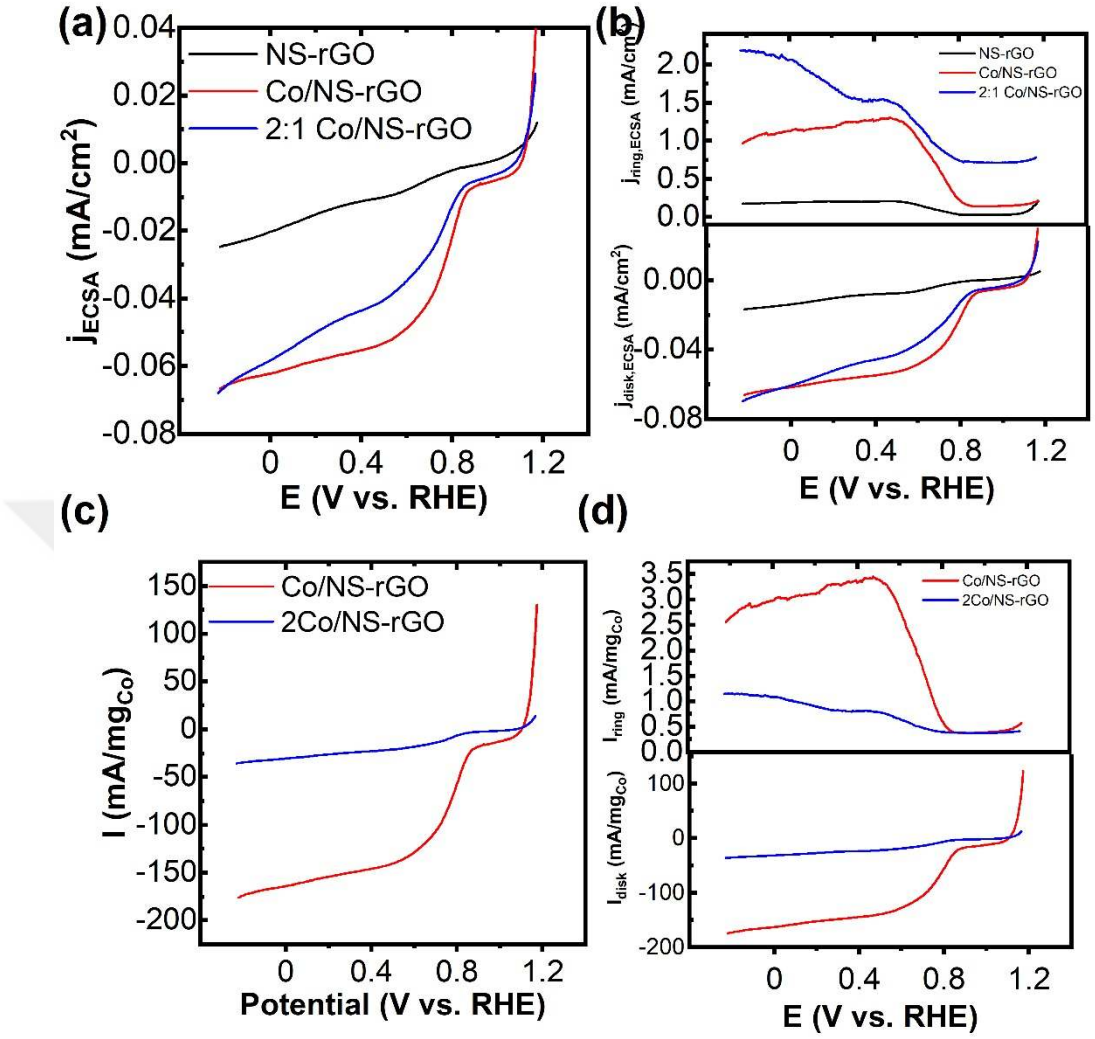

Figure 3-9 ECSA normalized electrochemical activity tests. a) ECSA normalized RDE in O_2-saturated electrolyte. b) ECSA normalized RRDE in O_2-saturated electrolyte. c) Metal mass activity normalized RDE. d) Metal mass activity normalized RRDE.

	$D(E_F)$ [eV^{-1} cm^{-3}]	Carrier Density (N_D) [cm^{-3}]	Flatband Potential (V_{fb}) [V]
NS-rGO	2.43×10^{22}	4.76×10^{25}	0.865
Co/NS-rGO	2.75×10^{22}	2.66×10^{26}	0.891
2Co/NS-rGO	2.17×10^{22}	2.2×10^{26}	0.666

Table 3-1 Electronic properties of density of states, carrier density, and flatband potential for the materials

3.5 Conclusion

Herein, we develop Co/NS-rGO and 2Co/NS-rGO catalysts with 1:2 Co content, CoS presence, and Co SA distribution along the graphene plane. With an optimum cobalt amount, the Co/NS-rGO catalyst would show lower overpotential and R_{ct}, higher ECSA, current density, and capacitance values. In contrast, the opposite happens when more cobalt is used for 2Co/NS-rGO. When the electronic properties of the catalysts are investigated through EIS techniques, it is found that catalysts show n-type semiconductor behavior and higher flatband potential, density of states, and carrier concentration. CoS formation is found using the XPS technique, while HR-STEM shows the distribution of Co SAs on the N, S-rGO matrix. Synergistic effects between CoS, Co SAs, and the NS-rGO basal plane are related to the catalyst's higher ORR activity.

Chapter 4:

Mechanistic Insights into Nitrate-to-Ammonia Electroreduction Through Constant and Pulsed Electrolysis Using Co/NS-rGO Catalysts

4.1 Introduction

4.1.1 Electrification of NH_3 Production Using Waterborne N-Species

Ammonia (NH_3) is a vital carbon-free energy carrier and a chemical commodity for its intensive use in (1) fertilizers to supply nutrition for the increasing human population[229], (2) pharmaceutical and heavy industry[9], [230], and (3) energy storage owing to its high energy density[13], [231]. However, the energy-intensive Haber-Bosch (H-B) process accounts for 90% of the annual global NH_3 production[232] and approximately 1.8% of the worldwide CO_2 emission[233]. The disruptive impact of the H-B process on the N-cycle due to anthropogenic activities has led to a significant shift in focus towards the green electrochemical synthesis of NH_3 through the reactive N-species, offering a promising alternative[133], [234], [235]. The electrochemical nitrogen (N_2) reduction reaction (NRR) presents an alternative route for sustainable and environment-friendly NH_3 production[236]. However, despite the intensive efforts[126], [237], [238], [239], [240], [241], [242], [243], [244], NRR suffers from poor NH_3 selectivity and two orders of magnitude lower yield rate than the H-B process[236] due to the high disassociation energy of N≡N bond (945 kJ mol^{-1}) in N_2[245], the low solubility of N_2 in aqueous electrolytes, and the presence of the competing hydrogen evolution reaction (HER) around the similar thermodynamic reduction potential[246]. Also, the quantification challenges in NRR experiments due to NH_3 contamination raise the question of the reliability and reproducibility of the NRR literature[247]. Furthermore, using Ultra-high vacuum systems in high-performance NRR studies may reflect the difficulty of producing scalable NH_3 at room T by reducing N_2[237], [243], [244]. When the bottlenecks of NRR are considered, potential solutions using different reactive N-species, i.e., NO_3^-, NO_2^-[248], for green and scalable ambient

electrochemical NH_3 synthesis, have emerged, offering an optimistic outlook for a more sustainable NH_3 production[249].

An abundance of nitrate (NO_3^-) ions exists in (1) agricultural runoffs due to overfertilization practices, (2) sewage, and (3) industrial wastewater streams, which cause significant pollution of surface water and underground aquifers[233]. Excessive nitrate contamination significantly threatens human health and the ecosystem[234], [250]. It causes the formation of eutrophication in wildlife, methemoglobinemia, and cancer in humans with their presence in drinking water[251]. Being hazardous to human health and the environment, there has been immense research on eliminating waterborne N-species through water remediation and denitrification[252]. These studies consider NH_3 an unwanted product since they aim to produce N_2 by reducing nitrate and purifying the water. On the other hand, one can have a sustainable NH_3 production route by capturing and isolating NO_x^- species abundant in wastewater and converting them into economically valuable NH_3. This autonomous system can effectively eliminate nitrate species' detrimental effects and produce NH_3 to compensate for the H-B process[253]. On top of the environmental merits, NO_3^- has a significantly lower disassociation energy of N=O bond (240 kJ mol^{-1}) and very high solubility in aqueous solutions[249], [254]. Furthermore, the recent low-energy plasma technologies that produce NO_3^- from the air add to its widespread availability[255].

4.1.2 Biological Insights into Electrochemical NO_3RR

In microorganisms, NO_3RR is carried out by a tandem process where nitrate-to-nitrite reduction is carried out by S-containing Mo-cofactors and nitrite-to-ammonia reduction is carried out by S-containing Fe and Cu-cofactors separately[256]. Many studies that mimic biological NO_3RR can achieve high NH_3 selectivity and yield. Ren et al. used a bioinspired approach where they studied Cd single-atom anchored $Mo_2TiC_2T_x$ catalyst to achieve >95% Faradaic efficiency (F.E.) and 48.5 mg h^{-1} cm^{-2} NH_3 yield rate by activating NO_3^- by Mo active center as of nitrate reductase and suppressing HER simultaneously[108]. Murphy et al. utilize a FeMo-N-C atomically dispersed catalyst that follows a cascade NO_3RR pathway through associative and disassociative adsorption of NO_3^-. They could effectively adsorb and reduce NO_3^- at Mo-N_4 sites to desorbable NO_2^- and *NOOH to NH_3 on Fe-N-C. The catalyst achieved 94% F.E. and a

high stability of 90% F.E. for 60 h[109]. Abbott et al. achieved 41% F.E. and 12.9 μmol $h^{-1}mg^{-1}$ using Mo_2CT_x: Fe through NO_3^- binding to vacancies promoted by Fe sites and further reduction to NH_3[257].

4.1.3 Electrochemical NO_3RR: Electronic Properties and The Effect of Pre-reduction

The material's electronic properties are significant for NH_3 production, especially in NO_3^- adsorption and water disassociation to form protons. Li et al. investigated the adsorption characteristics of the intermediates on Cu sites by projected partial density of states (PDOS) calculations. PDOS results showed that the Cu-NO_2 model exhibited higher energies of electrons than Cu-NO_3 and Cu-H_2O by the positive shift in Cu d orbital. This shift signified the better activation of the NO_2 adsorbed species for NO_3RR[258]. Similarly, Zhou et al. examined the material's electronic structure using PDOS, where the interaction between Cu and Co in the alloy allows spontaneous NO_3^- reduction and showed that H_2O disassociation is the rate-determining step for the reaction[144]. Carvalho et al. described through the electronic structure analysis that the NH_3 selectivity increases when H^* binding affinity is enough to reduce the NO_3^- while not contributing to HER. Also, materials' selectivity towards NH_3 increases when d-band center energy (E_d) approaches or overcomes the Fermi level E_f[259].

The NO_3RR literature does not comprehensively examine pre-reduction effects except for synthesis[99] or control experiments[260]. In contrast, pre-reduction is extensively studied on CO_2RR[127], [261], [262], [263] and ORR[264], which is applied to remove the oxide layer or O content, high surface roughness, and better kinetics.

4.1.4 Pulsed Electrolysis of NO_3RR-to-NH_3

Recently, pulsed electrolysis has been commonly studied to increase NH_3 yield and F.E. by causing morphological or oxidation state changes in the material[265] or modulating the NO_3^- to NH_3 mechanism. Pulsed electrolysis was used with cathodic and anodic potentials in multiple articles to denote the contribution of reconstruction of the catalyst to higher nitrate-to-ammonia activity[266]. In one study, oxidative and

reductive potentials are applied in a pulsed fashion to lower interfacial pH and replenish the electrical double-layer (EDL). However, they found that the lower interfacial pH promoted HER and caused nitrite selectivity to increase. Also, they argue that the N-selectivity can be changed due to nitrite desorption and prevent NH_3 electrosynthesis[134]. Another article proposes that the positive bias in electrode potential allows more nitrate accumulation on the electrode and more NH_3 production[267]. On the other hand, Li et al. applied negative potentials to modulate NO_3^- – NO_2^- - NH_3 modulation. They could confine NO_2^- in the high -0.8 V pulsed potential, suppress HER by NO_2^- to NH_3 reduction, and achieve high NH_3 F.E. through tandem NO_3^- to NH_3 reduction[258].

4.1.5 Aims of Study

Here, we use a cobalt-decorated Nitrogen, Sulfur-doped reduced Graphene Oxide (Co/NS-rGO), and Co/NS-rGO 900 catalyst. The former consists of CoS catalytic pairs in an N, S doped graphene structure, while the latter has a disrupted carbon structure enriched with CoO species. We investigated the effect of CoS and CoO species to promote NO_3RR and NO_2RR through potentiostatic and pulsed electrolysis experiments. We utilized pulsed potentials to examine the impact of more negative potentials to drive confined NO_2^- to NH_3 reduction by enabling water disassociation via inferior H* adsorption without promoting HER or less negative potentials to investigate the dominance of N-O bond cleavage and NO_2^- accumulation. We used electrochemical Tafel analysis to understand whether a chemical, adsorption, or electron transfer step occurs on different potentials. Furthermore, we proposed two different mechanisms for two different Co catalysts using XAS (X-ray absorption spectroscopy), EIS (Electrochemical impedance spectroscopy), and DRT (Distribution of relaxation times)[268] model principles.

4.2 Experimental Method

4.2.1 Synthesis of NS-rGO, NS-rGO 900, Co/NS-rGO, Co/NS-rGO 900 Catalysts

Graphene Oxide (GO) is synthesized using improved Hummer's method. Nitrogen-Sulfur doped reduced Graphene Oxide (NS-rGO) catalyst is synthesized by autoclave of 1:5 GO and Thiourea mixture at 190 °C for 18 h through a hydrothermal method.

Cobalt decorated NS-rGO (Co/NS-rGO) catalyst is synthesized by drying the 1 mL Co-DMF precursor and 1:1 NS-rGO and DMF solution at 90 °C. NS-rGO 900 and Co/NS-rGO 900 electrocatalysts are synthesized by the 1 hour pyrolysis of NS-rGO and Co/NS-rGO in N_2 environment for 1 h.

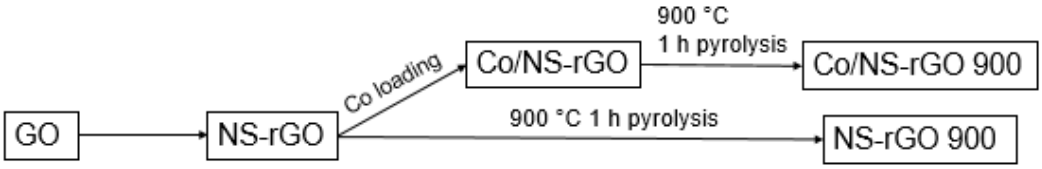

Figure 4-1: Classification of Electrocatalysts

4.2.2 Structural Characterizations

X-ray diffraction (XRD) measurements are performed using a Bruker D2 Phaser X-ray Diffractometer records equipped with a Cu Kα radiation with 10 kV potential and 30 mA current. Transmission electron microscopy (TEM) images are taken using 200 kV aberration-corrected FE-TEM/STEM Hitachi HF5000 device. Scanning electron microscopy (SEM) images are attained using A 20 kV Zeiss Ultra Plus microscope. Thermo K-alpha instrument that has monochromatized Al Kα (1486.7 eV) radiation is used to carry out X-ray photoelectron spectroscopy (XPS) results. The Raman spectroscopy is carried out using a Renishaw INVIA device at the laser wavelength of 532 nm. XAS measurements are carried out in SESAME (Synchrotron-light for Experimental Science and Application in the Middle East) XAS device with energy range of 3-30 keV and counting rate of minimum 3.2 Mcps.

4.2.3 Electrochemical Tests

NO_3RR and NO_2RR experiments are carried out in 0.1 M KOH + 0.1 M KNO_3 or KNO_2 electrolytes in both anodic and cathodic compartments that are separated by a Nafion membrane. An H-cell with conventional three electrode configuration having Ag/AgCl reference electrode, Pt counter electrode and coated Glassy Carbon electrode with catalyst loading of 2.122 mg/cm^2 is used for electrochemical NH_3 production experiments. H_2 detection experiments are carried out using a Gas Chromatography device with thermal conductivity detector (TCD) while NH_3 and NO_2^- detection experiments are performed using UV-Vis Spectroscopy by Indophenol Blue Method

and Griess' Test respectively[8]. The iR compensation and all EIS measurements was carried out at 85% and 100 kHz using either a Biologic SP-200 or VSP-300. Also, pulsed CA measurements are carried out at a fixed potential of -0.9 V or -0.4 V and one potential between -0.2 V to -1.2 V at each potential for 2 s by summing up to 30 mins.

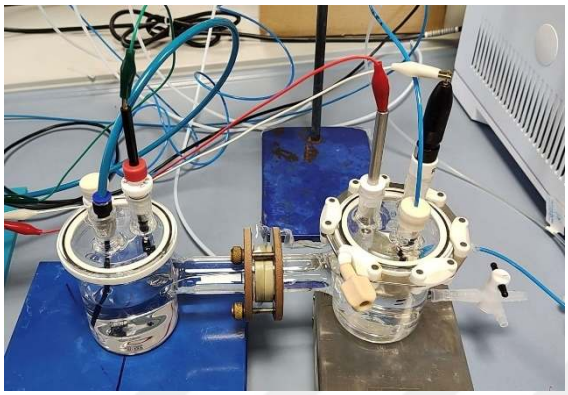

Figure 4-2: H-Cell Configuration

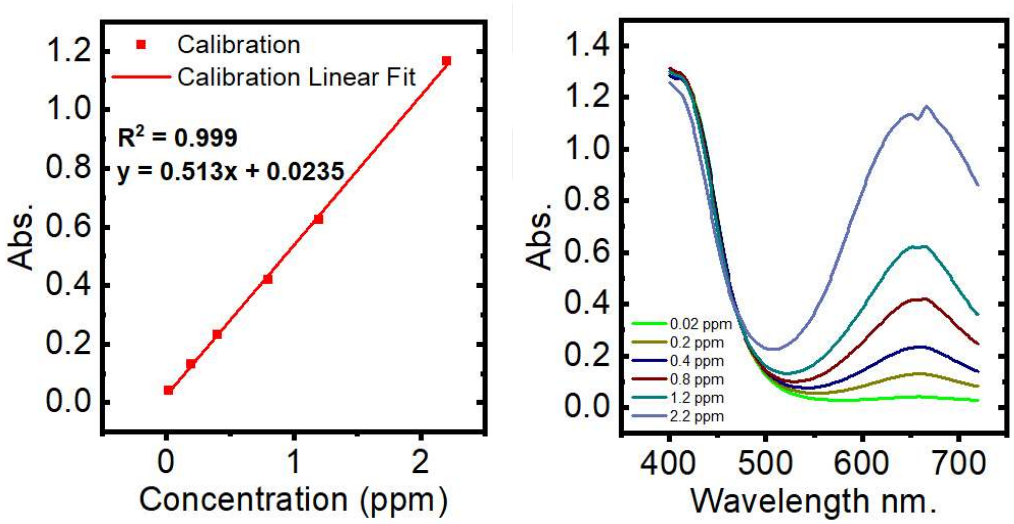

Figure 4-3: NH_3 Calibration using Indophenol Blue Method

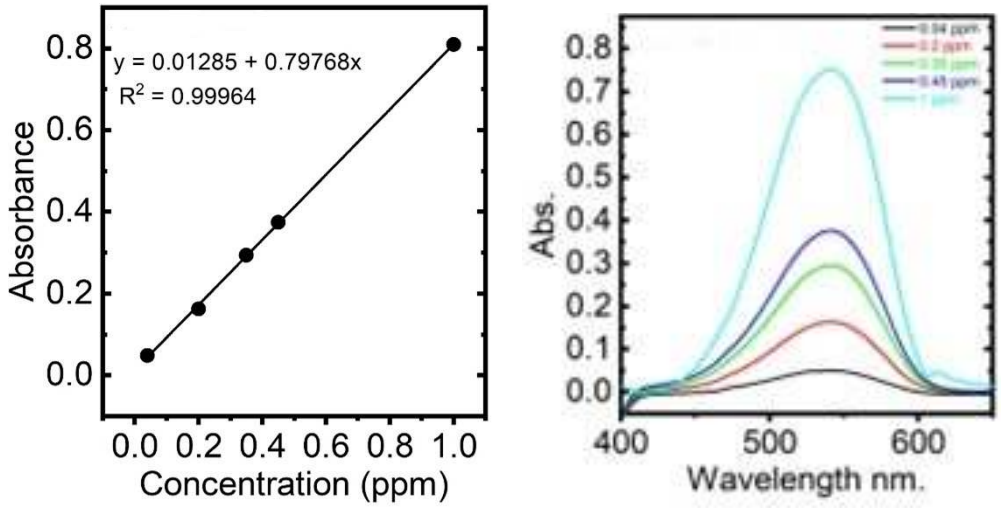

Figure 4-4: NO_2 Calibration using Griess' Test

4.3 Surface Characterization of Co/NS-rGO Through XPS and XAS Techniques

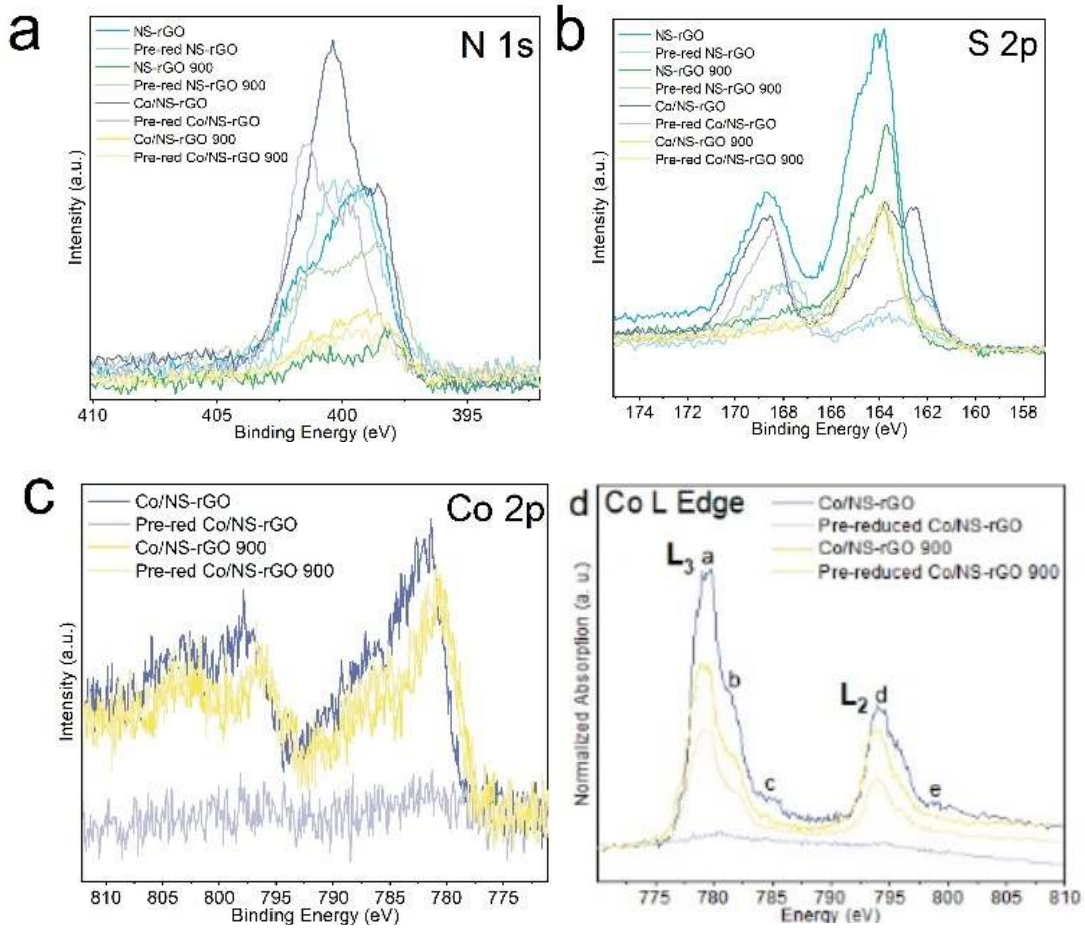

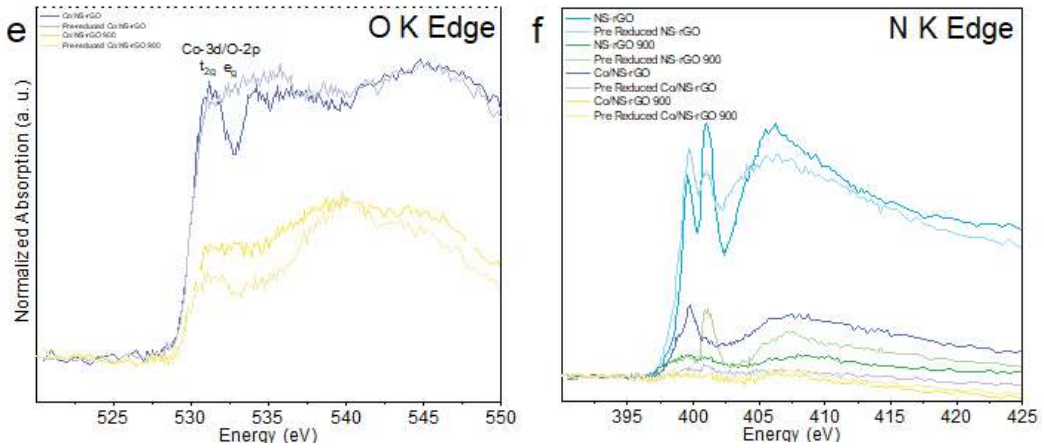

Figure 4-5: Structural Characterizations of Pre-reduced and bare samples. a) XPS N1s. b) S 2p. c) Co 2p. d) XAS Co L-Edge. e) XAS O K-Edge

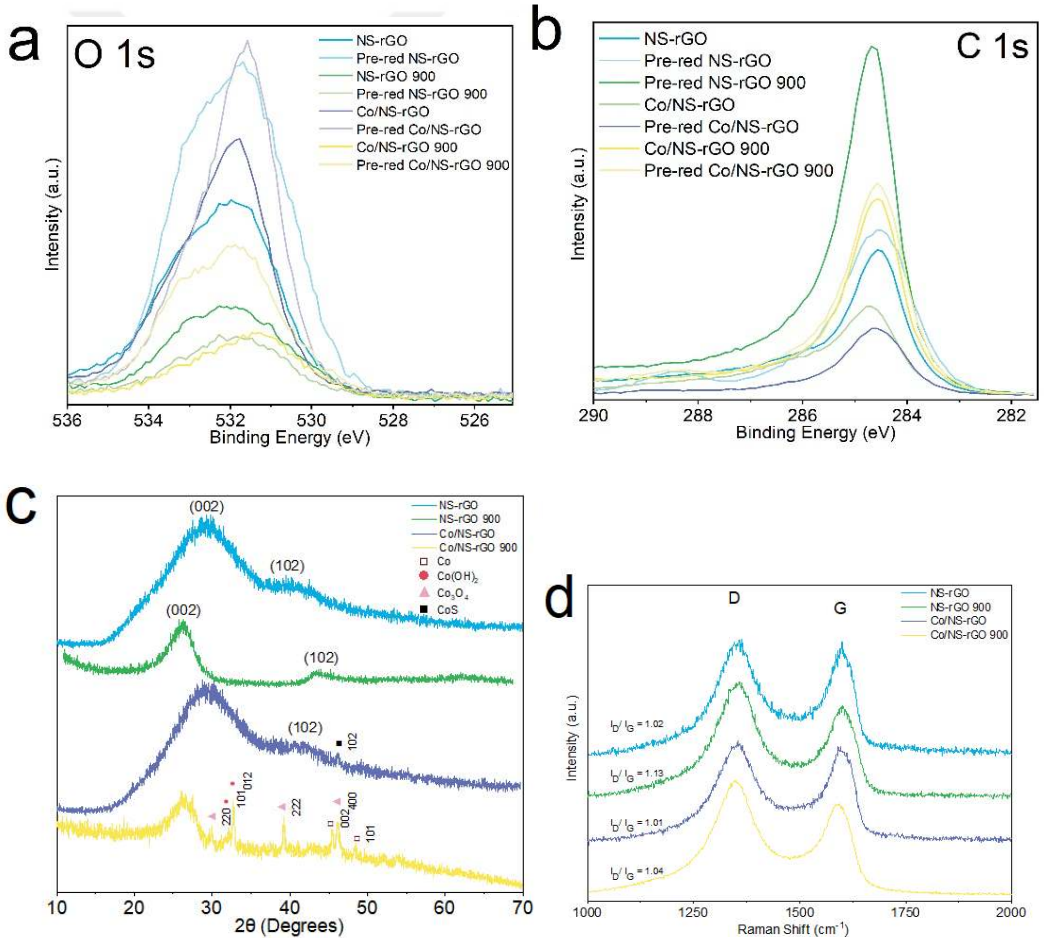

Figure 4-6: a) XPS O 1s Spectra, b) C 1s Spectra, c) XRD d) Raman Spectra

Sample	$I(L_3)$	$I(L_2)$	$I(L_3)/ I(L_2)$	$I(L_3)/ I(L_3)+ I(L_2)$

				Branching Ratio
Co/NS-rGO	0.535	0.274	1.953	0.661
Pre-red Co/NS-rGO	0.0278	0.00742	3.747	0.789
Co/NS-rGO 900	0.352	0.226	1.558	0.609
Pre-red Co/NS-rGO 900	0.262	0.131	2	0.667

Table 4-1: Co L-Edge Peak Intensity and Branching Ratio

The N 1s spectra show that Co/NS-rGO obtains pyridinic and pyrrolic N after Co incorporation to NS-rGO through surface functionalization. At the same time, the other samples primarily inherited their N-character from NS-rGO. Furthermore, the pre-reduction induced N-species with higher oxidation energies for all samples (Fig. 4-5a). The S 2p spectra show the emergence of a doublet peak for Co/NS-rGO around 162-164 eV, which indicates the formation of CoS in the catalyst. On the other hand, the S behavior of NS-rGO stays the same after the sample is subjected to either T or Co incorporation, only T treatment eliminating the sulfate content. Furthermore, S 2p spectra show that Co/NS-rGO preserves its CoS species even after pre-reduction (Fig. 4-5b). The Co 2p spectra in XPS show that the Co^{3+}/Co^{2+} ratio increases after T treatment even though the catalyst is Co^{2+} rich. An increase in C 1s peak intensities (Fig. 4-6a.) and I_D/I_G ratio in Raman Spectra and a decrease in O 1s peak intensities (Fig. 4-6b.) is observed after T treatment. Also, peak intensities in O 1s for pre-reduced samples are attributed to the presence of H_2O in the sample after the interaction with the electrolyte. The I_D/I_G ratio increase shows the presence of defects in the graphene plane. XRD patterns (Fig. 4-6c.) show the presence of (002) graphene plane for all samples. However, narrower peaks for NS-rGO 900 and Co/NS-rGO 900 imply the existence of a more graphitized structure, while broader peaks for the remainder show the presence of a few-layer graphene for these materials[269], [270]. The presence of (102) graphene layers, which indicates the short-range order in stacked layers, is also present in all samples except Co/NS-rGO 900. This finding also agrees with the disruption of the graphene plane for Co/NS-rGO 900. On the other hand, the presence of (220), (222), and (400) planes of Co_3O_4[271], (101), (012) planes of $Co(OH)_2$, and (002), (101) planes of Co[272] and disappearance of (100) plane is observed for Co/NS-rGO 900.

In Co L edge XAS (Fig. 4-5d), an increase in the $I(L_3)/ I(L_2)$ peak intensity ratio and the emergence of c and e peak for Co/NS-rGO shows the presence of CoS in the catalyst[153]. Furthermore, a higher $I(L_3)/ I(L_2)$ ratio indicates higher electron occupancy in the d orbital, and higher branching ratios refer to a high spin state (HS) while a low spin state (LS) for the opposite case[273]. It is important to note that the occupied d orbitals can cause weak binding of NO_x^- species due to high electron-electron repulsion[274]. Also, for example, the HS Co^{2+} in Co/NS-rGO can induce weak Co-O bond formations and suffer from low NO_x^- adsorption, while LS Co^{2+} in Co/NS-rGO 900 can facilitate strong Co-O bonds and facilitate NO_x^- adsorption, but the protonation becomes difficult. In addition, pre-reduction increases d-orbital occupancy and allows transition to higher spin states for both electrocatalysts.
O K-Edge XAS spectra (Fig. 4-5e) refer to the hybridization between Co 3p orbitals and O 2p unoccupied density of states by the fact that as peak (t_{2g}) intensity at 531 eV increases the peak intensity at (e_g) decreases and vice versa. For Pre-red Co/NS-rGO, a decrease in t_{2g} peak intensity induces an increase in the, e.g., peak intensity and an electron exchange from, e.g., orbitals to $t_{2g,}$ which causes higher d orbital occupancy, which is also shown by Co L-Edge peak intensity analysis[275]. A similar phenomenon of electron exchange between N_{Py} and, e.g., orbitals is observed for N K-Edge, corresponding to peaks of 399.8 and 401 eV consecutively (Fig. 4-5f)[276].

4.4 Structural Characterizations of Catalysts

It is observed that NS-rGO has a well-preserved layered graphene structure after N and S bonding, where characteristics of graphene flakes and paper-like structure are visible (Fig. 4-7). Even though subjected to 900 C pyrolysis for 1 h, NS-rGO 900 also has graphene layers, and the effects of carbonization are visible (Fig. 4-8) which is further supported by CHNS analysis (Fig 4-10 a, b.) In Fig. 4-9b, the Co/NS-rGO HR-STEM image shows the graphene layers and distribution of Co atoms in the basal plane. Furthermore, Co/NS-rGO SEM EDX (Fig. 4-11 a, c.) shows the presence of CoS pairs, also proven by XPS S 2p spectra. Co/NS-rGO 900 SEM (Fig. 4-5d) shows the disruption of the graphene plane for Co/NS-rGO and the presence of cobalt oxide particles shown by SEM EDX (Fig. 4-11 b, d). Also, ICP-MS results show the ultra-low

Co content in the catalysts, which are 1.6% for Co/NS-rGO and 1.9% for Co/NS-rGO 900 (Fig. 4-10 c).

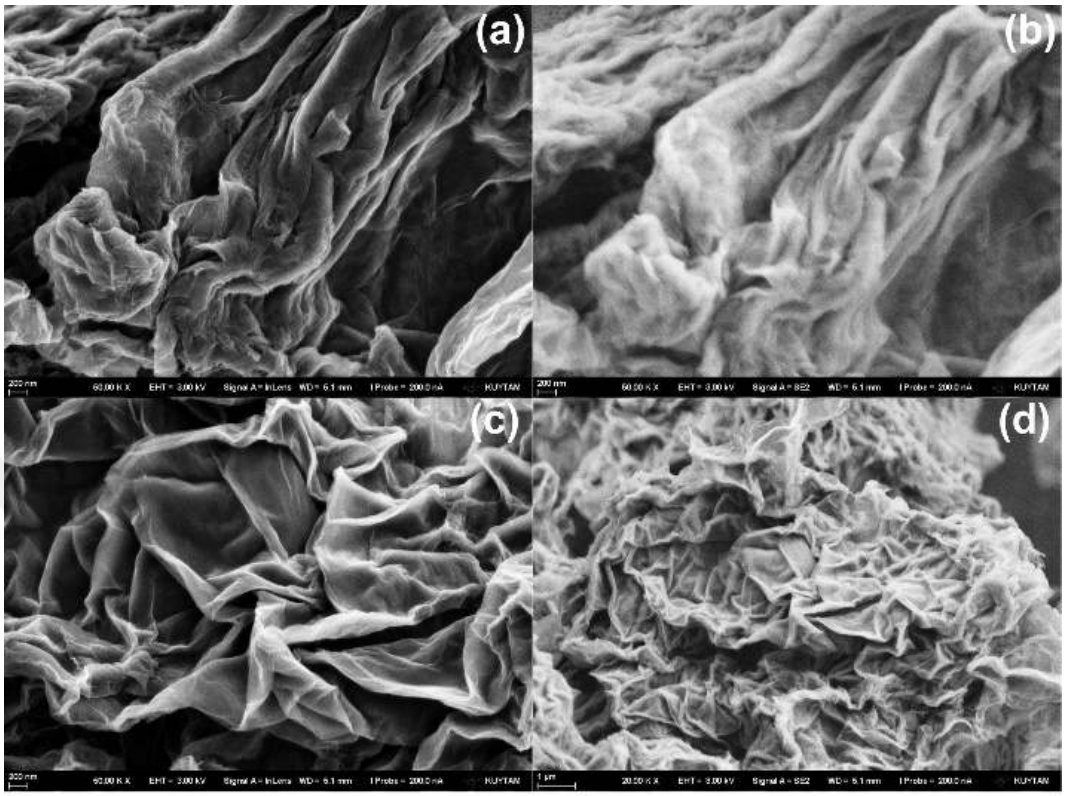

Figure 4-7: SEM images for NS-rGO

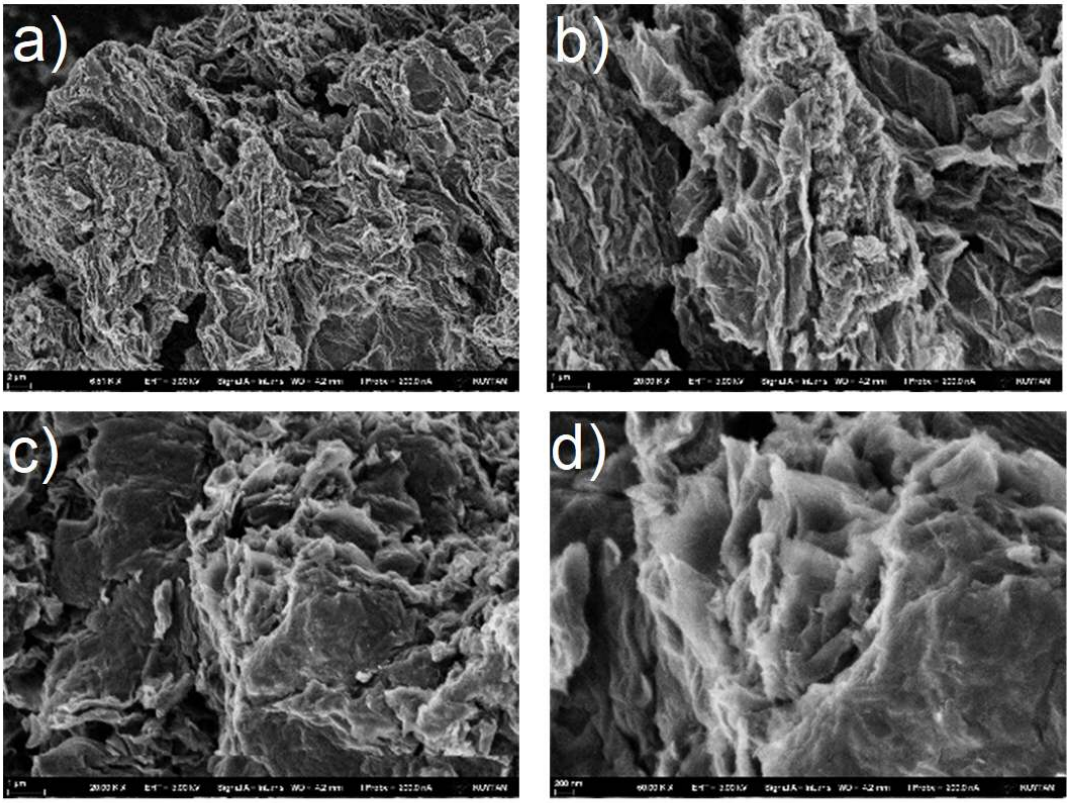

Figure 4-8: SEM images for NS-rGO 900

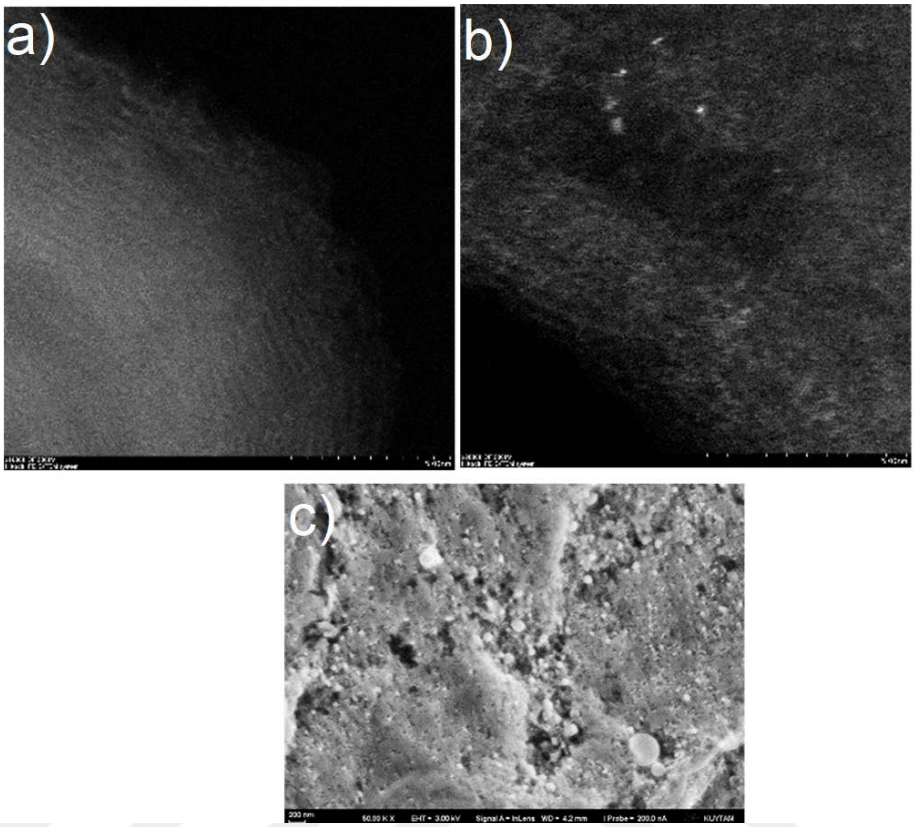

Figure 4-9: a, b) HR-STEM images for Co/NS-rGO. c) Co/NS-rGO 900 SEM

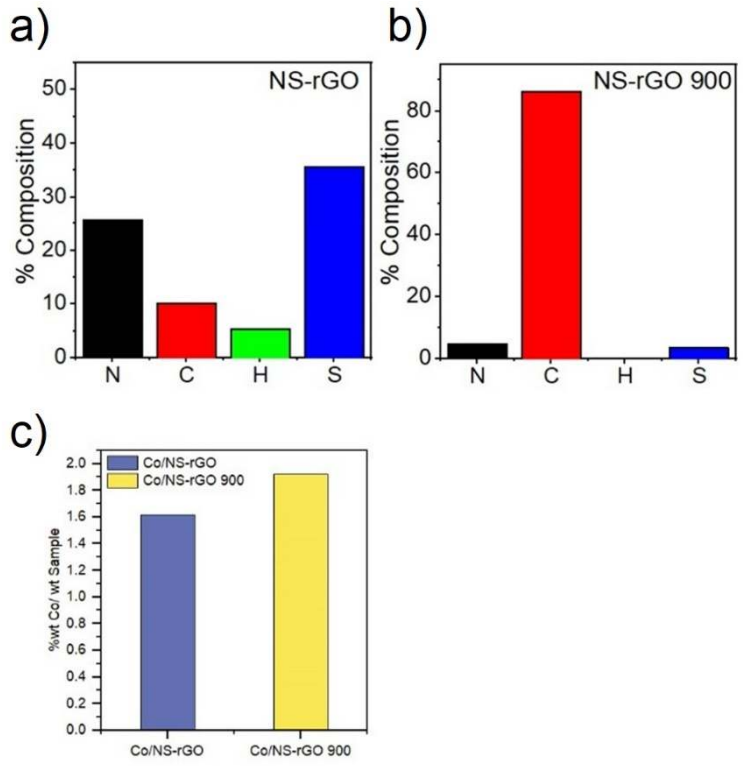

Figure 4-10: a) CHNS Analysis for NS-rGO and NS-rGO 900 b) ICP-MS for Co/NS-rGO and Co/NS-rGO 900

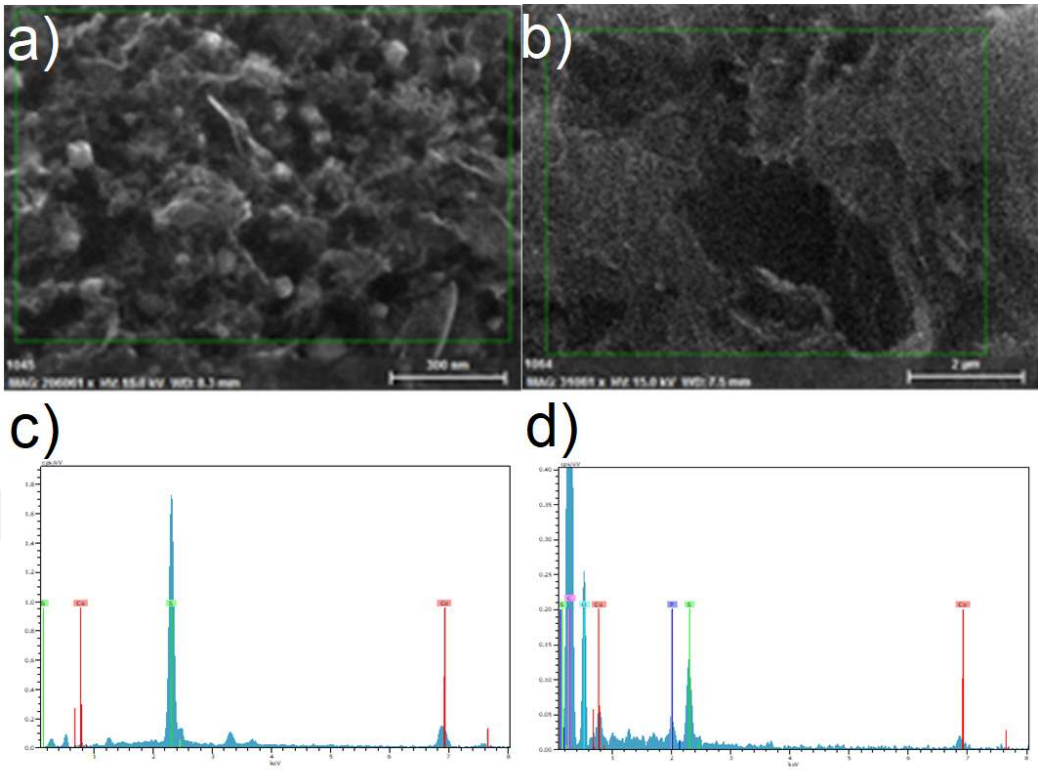

Figure 4-11: EDX Spectra, Microscopical Images, and ICP-MS. a) Co/NS-rGO area-specific SEM c) EDX b) Co/NS-rGO 900 area-specific SEM d) EDX

4.5 Tafel Analysis

LSV measurements show that except NS-rGO 900 NO_3RR, an already strongly reduced sample, pre-reduction allows a considerable decrease in overpotential. Furthermore, pre-reduction enables a plateau in the kinetic region for NS-rGO and Co/NS-rGO samples (Fig. 4-12a). It is observed that Co/NS-rGO 900 and Co/NS-rGO have the lowest overpotential for NO_3RR and NO_2RR respectively. Also, the lowest overpotential for HER belongs to Co/NS-rGO 900 and the highest to Co/NS-rGO (Table 2).
Tafel slope values indicate that only for pre-reduced NS-rGO and Co/NS-rGO 900 samples, RDS for NO_3RR is 1 e^- transfer for NO_3^- to NO_2^- reduction due to the slope being slightly lower than 120 mV^{-1}/decade. NO_3RR RDS for other catalysts is determined as the initial adsorption and activation of NO_3^- due to their higher Tafel slope values. For NO_2RR, NS-rGO and Co/NS-rGO 900 are limited by the binding of NO_2^-, while for NS-rGO 900, RDS is the NO_2^- to NO e^- transfer. Furthermore, the 72.08

mV/decade Tafel slope of Co/NS-rGO indicates that for Co/NS-rGO, RDS is a chemical step that can be the coupling of strong adsorption of intermediate, i.e., NO*, *H species. Tafel slopes for HER show that Co/NS-rGO 900 has the fastest kinetics for HER, while Co/NS-rGO has a significantly higher Tafel slope value[99]. Therefore, HER can suppress the NO_3RR activity of Co/NS-rGO 900 at lower overpotentials, while slower kinetics of HER for Co/NS-rGO can facilitate NO_3RR protonation.

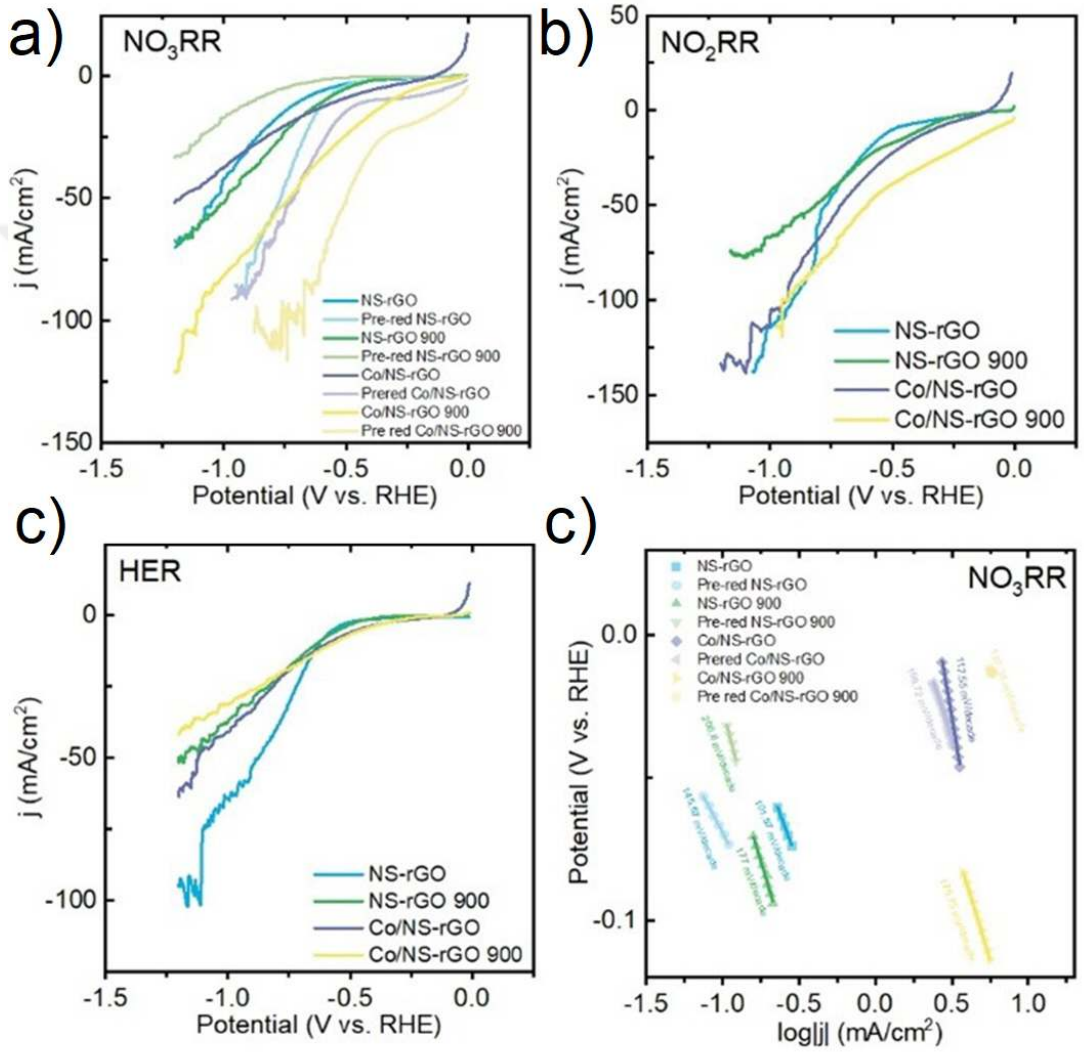

Figure 4-12: LSV Measurements. a) LSV for NO_3RR, b) LSV for NO_2RR, c) LSV for HER, d) Tafel Plot for NO_3RR

Sample	NO_3RR	TS	OP	NO_2RR	TS	OP	HER	TS	OP
NS-rGO		145.67	-0.67		161.19	-0.48		199.34	-0.54
Pre-red NS-rGO		101.87	-0.55						
NS-rGO 900		177	-0.53		115.73	-0.5		156.85	-0.53
Pre-red NS-rGO 900		206.8	-0.6						
Co/NS-rGO		317.87	-0.65		72.08	-0.27		563.75	-0.56
Pre-red Co/NS-rGO		169.72	-0.45						
Co/NS-rGO 900		175.75	-0.38		210.47	-0.52		145.03	-0.32
Pre-red Co/NS-rGO 900		107.38	-0.38						

Table 4-2: Tafel Slope (TS) Values (mV/decade) and Onset Potentials (OP) (V) of the samples for NO_3RR, NO_2RR, and HER

4.6 *Proposing Two Different NO_3RR Mechanisms Through Tafel Analysis and XAS*

When Tafel slope values, d-orbital occupancy, and spin state analysis from XAS are considered, one can propose two different mechanisms for Co/NS-rGO and Co/NS-rGO 900. It is observed that high d-orbital occupancy of Co/NS-rGO will repulse incoming NO_3^- molecules, and the HS state of Co/NS-rGO will induce weak Co-O bonds and will make the NO_3^- adsorption very challenging for the catalyst while ensuring better protonation properties which is in excellent agreement with Tafel analysis. On the other hand, low d-orbital occupancy and LS state of Co/NS-rGO 900 will allow better NO_3^- adsorption, and the catalyst will suffer from low protonation capabilities. Also, the faster kinetics of HER for Co/NS-rGO 900 shows the difficulty of protonating the sample from the Tafel analysis perspective.

4.7 *NH_3 Production Performance Tests Using Constant CA*

The high NO_2 yield rate and F.E. values for NS-rGO are shown by adding inductance to equivalent circuit modeling of Nyquist plots and the emergence of a new peak for inductance in DRT models and an inductive loop at EIS measurements NO_3RR after pre-reduction (Fig. 4-16) and NO_2RR[109], [158], [277], [278], [279], [280]. Fig. 4-13e shows that the electrolyte impedance (Z_e) is high for NS-rGO for NO_3RR without pre-reduction and charge transfer resistance (R_{ct}) (Fig. 4-14e) is high after pre-reduction,

which allows us to signify the inability of NS-rGO for NO_3 activation and adsorption for the former and NO_3-to-NH_3 e^- transfer for the latter which is in line with TS analysis. The fact that Z_e values are not very high for NO_2RR can show the NO_2 activation and adsorption ability of NS-rGO and R_{ct} values being comparably low (Fig. 4-14e) can be related to the comparably high NH_3 F.E. at more positive potentials. The decline in $F.E._{NH3}$ for NO_2RR in more negative potentials may be due to the relaxation of adsorbed NO_2 species shown by the emergence of the inductive loop (Fig. 4-16) at more negative potentials.

NO_3RR experiments for NS-rGO (Fig. 4-15 a, c) show that NH_3 production starts at -0.5 V and -0.6 V for NO_3RR and Pre-red NO_3RR, respectively, which is at the subsequent potential to the formation of the semicircle in EIS analysis (Fig. 4-16) and compliance with LSV onset potentials (Fig. 4-12a) for these samples. NS-rGO has the highest NO_2 yield rate and the lowest NH_3 yield rate at more negative potentials for all experiments. Also, pre-reduction facilitates NO_2 yield significantly while causing an inductive loop (Fig. 4-16), possibly due to the desorption of NO_2. Furthermore, the highest $F.E._{NH3}$ of NS-rGO is observed at -0.5 V for NO_3RR after pre-reduction, and $F.E._{NH3}$ is decreased significantly at more negative potentials. Even though pre-reduction enables the adsorption and activation of NO_3, high R_{ct} (Fig. 4-14b) at lower potentials shows the inability of NS-rGO to perform NO_3 to NH_3 e^- transfer. The fact that the higher frequency peak to low-frequency peak ratio is increasing for NS-rGO with increasing potential observed in the DRT model (Fig. 4-16) further enables us to claim that the reaction becomes kinetically limited after -0.6 V for NO_3RR with or without pre-reduction. This finding agrees with NS-rGO having the lowest NO_3RR and pre-red NO_3RR Tafel slope values. However, low NH_3 F.E. and yield rate for NO_3RR allow us to claim that the reaction is 1 e^- reduction from NO_3 to NO_2 rather than 8 e^- transfer for NO_3 to NH_3 electroreduction.

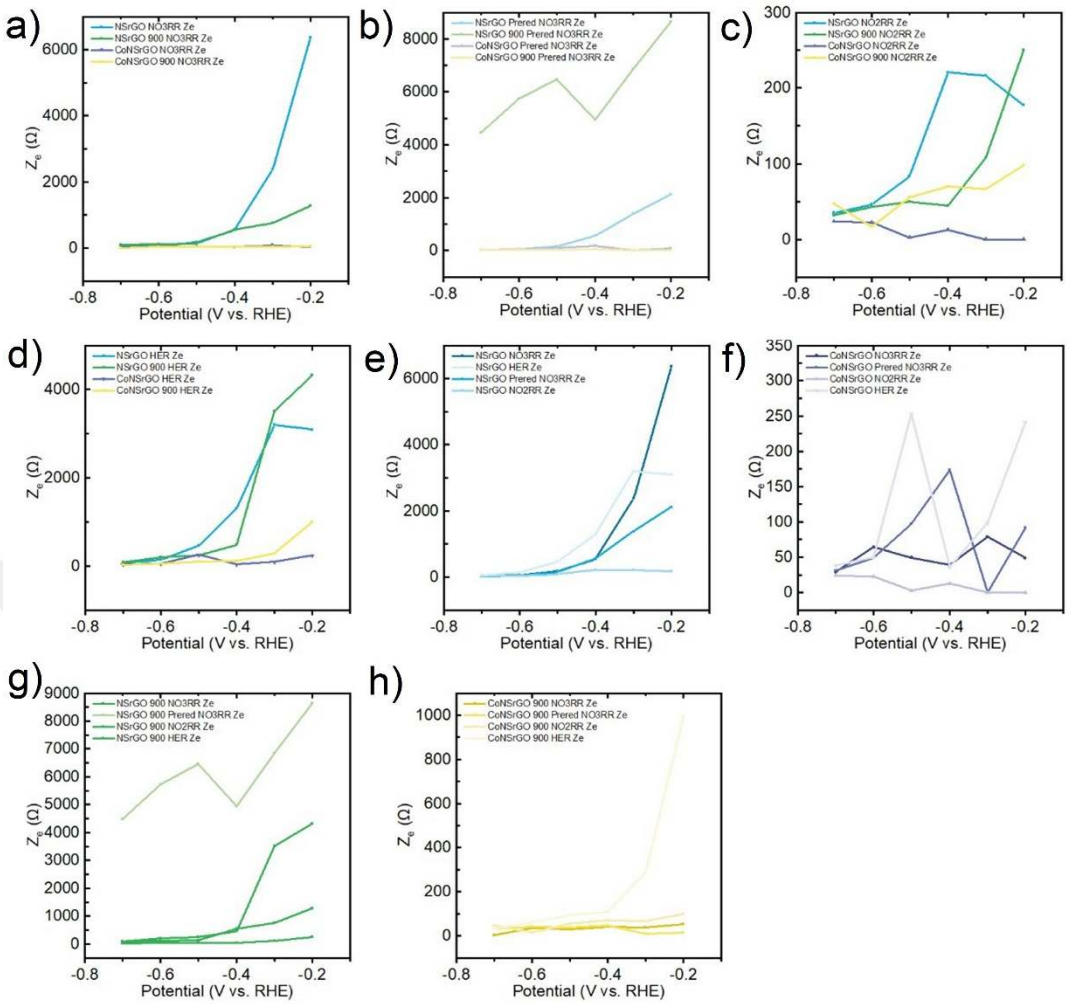

Figure 4-13: Electrolyte impedances (Z_e) for a) NO_3RR, b) Pre-red NO_3RR, c) NO_2RR, d) HER, e) NS-rGO, f) NS-rGO 900, g) Co/NS-rGO, h) Co/NS-rGO 900

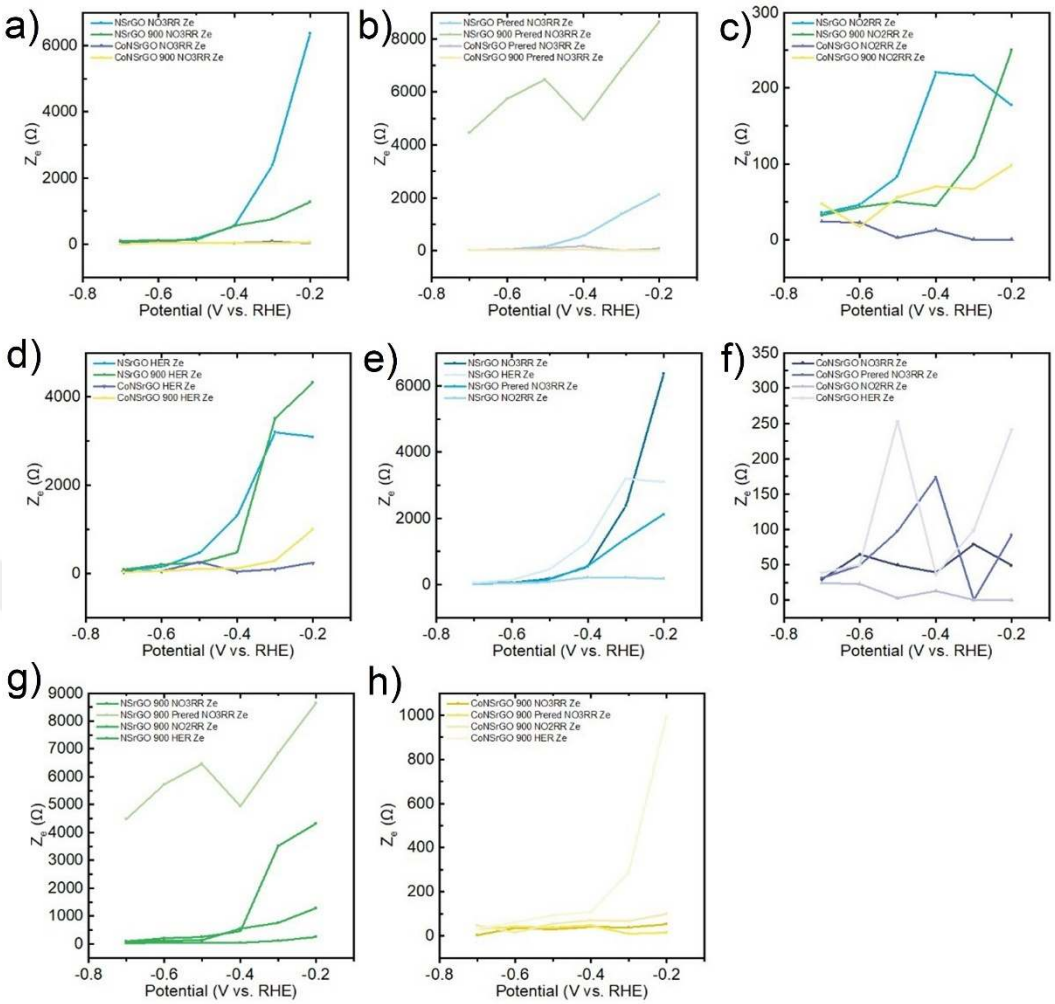

***Figure 4-14**:* Charge Transfer Resistances (R_{ct}) for a) NO_3RR, b) Pre-red NO_3RR, c) NO_2RR, d) HER, e) NS-rGO, f) NS-rGO 900, g) Co/NS-rGO, h) Co/NS-rGO 900

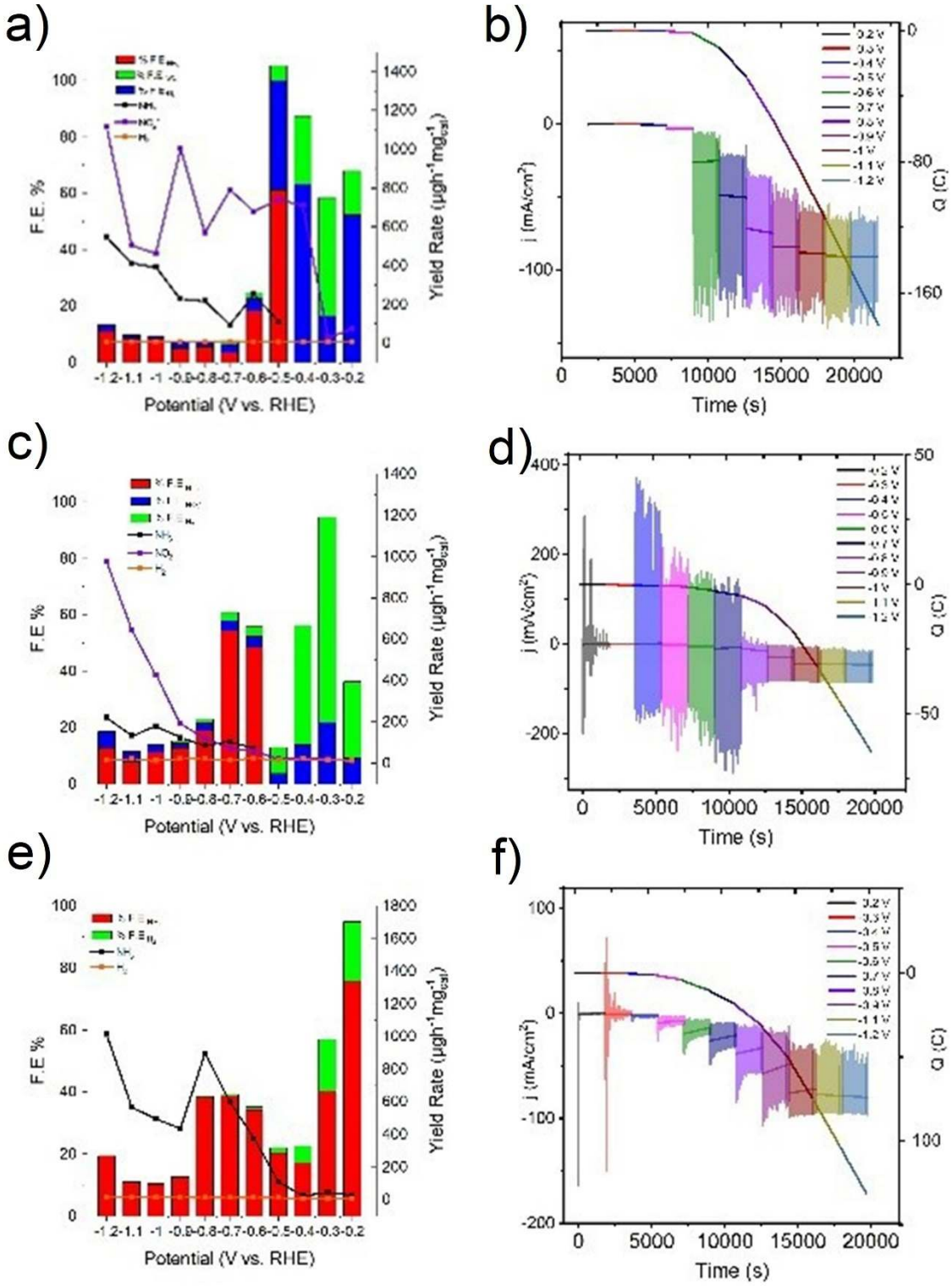

Figure 4-15: Nitrate to ammonia electrosynthesis activity of NS-rGO. a) NO_2^-, NH_3, H_2 F.E., and Y.R. of NS-rGO after pre-reduction at -1.5 V in 0.1 M KOH + 0.1 M KNO_3. b) j and q values for NS-rGO NO_3RR after pre-reduction at -1.5 V. c) NO_2^-, NH_3, H_2 F.E. and Y.R. of NS-rGO in 0.1 M KOH + 0.1 M KNO_3 d) j and q values for NS-rGO NO_3RR e) NO_2^-, NH_3, H_2 F.E. and Y.R. of NS-rGO in 0.1 M KOH + 0.1 M KNO_2 f) j and q values for NS-rGO NO_2RR

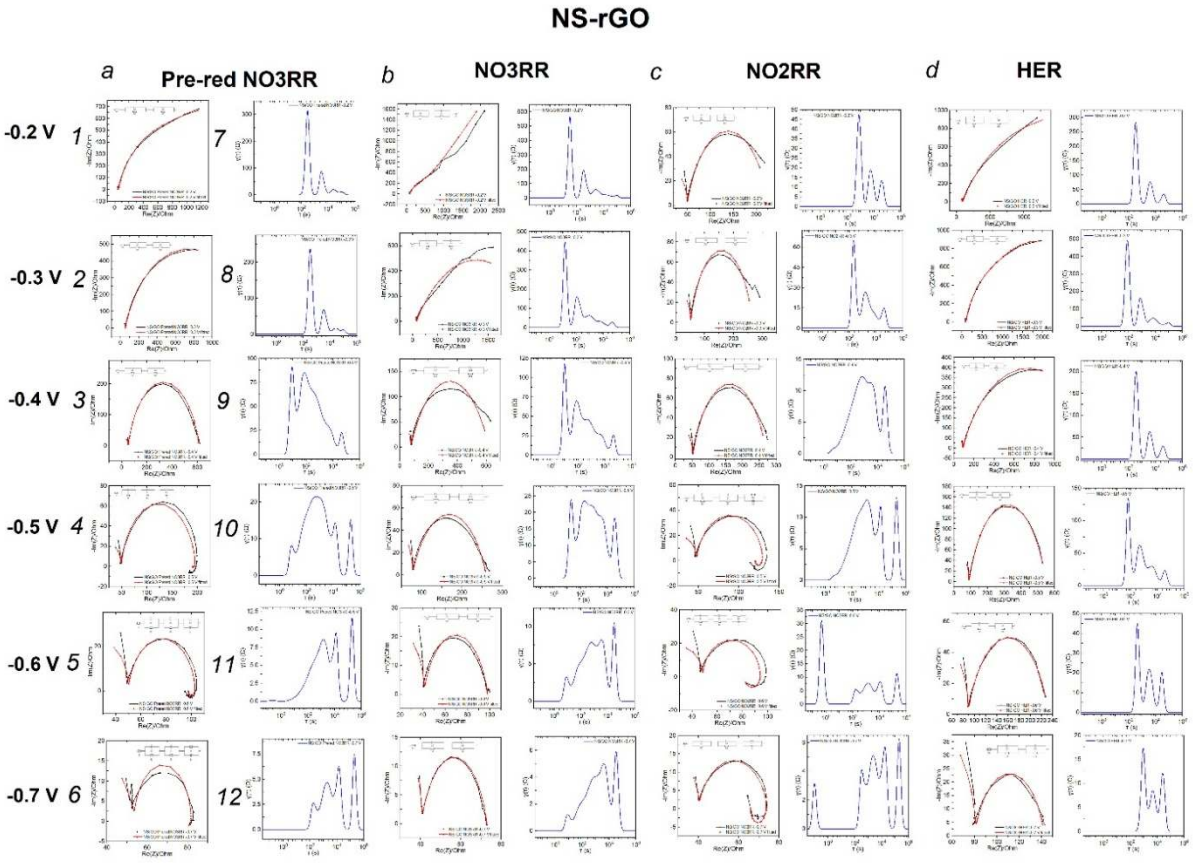

Figure 4-16: NS-rGO EIS and DRT Models

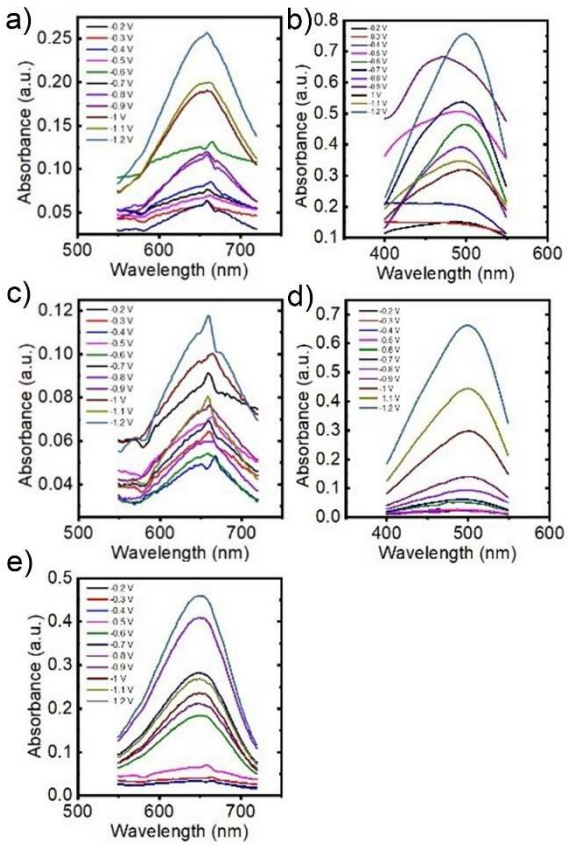

Figure 4-17: UV-vis spectroscopy results after NO_3RR and NO_2RR experiments. a) NH_3 quantification using the Indophenol Blue Method for NS-rGO NO_3RR after pre-reduction at -1.5 V. b) NO_2 quantification using the Griess Test for NS-rGO after pre-reduction at -1.5 V. c) NH_3 quantification using the Indophenol Blue Method for NS-rGO NO_3RR without pre-reduction at -1.5 V. d) NO_2 quantification using the Griess Test for NS-rGO without pre-reduction at -1.5 V. e) NH_3 quantification using the Indophenol Blue Method for NS-rGO NO_2RR.

High TS values for NO_3RR and NO_2RR indicate that NS-rGO 900 follows an adsorption-limited mechanism (Table 4-2). Surprisingly, the activity of the NS-rGO 900 catalyst is diminished after pre-reduction, where an increase in both overpotential and NO_3RR TS is observed (Fig. 4-12a). Also, HER TS values indicate faster kinetics for pyrolyzed samples as of NS-rGO 900 having 199.34 mV/decade. Superior HER kinetics are also observed in high H_2 yield in NH_3 activity measurements (Fig. 4-18). The highest Z_e (Fig. 4-13f) values for NS-rGO, among other samples, especially after pre-reduction, signify the mass-transfer limited NO_3RR activity of the catalyst. Also, the highest R_{ct} values (Fig. 4-14f) show that the subsequent charge transfer has inferior properties, which explains the low NH_3 activity of the catalyst suppressed by superior HER. High peak intensity of low frequencies in the DRT Model and the formation of semicircles in later potentials also emphasize the catalyst's inferior NO_3RR and NO_2RR activity (Fig. 7).

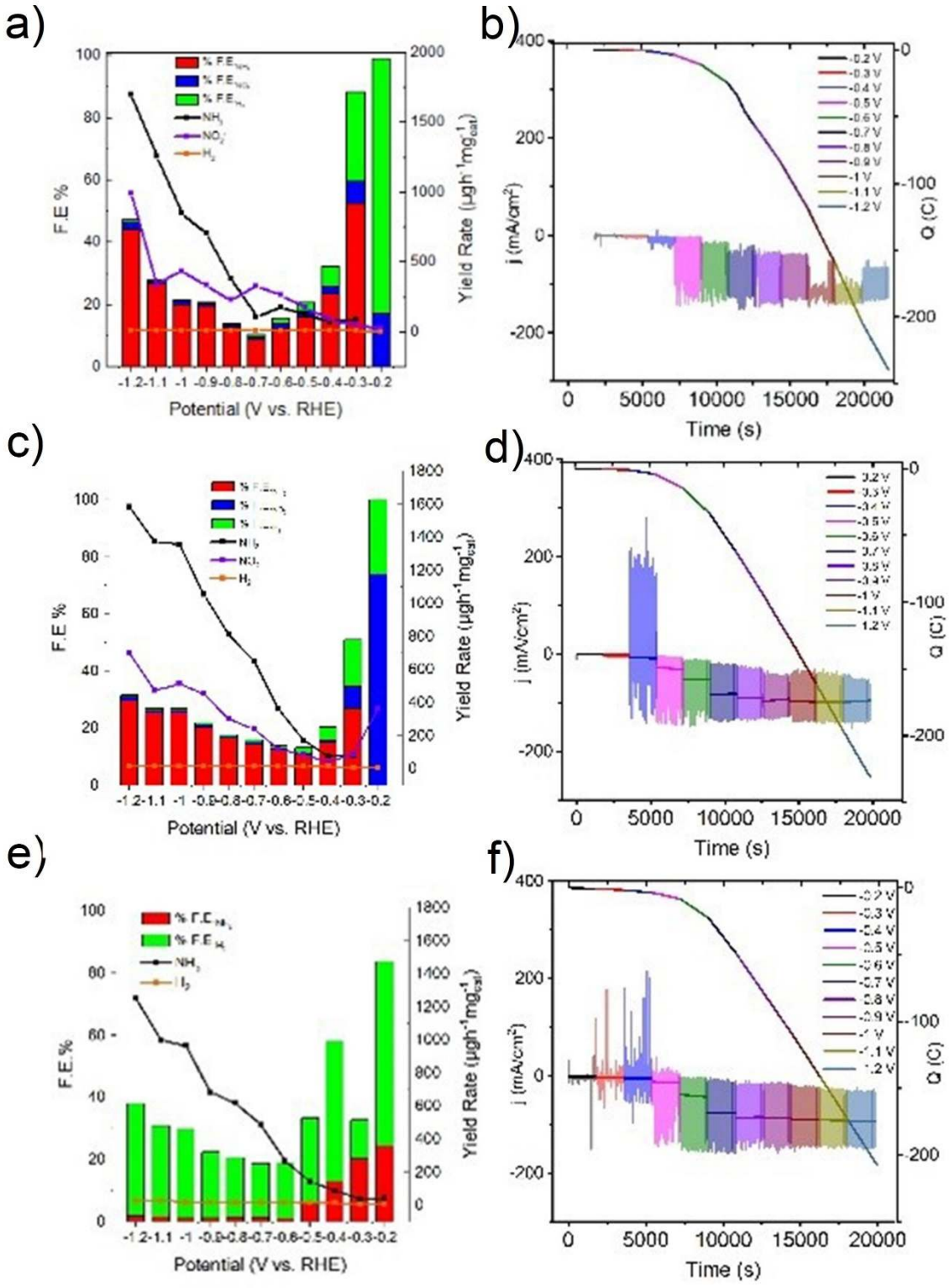

Figure 4-18: Nitrate to ammonia electrosynthesis activity of NS-rGO 900. a) NO_2^-, NH_3, H_2 F.E., and Y.R. of NS-rGO 900 after pre-reduction at -1.5 V in 0.1 M KOH + 0.1 M KNO_3. b) j and q values for NS-rGO 900 NO_3RR after pre-reduction at -1.5 V. c) NO_2^-, NH_3, H_2 F.E. and Y.R. of NS-rGO 900 in 0.1 M KOH + 0.1 M KNO_3 d) j and q values for NS-rGO 900 NO_3RR e) NO_2^-, NH_3, H_2 F.E. and Y.R. of NS-rGO 900 in 0.1 M KOH + 0.1 M KNO_2 f) j and q values for NS-rGO 900 NO_2RR

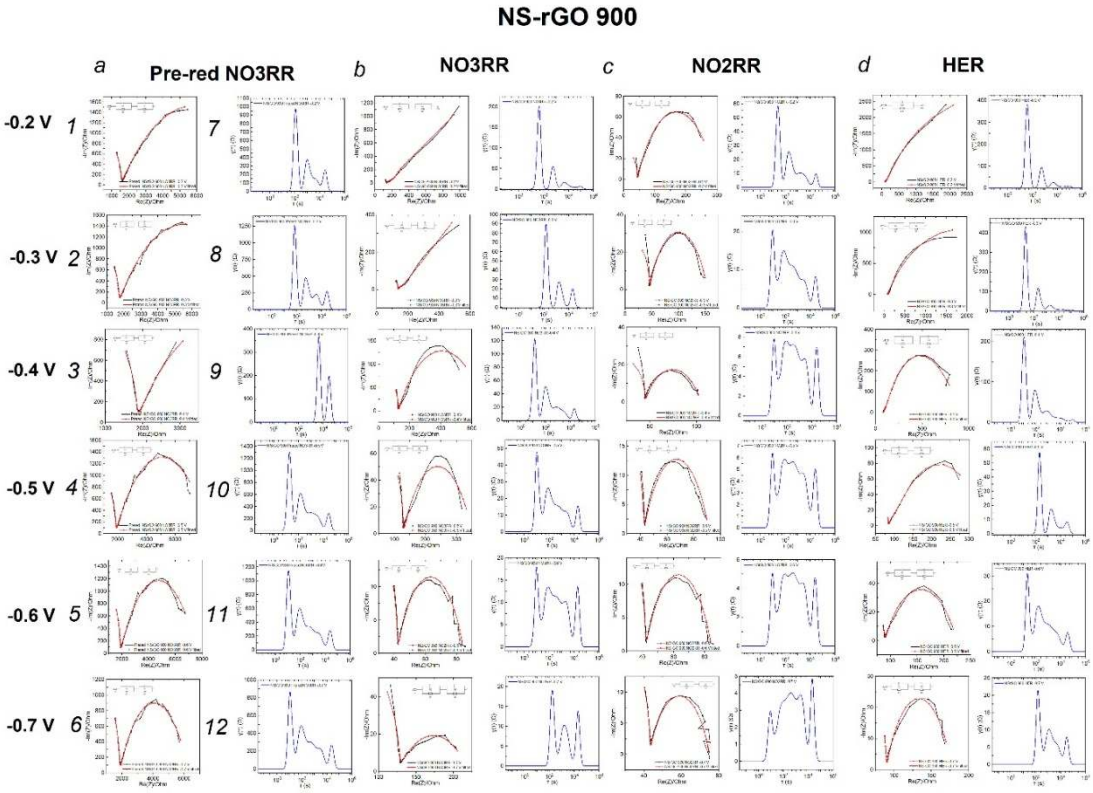

Figure 4-19: DRT and EIS analysis for NS-rGO 900

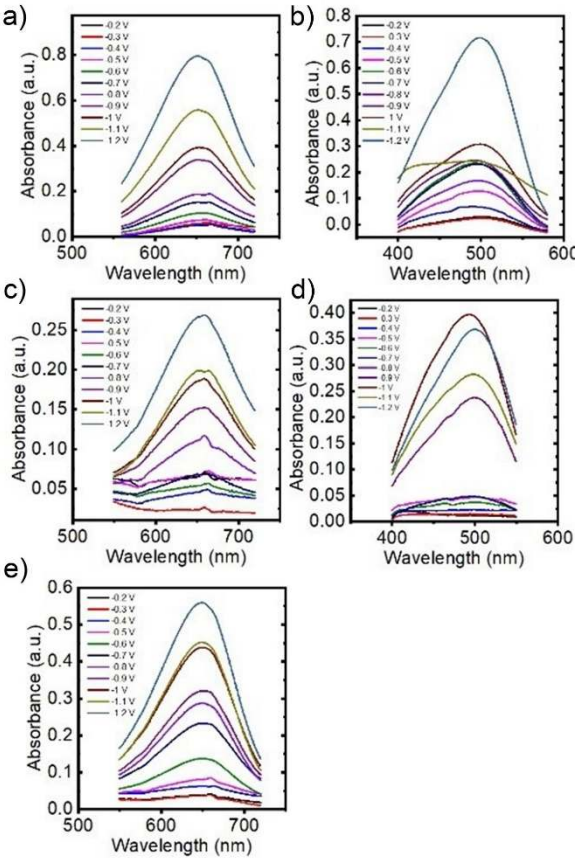

Figure 4-20: UV-vis spectroscopy results after NO_3RR and NO_2RR experiments. a) NH_3 quantification using the Indophenol Blue Method for NS-rGO 900 NO_3RR after pre-reduction at -1.5 V. b) NO_2 quantification using the Griess Test for NS-rGO 900 after pre-reduction at -1.5 V. c) NH_3 quantification using the Indophenol Blue Method for NS-rGO 900 NO_3RR without pre-reduction at -1.5 V. d) NO_2 quantification using the Griess Test for NS-rGO 900 without pre-reduction at -1.5 V. e) NH_3 quantification using the Indophenol Blue Method for NS-rGO 900 NO_2RR.

Even though NO_3RR TS is significantly lowered after the pre-reduction from 317.87 to 169.72 mV/decade, high TS values for Co/NS-rGO indicate a mass-transport-limited NO_3RR mechanism (Table 4-2). Furthermore, the highest HER TS of 563.75 mV/decade is achieved for Co/NS-rGO, indicating suppressed HER activity. This agrees with the low H_2 yield obtained from NH_3 activity measurements and XAS data, which shows that Co/NS-rGO facilitates protonation better. It is observed that the pre-reduction lowers the potential for NH_3 F.E. maxima from -0.9 V to -0.4 V (Fig. 4-21a). Also, the highest $F.E._{NH3}$ for Co/NS-rGO in the pre-reduced case is achieved at NO_3RR onset potential, while without pre-reduction, on top of a -200 mV increase in overpotential, the catalyst does not show its NH_3 F.E. onset potential, possibly due to the absence of a well-defined kinetic, mixed-kinetic and mass-transfer limited region (Fig. 4-12a). Since the NO_3RR for Co/NS-rGO is limited by the NO_3 adsorption, lower Z_e values (Fig. 4-13g) for Co/NS-rGO than NS-rGO can explain the increase in NH_3 production activity with Co incorporation.

As TS results suggest, the high peak intensity ratio between high-frequency and low-frequency peaks in the DRT model indicates that NO_3RR and HER reactions signify the adsorption-driven mechanism of Co/NS-rGO (Fig. 4-22). It is reported that high-frequency inductance behavior is associated with the relaxation of surface coverages or species desorption[158]. The same phenomenon is observed for pre-red NO_3RR starting from -0.5 V, increasing inductive loop sizes in EIS, and the emergence of a new peak in the DRT model. After pre-reduction, a 2-fold increase in NO_2 yield rate and higher NO_2 F.E. values allows us to claim the possibility of NO_2 being the desorbed species. Pre-reduction lowered the potential for forming the semicircle associated with the NO_3RR charge transfer. EIS and DRT behavior after pre-reduction can point out a change in the NO_3RR mechanism. The increase in NH_3 yield after pre-reduction may be explained by the more facile reduction of desorbed NO_2 at the next more negative potential in a mass-transfer-limited fashion owing to superior NO_2RR properties of Co/NS-rGO.

We see an exceptional NO_2RR activity for Co/NS-rGO in NH_3 yield and F.E values (Fig. 4-21). Similar superior NO_2RR activity of Co catalysts is reported in the literature, too. Very high NH_3 F.E. values are observed for Co/NS-rGO throughout the studied potential range, and we see a near 100% F.E. at more negative potentials owing to the superior protonation ability of Co/NS-rGO. Surprisingly, the low NO_2RR TS of Co/NS-rGO 72.08 mV/decade shows that neither NO_2 adsorption nor charge transfer processes are RDS but a chemical step. Tafel analysis signifies the facile adsorption and e^- transfer processes for Co/NS-rGO. Furthermore, a significantly high HER TS of 563.75 mV/decade aligns with a low H_2 yield rate and F.E. observed for NO_3RR and NO_2RR experiments. This finding shows that HER cannot suppress NO_3RR and NO_2RR, and protonation is highly facilitated for the proposed mechanism. For NO_2RR, the inductive behavior starts at lower frequencies, which can be attributed to electrical connection disturbances or EDL interactions[281]. Because low-frequency behavior is only observed for the NO_2RR experiment of Co/NS-rGO, we claim that the behavior is due to EDL contributions induced by NO_2^-. Furthermore, the affinity of NO_2^- species to interact with Co/NS-rGO EDL can indicate the facile movement of NO_2 along EDL, supporting the easier NO_2 desorption on EDL.

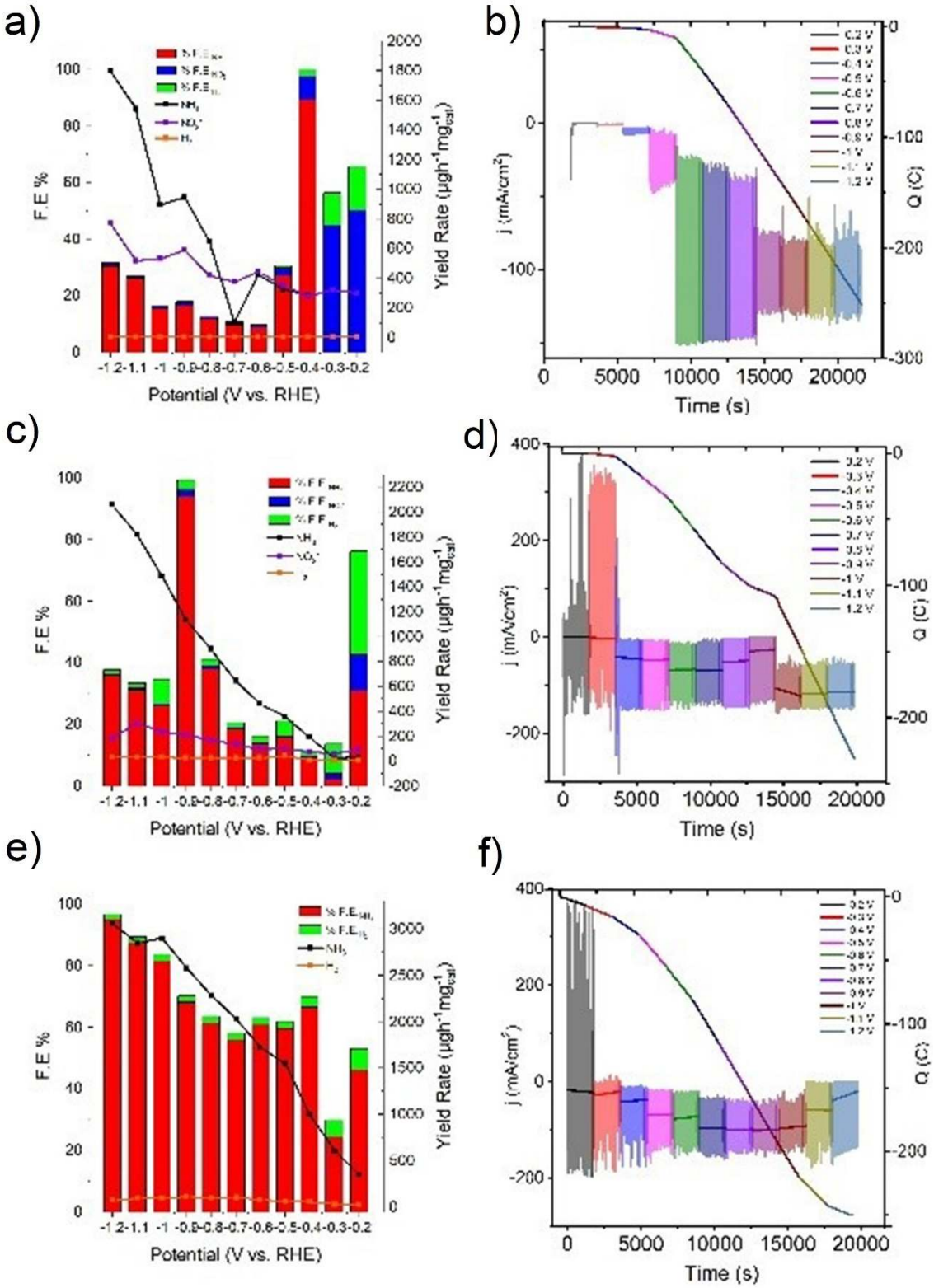

Figure 4-21: Nitrate to ammonia electrosynthesis activity of Co/NS-rGO. a) NO_2^-, NH_3, H_2 F.E., and Y.R. of Co/NS-rGO after pre-reduction at -1.5 V in 0.1 M KOH + 0.1 M KNO_3. b) j and q values for Co/NS-rGO NO_3RR after pre-reduction at -1.5 V. c) NO_2^-, NH_3, H_2 F.E. and Y.R. of Co/NS-rGO in 0.1 M KOH + 0.1 M KNO_3 d) j and q values for Co/NS-rGO NO_3RR e) NO_2^-, NH_3, H_2 F.E. and Y.R. of Co/NS-rGO in 0.1 M KOH + 0.1 M KNO_2 f) j and q values for Co/NS-rGO NO_2RR

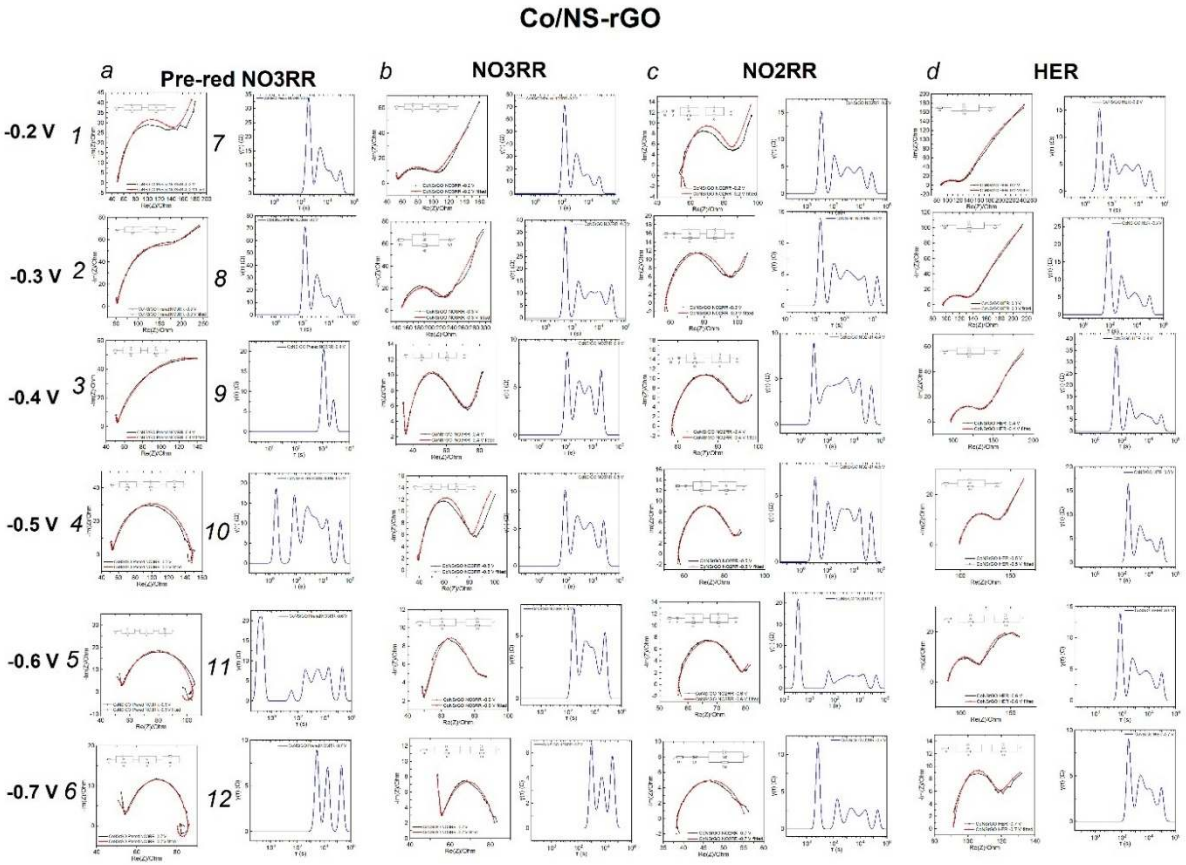

Figure 4-22: Potential dependent EIS and DRT analysis for Co/NS-rGO

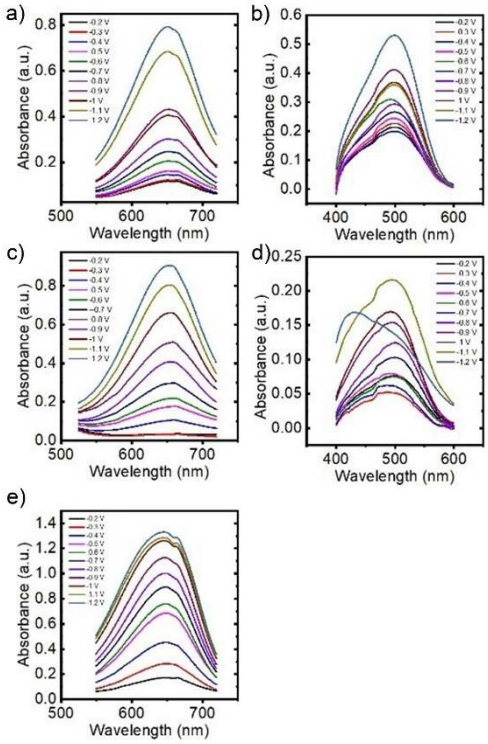

Figure 4-23: UV-vis spectroscopy results after NO_3RR and NO_2RR experiments. a) NH_3 quantification using the Indophenol Blue Method for Co/NS-rGO NO_3RR after pre-reduction at -1.5 V. b) NO_2 quantification using the Griess Test for Co/NS-rGO after pre-reduction at -1.5 V. c) NH_3 quantification using the Indophenol Blue Method for Co/NS-rGO NO_3RR without pre-reduction at -1.5 V. d) NO_2 quantification using the Griess Test for Co/NS-rGO without pre-reduction at -1.5 V. e) NH_3 quantification using the Indophenol Blue Method for Co/NS-rGO NO_2RR.

TS values of Co/NS-rGO 900 indicate that after pre-reduction, the reaction mechanism becomes NO_3-NO_2 $1e^-$ transfer from being adsorption limited (Table 4-2). Also, high NO_2RR TS and high overpotential indicate a NO_2 adsorption-limited mechanism and explain the catalyst's inferior NO_2RR activity (Fig. 4-12b). Furthermore, low HER TS indicates faster kinetics, which agrees with the high H_2 yield in NO_3RR experiments (Fig. 4-24). Also, TS findings align with the proposed mechanism inspired by XAS analysis where facile NO_3 adsorption properties for pre-red NO_3RR and low protonation properties due to fast HER kinetics. On the other hand, low Z_e (Fig. 4-13h) and R_{ct} (Fig. 4-14h) values for NO_3RR and high values for corresponding indicators for NO_2RR support our claim for the Co/NS-rGO 900 activity. NH_3 electrosynthesis activity measurements (Fig. 4-24) show the high NH_3 F.E. and yield rates, the positive effect of pre-reduction in lowering the potential for NH_3 production maxima, high H_2 yield, and inferior NO_2RR activity of the catalyst. EIS analysis (Fig. 4-25) shows a first bump in both NO_3RR and NO_2RR experiments, indicating the emergence of a semicircle for the former and a capacitive behavior for the latter. Different from other samples, instead of two peaks, adsorption and charge transfer processes are carried out in nearly the same semicircle with lower time constants. This finding shows the facile NO_3RR adsorption properties and charge-transfer limitation of the catalyst where NO_3-NO_2 e^- transfer is carried out easier, demonstrated by the formation of a semicircle butO_2-NO e^- transfer being not favored due to the absence of a semicircle. DRT model supports this claim by demonstrating higher frequency peaks and singular peaks in later potentials.

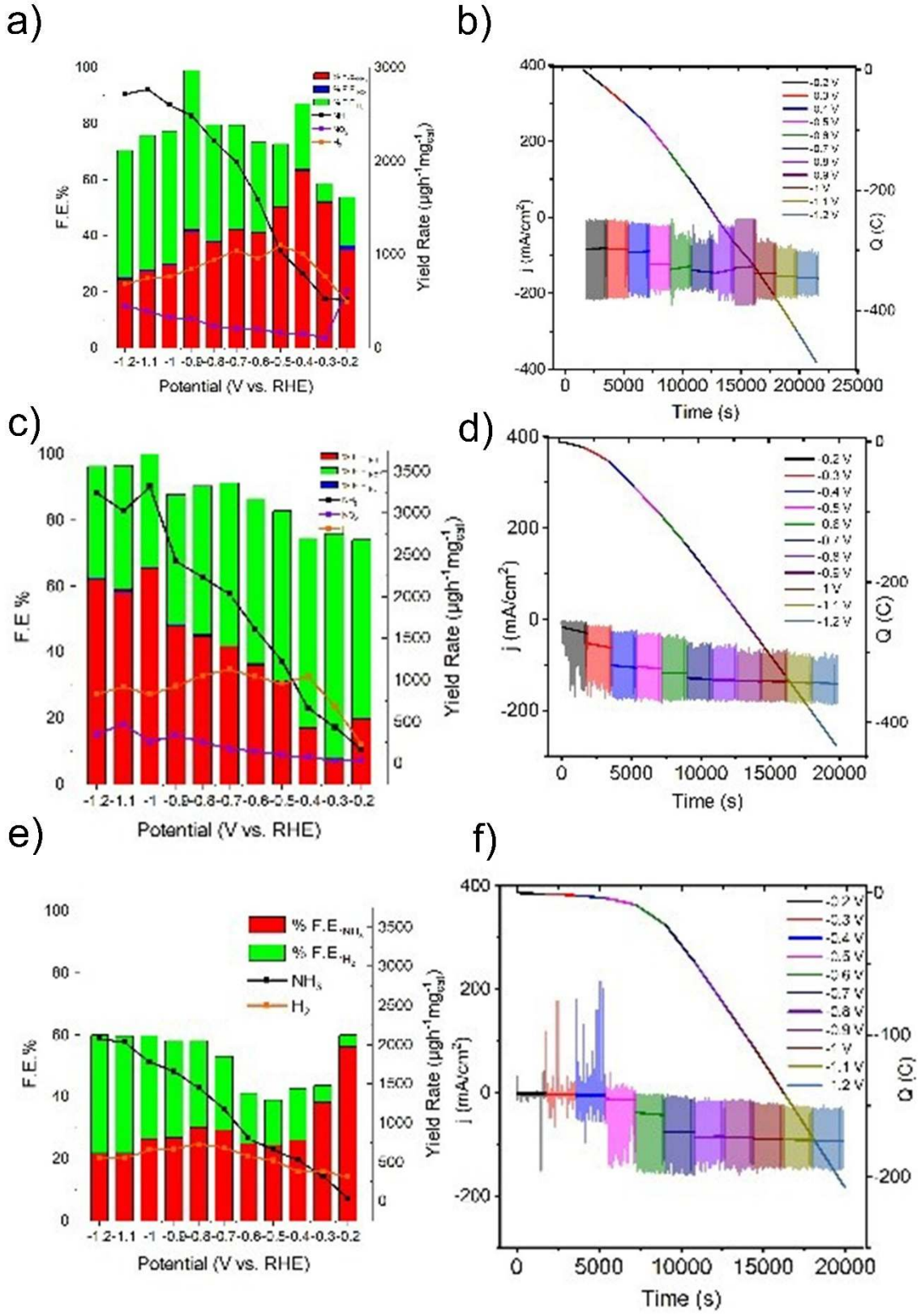

Figure 4-24: Nitrate to ammonia electrosynthesis activity of Co/NS-rGO 900. a) NO_2^-, NH_3, H_2 F.E., and Y.R. of Co/NS-rGO 900 after pre-reduction at -1.5 V in 0.1 M KOH + 0.1 M KNO_3. b) j and q values for Co/NS-rGO 900 NO_3RR after pre-reduction at -1.5 V. c) NO_2^-, NH_3, H_2 F.E. and Y.R. of Co/NS-rGO 900 in 0.1 M KOH + 0.1 M KNO_3 d) j and q values for

Co/NS-rGO 900 NO_3RR e) NO_2^-, NH_3, H_2 F.E. and Y.R. of Co/NS-rGO 900 in 0.1 M KOH + 0.1 M KNO_2 f) j and q values for Co/NS-rGO 900 NO_2RR

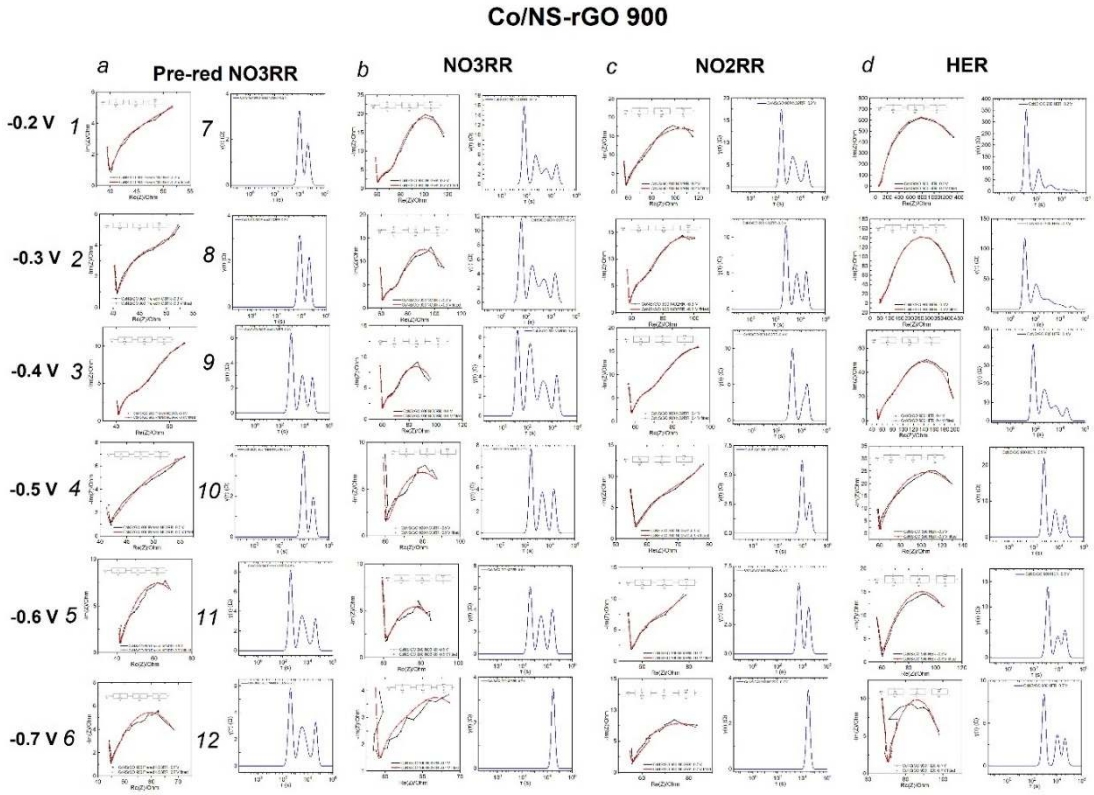

Figure 4-25: DRT and EIS analysis for Co/NS-rGO 900

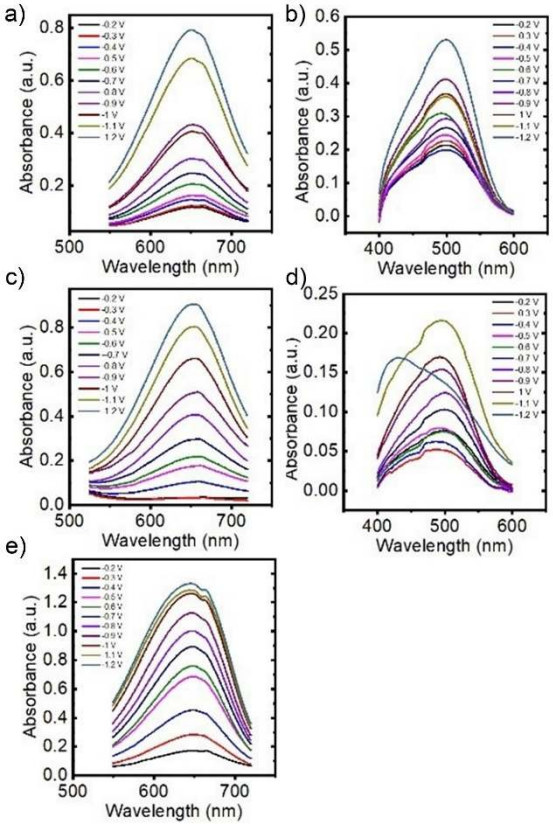

Figure 4-26: UV-vis spectroscopy results after NO_3RR and NO_2RR experiments. a) NH_3 quantification using the Indophenol Blue Method for Co/NS-rGO 900 NO_3RR after pre-reduction at -1.5 V. b) NO_2 quantification using the Griess Test for Co/NS-rGO 900 after pre-reduction at -1.5 V. c) NH_3 quantification using the Indophenol Blue Method for Co/NS-rGO 900 NO_3RR without pre-reduction at -1.5 V. d) NO_2 quantification using the Griess Test for Co/NS-rGO 900 without pre-reduction at -1.5 V. e) NH_3 quantification using the Indophenol Blue Method for Co/NS-rGO 900 NO_2RR.

4.8 *NH_3 Production Performance Tests Using Pulsed CA*

Considering the high NH_3 yield rates and F.E.s of Co/NS-rGO for NO_2RR, which is also reported in the literature, the observed mass transport limitations, to further investigate the actual behavior of adsorption limitations and better protonation properties of proposed mechanism and presence of NO_2^- desorption, a pulse strategy is proposed in both mass transfer limited and charge transfer dominated potentials of -0.4 V and -0.9 V consecutively. Also, the pulse method is utilized to examine the effect of more positive or negative potentials than the studied potential on NO_3RR activity through changes in the NO_3 concentration on the electrode. Furthermore, as suggested in other studies, the presence of a tandem NO_3RR electrolysis is investigated through a pulsed strategy owing to the desorption of NO_2^- species, surprisingly low Tafel Slope for Co/NS-rGO indicating a chemical step, and uniquely high NO_2^- to NH_3 conversion activity of Co/NS-rGO. Also, the behavior of non-metal and pyrolyzed metal-loaded catalysts is investigated to examine the mechanism of different catalysts.

Pulsed NO_3RR for NS-rGO (Fig. 4-27) is carried out to drive the reaction into becoming more mass-transfer limited by applying pulses at -0.4 V and the studied potential for 2 s each. In pre-reduced NO_3RR, NH_3 production starts at a later potential, possibly due to the more intensified mass-transport limitations or less NO_3 concentration on the electrode. Furthermore, the NO_2 F.E. nearly becomes zero when NH_3 F.E. increases owing to the consecutive reduction of desorbed NO_2 species identified in EIS analysis for pre-reduced NO_3RR through pulsed reduction. For NO_3RR, overall NH_3 and NO_2 F.E. is increased while H_2 F.E. is diminished. NO_2RR activity measurements show that for pulsed measurements, $F.E._{NH3}$ increases at less negative potentials and decreases at more negative potentials due to mass-transfer properties being more dominant at more positive potentials.

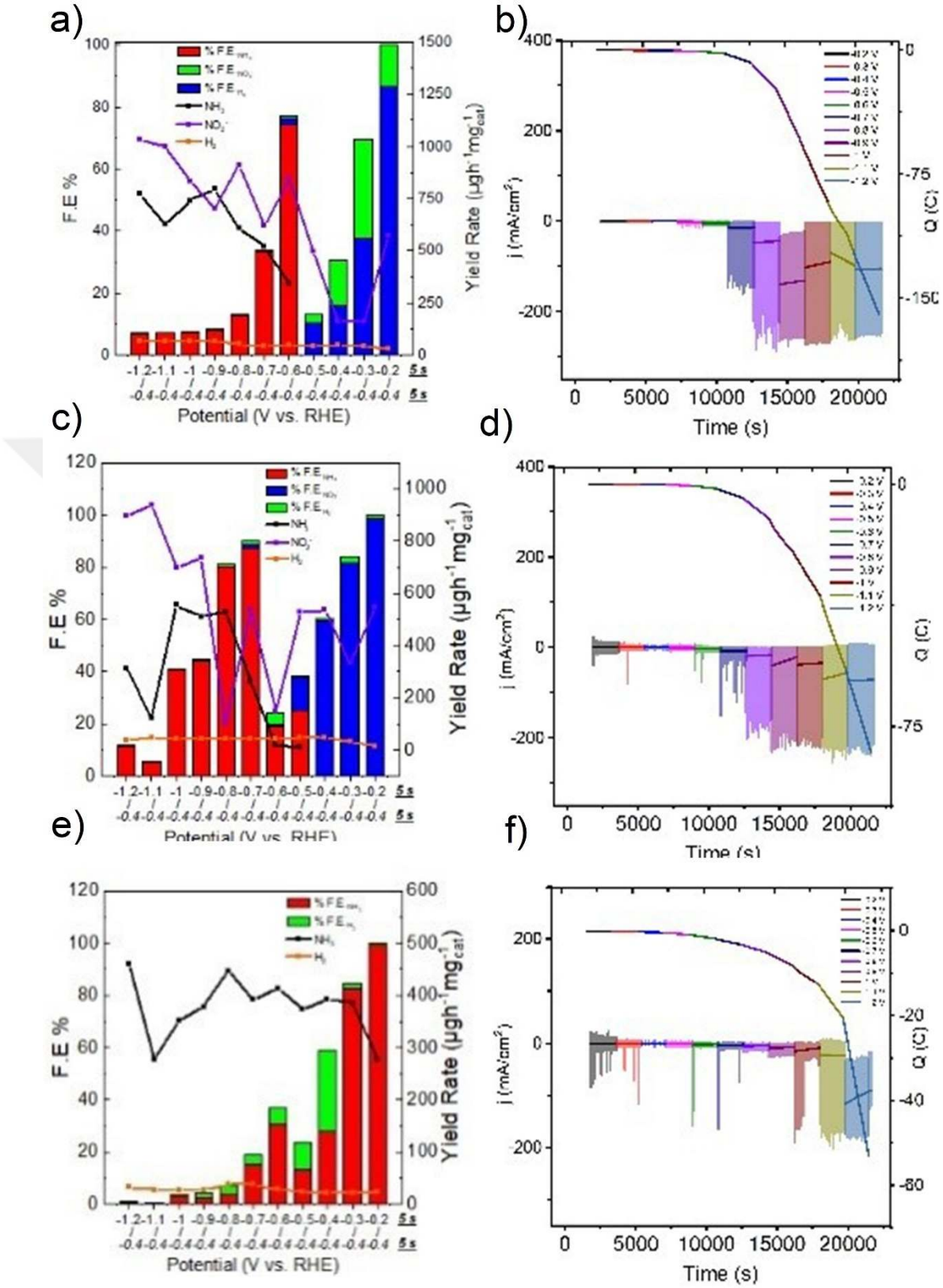

Figure 4-27: Pulsed Nitrate to ammonia electrosynthesis activity of NS-rGO for 2 s at constant electrolysis potentials and pulsed potential of -0.4 V. a) NO_2^-, NH_3, H_2 F.E., and Y.R. of NS-rGO after pre-reduction at -1.5 V in 0.1 M KOH + 0.1 M KNO_3. b) j and q values for NS-

rGO NO_3RR after pre-reduction at -1.5 V. c) NO_2^-, NH_3, H_2 F.E. and Y.R. of NS-rGO in 0.1 M KOH + 0.1 M KNO_3 d) j and q values for NS-rGO NO_3RR e) NO_2^-, NH_3, H_2 F.E. and Y.R. of NS-rGO in 0.1 M KOH + 0.1 M KNO_2 f) j and q values for NS-rGO NO_2RR

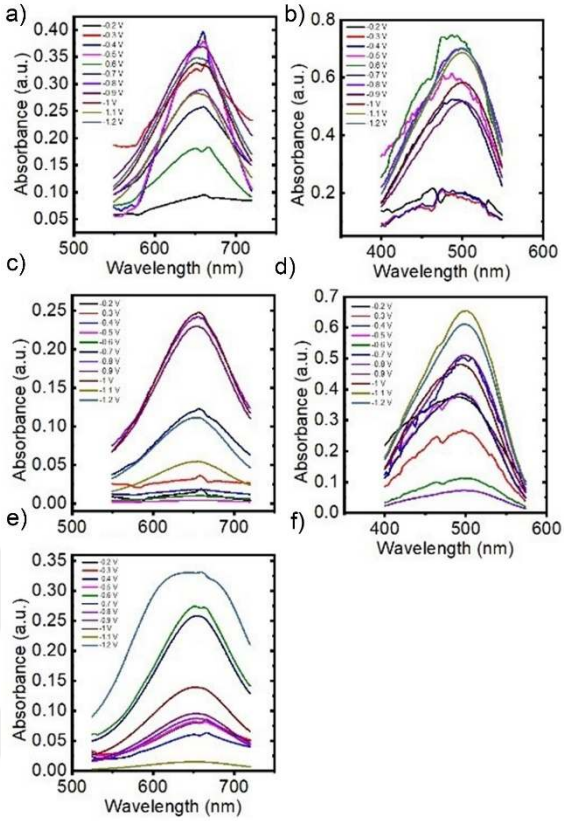

Figure 4-28: UV-vis spectroscopy results after pulsed NO_3RR and NO_2RR experiments at constant electrolysis potentials and pulsed potential of -0.4 V for 2 s. a) NH_3 quantification using the Indophenol Blue Method for NS-rGO NO_3RR after pre-reduction at -1.5 V. b) NO_2 quantification using the Griess Test for NS-rGO after pre-reduction at -1.5 V. c) NH_3 quantification using the Indophenol Blue Method for NS-rGO NO_3RR without pre-reduction at -1.5 V. d) NO_2 quantification using the Griess Test for NS-rGO without pre-reduction at -1.5 V. e) NH_3 quantification using the Indophenol Blue Method for NS-rGO NO_2RR.

Higher NH_3 F.E. values are obtained for pre-reduced Co/NS-rGO NO_3RR (Fig. 4-29) pulsed electroreduction experiments at -0.4 V, possibly due to the consecutive reduction of the desorbed NO_2 species. Furthermore, it is observed that at more negative potentials, $F.E._{NH3}$ values steadily increase owing to the preservation of the material's mass-transfer-limited properties and superior protonation assets. Also, for NO_3RR, $F.E._{NH3}$ is increased compared to constant CA measurements throughout the potential range except for the exceptionally high performance at -0.9 V NO_3RR of Co/NS-rGO. However, it is observed that the pulsed CA at -0.4 V for 2 s does not promote constant NO_2RR, possibly due to no adsorption limitations for NO_2RR.

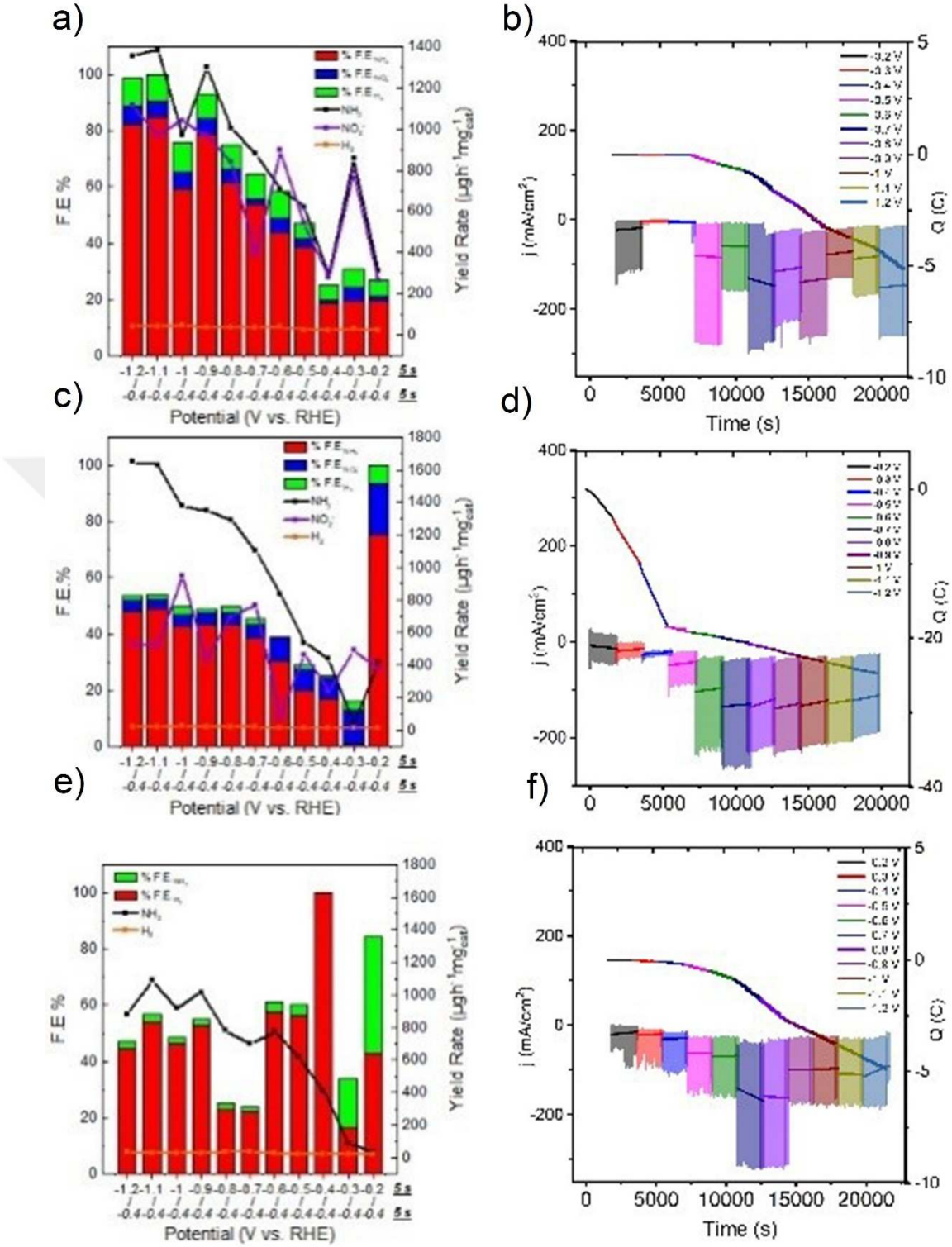

Figure 4-29: Pulsed Nitrate to ammonia electrosynthesis activity of Co/NS-rGO for 2 s at constant electrolysis potentials and pulsed potential of -0.4 V. a) NO_2^-, NH_3, H_2 F.E., and Y.R. of Co/NS-rGO after pre-reduction at -1.5 V in 0.1 M KOH + 0.1 M KNO_3. b) j and q values for Co/NS-rGO NO_3RR after pre-reduction at -1.5 V. c) NO_2^-, NH_3, H_2 F.E. and Y.R. of Co/NS-rGO in 0.1 M KOH + 0.1 M KNO_3 d) j and q values for Co/NS-rGO NO_3RR e) NO_2^-, NH_3, H_2 F.E. and Y.R. of Co/NS-rGO in 0.1 M KOH + 0.1 M KNO_2 f) j and q values for Co/NS-rGO NO_2RR

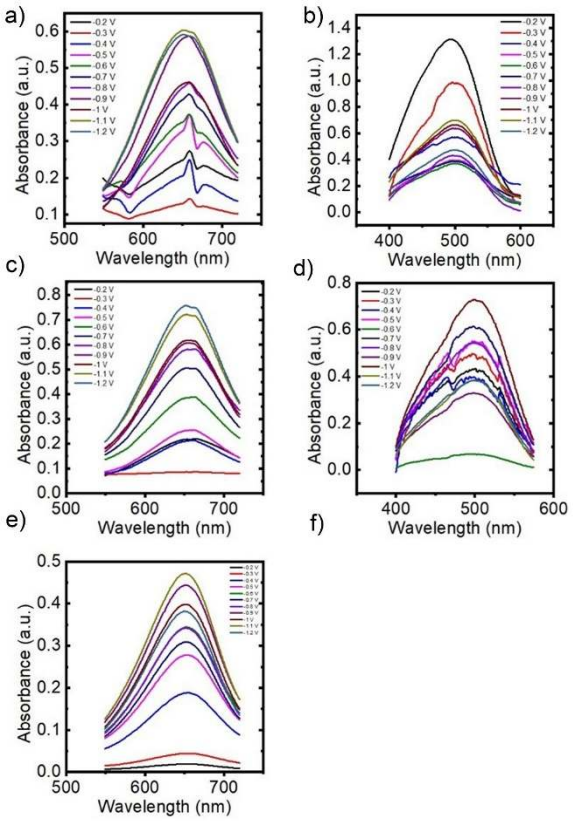

Figure 4-30: UV-vis spectroscopy results after pulsed NO_3RR and NO_2RR experiments at constant electrolysis potentials and pulsed potential of -0.4 V for 2 s. a) NH_3 quantification using the Indophenol Blue Method for Co/NS-rGO NO_3RR after pre-reduction at -1.5 V. b) NO_2 quantification using the Griess Test for Co/NS-rGO after pre-reduction at -1.5 V. c) NH_3 quantification using the Indophenol Blue Method for Co/NS-rGO NO_3RR without pre-reduction at -1.5 V. d) NO_2 quantification using the Griess Test for Co/NS-rGO without pre-reduction at -1.5 V. e) NH_3 quantification using the Indophenol Blue Method for Co/NS-rGO NO_2RR.

Even though NH_3 production starts at earlier potentials for pulsed electroreduction at -0.9 V, possibly owing to higher negative bias on the electrode, overall NH_3 F.E. is lower than the pulse at -0.4 V due to the superior catalytic properties of the material in mass-transfer-limited potentials. In the -0.9 V pulse, NO_3RR and NO_2RR for NS-rGO are heavily suppressed by HER, as shown by increasing H_2 yield rate and F.E. Interestingly, the highest NO_2 yield rate is achieved for NS-rGO at more negative potentials, possibly owing to increasing desorption at these potentials.

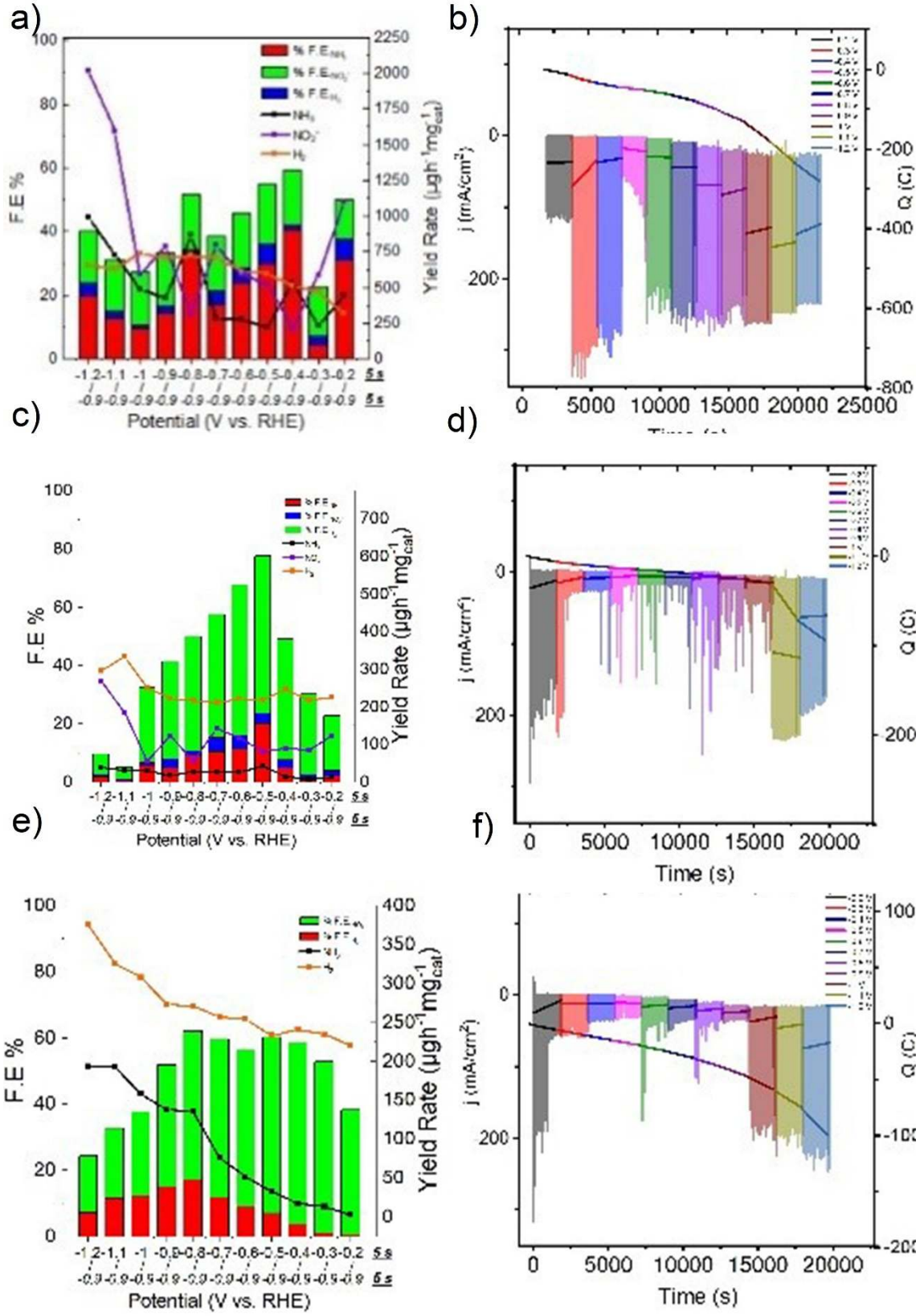

Figure 4-31: Pulsed Nitrate to ammonia electrosynthesis activity of NS-rGO for 2 s at constant electrolysis potentials and pulsed potential of -0.9 V. a) NO_2^-, NH_3, H_2 F.E., and Y.R. of NS-rGO after pre-reduction at -1.5 V in 0.1 M KOH + 0.1 M KNO_3. b) j and q values for NS-rGO NO_3RR after pre-reduction at -1.5 V. c) NO_2^-, NH_3, H_2 F.E. and Y.R. of NS-rGO in 0.1 M

KOH + 0.1 M KNO_3 d) j and q values for NS-rGO NO_3RR e) NO_2^-, NH_3, H_2 F.E. and Y.R. of NS-rGO in 0.1 M KOH + 0.1 M KNO_2 f) j and q values for NS-rGO NO_2RR

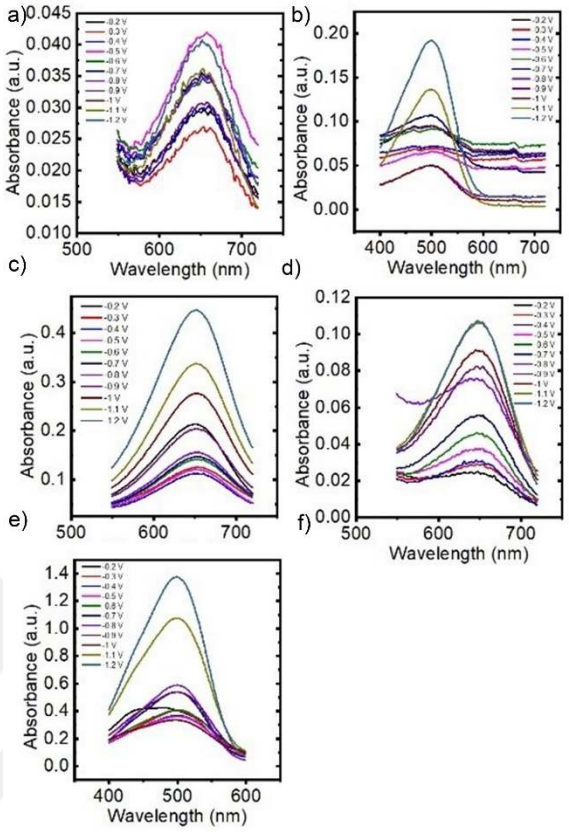

Figure 4-32: UV-vis spectroscopy results after pulsed NO_3RR and NO_2RR experiments at constant electrolysis potentials and pulsed potential of -0.9 V for 2 s. a) NH_3 quantification using the Indophenol Blue Method for NS-rGO NO_3RR after pre-reduction at -1.5 V. b) NO_2 quantification using the Griess Test for NS-rGO after pre-reduction at -1.5 V. c) NH_3 quantification using the Indophenol Blue Method for NS-rGO NO_3RR without pre-reduction at -1.5 V. d) NO_2 quantification using the Griess Test for NS-rGO without pre-reduction at -1.5 V. e) NH_3 quantification using the Indophenol Blue Method for NS-rGO NO_2RR.

Similar phenomena in NS-rGO of increasing H_2 yield rate and F.E. are also observed for Co/NS-rGO pulsed experiments at -0.9 V (Fig. 4-33). For Pre-red NO_3RR, even though there is a minor decrease in NH_3 F.E. compared to pulse at -0.4 V, the NH_3 yield rate is tripled compared to constant electrolysis and more than quadrupled compared to pulse at -0.4 V. This increase can be explained by the more favored reduction of desorbed NO_2 species to NH_3 at -0.9 V as seen by decreasing NO_2 yield and increased NH_3 yield rate at more negative potentials. The reason for decreasing NH_3 F.E. is explained by the increasing H_2 yield at -0.9 V pulse. However, this increase in H_2 yield is not counterintuitive for NH_3, possibly due to the superior protonation properties of the material. Also, more negative bias and less NO_3 concentration on the electrode are not a dominant parameter for Co/NS-rGO NO_3RR at the pre-reduced

electrode. The positive effect of -0.9 V pulse is not observed for NO_3RR at the bare electrode, possibly due to the inability of bare Co/NS-rGO to cause NO_2 desorption. Also, as of -0.4 V pulse, -0.9 V pulse does not favor NO_2RR but disturbs the facile reduction of NO_2 on Co/NS-rGO.

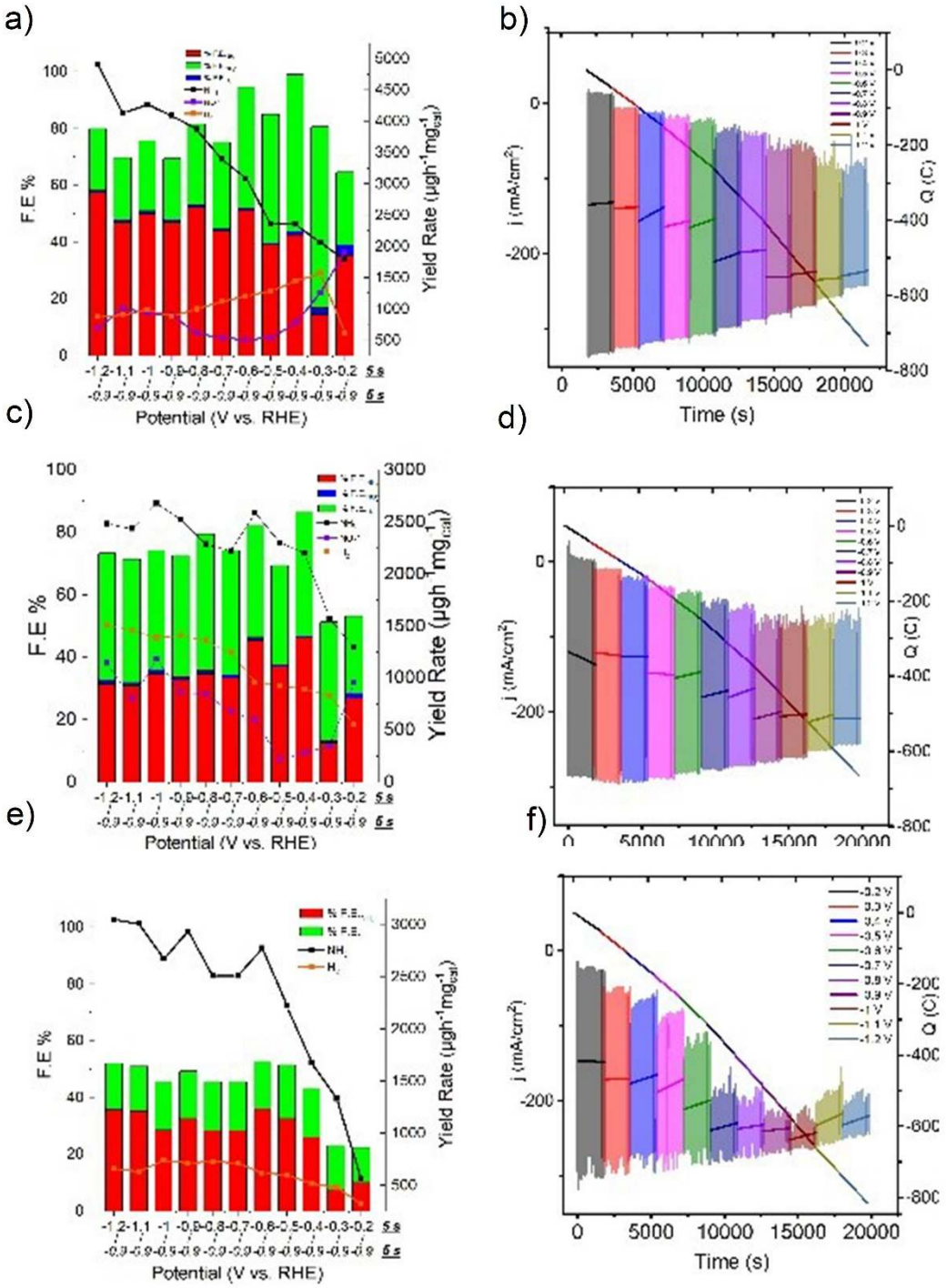

Figure 4-33: Pulsed Nitrate to ammonia electrosynthesis activity of Co/NS-rGO for 2 s at constant electrolysis potentials and pulsed potential of -0.9 V. a) NO_2^-, NH_3, H_2 F.E., and Y.R. of Co/NS-rGO after pre-reduction at -1.5 V in 0.1 M KOH + 0.1 M KNO_3. b) j and q values for

Co/NS-rGO NO_3RR after pre-reduction at -1.5 V. c) NO_2^-, NH_3, H_2 F.E. and Y.R. of Co/NS-rGO in 0.1 M KOH + 0.1 M KNO_3 d) j and q values for Co/NS-rGO NO_3RR e) NO_2^-, NH_3, H_2 F.E. and Y.R. of Co/NS-rGO in 0.1 M KOH + 0.1 M KNO_2 f) j and q values for Co/NS-rGO NO_2RR

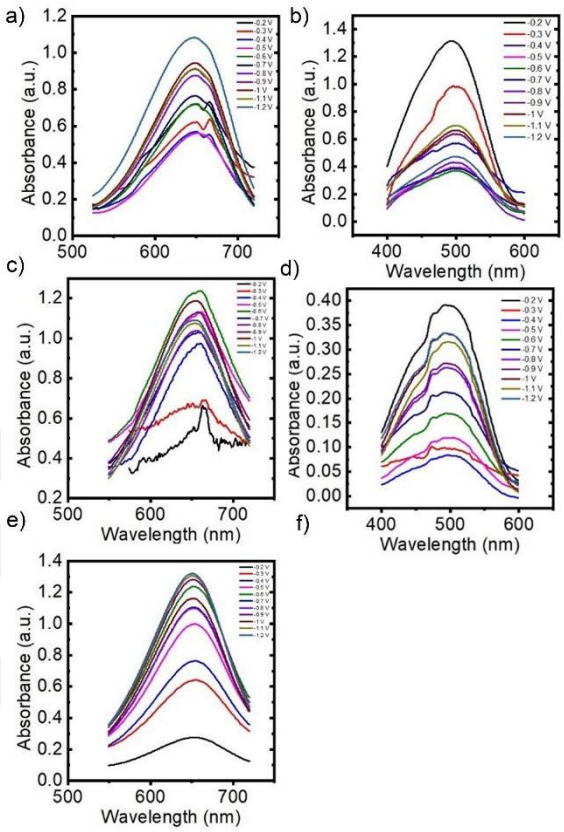

Figure 4-34: UV-vis spectroscopy results after pulsed NO_3RR and NO_2RR experiments at constant electrolysis potentials and pulsed potential of -0.9 V for 2 s. a) NH_3 quantification using the Indophenol Blue Method for Co/NS-rGO NO_3RR after pre-reduction at -1.5 V. b) NO_2 quantification using the Griess Test for Co/NS-rGO after pre-reduction at -1.5 V. c) NH_3 quantification using the Indophenol Blue Method for Co/NS-rGO NO_3RR without pre-reduction at -1.5 V. d) NO_2 quantification using the Griess Test for Co/NS-rGO without pre-reduction at -1.5 V. e) NH_3 quantification using the Indophenol Blue Method for Co/NS-rGO NO_2RR.

Pulsed electroreduction tests at -0.9 V for Co/NS-rGO 900 show that H_2 production is further increased for Co/NS-rGO 900 in these experiments owing to already superior HER properties of Co/NS-rGO is facilitated more than NH_3 production is suppressed (Fig. 4-35). Opposing Co/NS-rGO, Co/NS-rGO 900 has poor protonation properties, which is the reason for suppressed NO_3RR. Furthermore, Co/NS-rGO 900 has a lower NH_3 yield than Co/NS-rGO at pulse at -0.9 V. Its NH_3 yield is higher at constant CA measurements due to Co/NS-rGO 900 lacking NO_2 desorption properties. It is not mass-transfer limited at more positive potentials and poor protonation properties.

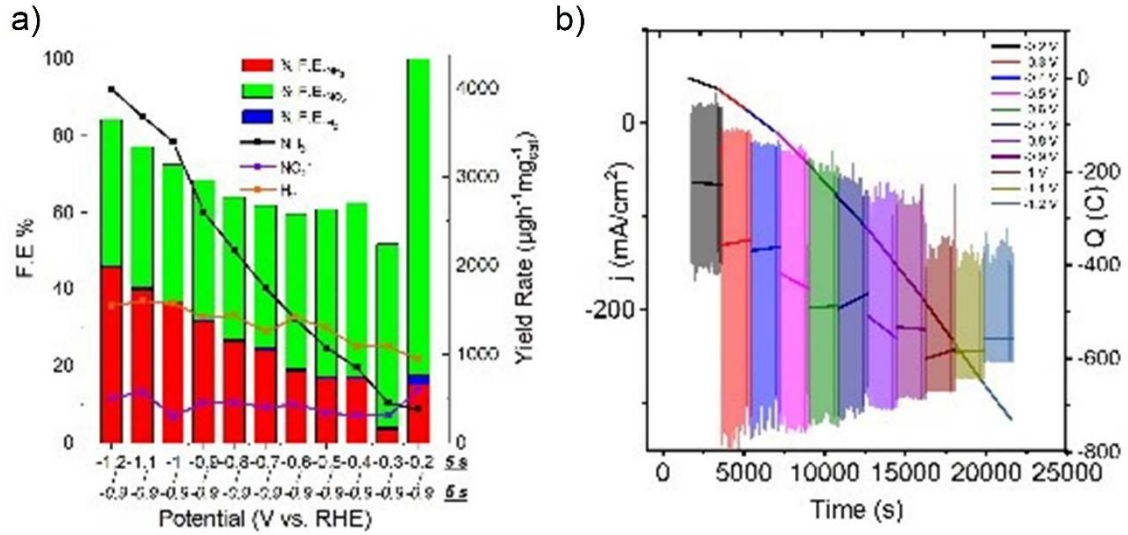

Figure 4-35: Pulsed Nitrate to ammonia electrosynthesis activity of Co/NS-rGO 900 for 2 s at constant electrolysis potentials and pulsed potential of -0.9 V. a) NO_2^-, NH_3, H_2 F.E., and Y.R. of Co/NS-rGO after pre-reduction at -1.5 V in 0.1 M KOH + 0.1 M KNO_3. b) j and q values for Co/NS-rGO NO_3RR after pre-reduction at -1.5 V.

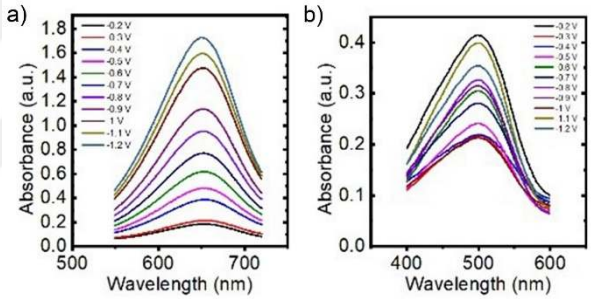

Figure 4-36: UV-vis spectroscopy results after pulsed NO_3RR and NO_2RR experiments at constant electrolysis potentials and pulsed potential of -0.9 V for 2 s. a) NH_3 quantification using the Indophenol Blue Method for Co/NS-rGO 900 NO_3RR after pre-reduction at -1.5 V. b) NO_2 quantification using the Griess Test for Co/NS-rGO 900 after pre-reduction at -1.5 V.

4.9 *Conclusion*

This work adopts Co/NS-rGO and Co/NS-rGO 900 catalysts as two model catalysts. The former consists of CoS moieties, while the latter has an amorphous structure with CoO particles. XAS study told us that two different mechanisms emerge for these catalysts: a mass-transfer limited mechanism for the former and a mechanism lacking a protonation step in NO_3RR for the latter. It was observed that the presence of CoS species facilitates NO_2RR and CoO species to promote HER. Pulsed electrolysis experiments results show that mass-transfer limited Co/NS-rGO favors more NH_3 production, possibly due to the reduction of desorbed NO2 species or superior

protonation properties of the material, while pulsed CA measurements suppress NH_3 production for Co/NS-rGO 900 and facilitate HER .

Chapter 5:
Conclusion and Future Outlook

In this thesis, characterization and electrochemical screenings of Co decorated N, S doped Reduced Graphene Oxide (Co/NS-rGO) catalysts are carried out comprehensively. For the ORR study, we conclude that an optimum amount of Co (Co/NS-rGO) can induce CoS species along with Co SAs that facilitate ORR better than its more metal-loaded counterparts. We observed that CoS species favor the 4e- pathway while CoO species lead to the $2e^-$ peroxide pathway. Also, the Co/NS-rGO catalyst is found to have better utilization of its active sites through ECSA-normalized RDE and RRDE analyses. Furthermore, we investigated the origin of ORR activity through the electronic properties of the material. The density of states, charge carrier concentration, flatband potential, and charge storage properties of Co/NS-rGO being the most superior, along with its high ORR activity, allows us to signify the importance of having an optimum composition of the metal and favorable surface species in the catalyst.

In the NO_3RR study, we investigated two different catalysts, one subjected to high heat treatment, i.e., Co/NS-rGO 900, while the other was not pyrolyzed. We claimed that these two catalysts follow two different reaction mechanisms by examining XAS behavior and Tafel Analysis. Co/NS-rGO is found to follow a mass-transfer limited mechanism where the Co/NS-rGO 900 is not mass-transfer limited but favors HER. Furthermore, we investigated the desorption of NO_2 species using EIS techniques and DRT models. Also, we studied pulsed electrolysis to understand whether the shift in negative bias on the electrode, mass-transfer limited potential regime, or reduction of desorbed species enables higher NH_3 yield. We discovered that pulsed electrolysis was detrimental to the already high NO_2RR activity of Co/NS-rGO and resulted in higher H_2 production for Co/NS-rGO 900 and suppressed NH_3 production. However, pulsed electrolysis was beneficial to NH_3 F.E. and yield of Co/NS-rGO, possibly due to the elimination of mass-transfer limitations, modulation of desorbed or adsorbed surface species, or altering the negative bias in the vicinity of the electrode.

We project that EIS techniques, kinetic analysis, and spectroscopic methods can be more accessible and informative in understanding reaction mechanisms and enhancing electrochemical activities. Also, very low metal loading, 1-5%, dispersion on high

surface area supports such as graphene with N and S elemental contents through doping can pave the way for electrochemically active surface species.

After improvements in the durability of the catalyst, one can operate transition metal dispersed high surface area catalysts in industrial applications to replace scarce and expensive PGM catalysts. The in-depth kinetic and mechanistic analysis of catalysts toward electrochemical reactions allows us to design more active catalysts that can perform in the desired range.

BIBLIOGRAPHY

[1] Z. W. Seh, J. Kibsgaard, C. F. Dickens, I. Chorkendorff, J. K. Nørskov, and T. F. Jaramillo, "Combining theory and experiment in electrocatalysis: Insights into materials design," *Science*, vol. 355, no. 6321, p. eaad4998, Jan. 2017, doi: 10.1126/science.aad4998.

[2] S. Chu and A. Majumdar, "Opportunities and challenges for a sustainable energy future," *Nature*, vol. 488, no. 7411, Art. no. 7411, Aug. 2012, doi: 10.1038/nature11475.

[3] T. M. Gür, "Review of electrical energy storage technologies, materials, and systems: challenges and prospects for large-scale grid storage," *Energy Environ. Sci.*, vol. 11, no. 10, pp. 2696–2767, Oct. 2018, doi: 10.1039/C8EE01419A.

[4] D. A. J. Rand, "A journey on the electrochemical road to sustainability," *J Solid State Electrochem*, vol. 15, no. 7, pp. 1579–1622, Jul. 2011, doi: 10.1007/s10008-011-1410-z.

[5] O. Gröger, H. A. Gasteiger, and J.-P. Suchsland, "Review—Electromobility: Batteries or Fuel Cells?," *J. Electrochem. Soc.*, vol. 162, no. 14, p. A2605, Oct. 2015, doi: 10.1149/2.0211514jes.

[6] J.-M. Tarascon and M. Armand, "Issues and challenges facing rechargeable lithium batteries," *Nature*, vol. 414, no. 6861, pp. 359–367, Nov. 2001, doi: 10.1038/35104644.

[7] J.-X. Liu, D. Richards, N. Singh, and B. R. Goldsmith, "Activity and Selectivity Trends in Electrocatalytic Nitrate Reduction on Transition Metals," *ACS Catal.*, vol. 9, no. 8, pp. 7052–7064, Aug. 2019, doi: 10.1021/acscatal.9b02179.

[8] K. P. Kuhl, T. Hatsukade, E. R. Cave, D. N. Abram, J. Kibsgaard, and T. F. Jaramillo, "Electrocatalytic Conversion of Carbon Dioxide to Methane and Methanol on Transition Metal Surfaces," *J. Am. Chem. Soc.*, vol. 136, no. 40, pp. 14107–14113, Oct. 2014, doi: 10.1021/ja505791r.

[9] V. Kyriakou, I. Garagounis, A. Vourros, E. Vasileiou, and M. Stoukides, "An Electrochemical Haber-Bosch Process," *Joule*, vol. 4, no. 1, pp. 142–158, Jan. 2020, doi: 10.1016/j.joule.2019.10.006.

[10] N. A. Baharuddin, W. N. A. Wan Yusoff, A. J. Abd Aziz, and N. N. Mohd Tahir, "Hydrogen fuel cells for sustainable energy: Development and progress in selected developed countries," *IOP Conf. Ser.: Mater. Sci. Eng.*, vol. 1078, no. 1, p. 012011, Feb. 2021, doi: 10.1088/1757-899X/1078/1/012011.

[11] O. Antoine, Y. Bultel, and R. Durand, "Oxygen reduction reaction kinetics and mechanism on platinum nanoparticles inside Nafion®," *Journal of Electroanalytical Chemistry*, vol. 499, no. 1, pp. 85–94, Feb. 2001, doi: 10.1016/S0022-0728(00)00492-7.

[12] K. Artyushkova, A. Serov, S. Rojas-Carbonell, and P. Atanassov, "Chemistry of Multitudinous Active Sites for Oxygen Reduction Reaction in Transition Metal–Nitrogen–Carbon Electrocatalysts," *J. Phys. Chem. C*, vol. 119, no. 46, pp. 25917–25928, Nov. 2015, doi: 10.1021/acs.jpcc.5b07653.

[13] C. H. Christensen, T. Johannessen, R. Z. Sørensen, and J. K. Nørskov, "Towards an ammonia-mediated hydrogen economy?," *Catalysis Today*, vol. 111, no. 1, pp. 140–144, Jan. 2006, doi: 10.1016/j.cattod.2005.10.011.

[14] M. K. Debe, "Electrocatalyst approaches and challenges for automotive fuel cells," *Nature*, vol. 486, no. 7401, Art. no. 7401, Jun. 2012, doi: 10.1038/nature11115.

[15] J. Kibsgaard, J. K. Nørskov, and I. Chorkendorff, “The Difficulty of Proving Electrochemical Ammonia Synthesis,” *ACS Energy Lett.*, vol. 4, no. 12, pp. 2986–2988, Dec. 2019, doi: 10.1021/acsenergylett.9b02286.
[16] M. E. Kreider *et al.*, “Strategies for Modulating the Catalytic Activity and Selectivity of Manganese Antimonates for the Oxygen Reduction Reaction,” *ACS Catal.*, vol. 12, no. 17, pp. 10826–10840, Sep. 2022, doi: 10.1021/acscatal.2c01764.
[17] J. K. Nørskov *et al.*, “Universality in Heterogeneous Catalysis,” *Journal of Catalysis*, vol. 209, no. 2, pp. 275–278, Jul. 2002, doi: 10.1006/jcat.2002.3615.
[18] D. Guo, R. Shibuya, C. Akiba, S. Saji, T. Kondo, and J. Nakamura, “Active sites of nitrogen-doped carbon materials for oxygen reduction reaction clarified using model catalysts,” *Science*, vol. 351, no. 6271, pp. 361–365, Jan. 2016, doi: 10.1126/science.aad0832.
[19] T. Asset and P. Atanassov, “Iron-Nitrogen-Carbon Catalysts for Proton Exchange Membrane Fuel Cells,” *Joule*, vol. 4, no. 1, pp. 33–44, Jan. 2020, doi: 10.1016/j.joule.2019.12.002.
[20] E. Murphy *et al.*, “Elucidating electrochemical nitrate and nitrite reduction over atomically-dispersed transition metal sites,” Chemistry, preprint, Nov. 2022. doi: 10.26434/chemrxiv-2022-xhfjc.
[21] J. Ni *et al.*, “Atomic Co─P Catalytic Pair Drives Efficient Electrochemical Nitrate Reduction to Ammonia,” *Advanced Energy Materials*, vol. n/a, no. n/a, p. 2400065, doi: 10.1002/aenm.202400065.
[22] “Cobalt Sulfide Nanoparticles Grown on Nitrogen and Sulfur Codoped Graphene Oxide: An Efficient Electrocatalyst for Oxygen Reduction and Evolution Reactions | ACS Catalysis.” Accessed: Jan. 12, 2023. [Online]. Available: https://pubs.acs.org/doi/10.1021/acscatal.5b00154
[23] L. Bu *et al.*, “Biaxially strained PtPb/Pt core/shell nanoplate boosts oxygen reduction catalysis,” *Science*, vol. 354, no. 6318, pp. 1410–1414, Dec. 2016, doi: 10.1126/science.aah6133.
[24] K. Sasaki *et al.*, “Core-Protected Platinum Monolayer Shell High-Stability Electrocatalysts for Fuel-Cell Cathodes,” *Angewandte Chemie International Edition*, vol. 49, no. 46, pp. 8602–8607, 2010, doi: 10.1002/anie.201004287.
[25] J. Duan, S. Chen, M. Jaroniec, and S. Z. Qiao, “Heteroatom-Doped Graphene-Based Materials for Energy-Relevant Electrocatalytic Processes,” *ACS Catal.*, vol. 5, no. 9, pp. 5207–5234, Sep. 2015, doi: 10.1021/acscatal.5b00991.
[26] A. H. Castro Neto, F. Guinea, N. M. R. Peres, K. S. Novoselov, and A. K. Geim, “The electronic properties of graphene,” *Rev. Mod. Phys.*, vol. 81, no. 1, pp. 109–162, Jan. 2009, doi: 10.1103/RevModPhys.81.109.
[27] A. K. Geim and K. S. Novoselov, “The rise of graphene,” *Nature Mater*, vol. 6, no. 3, Art. no. 3, Mar. 2007, doi: 10.1038/nmat1849.
[28] “Graphene: Status and Prospects | Science.” Accessed: Jul. 30, 2023. [Online]. Available: https://www.science.org/doi/10.1126/science.1158877
[29] “Superior Thermal Conductivity of Single-Layer Graphene | Nano Letters.” Accessed: Jul. 30, 2023. [Online]. Available: https://pubs.acs.org/doi/full/10.1021/nl0731872?casa_token=G7O_QQifuaAAAAA%3AejUfAnOx416S03UQvfsbuq_MGG1kk-SO_FdiWcxvQOXzw5PVYUBlT24FKi7tbLTi6jkGb_rN2V-bWg0
[30] F. Bonaccorso, Z. Sun, T. Hasan, and A. C. Ferrari, “Graphene photonics and optoelectronics,” *Nature Photonics*, vol. 4, no. 9, pp. 611–622, 2010, doi: 10.1038/nphoton.2010.186.

[31] H. Fei *et al.*, “Atomic cobalt on nitrogen-doped graphene for hydrogen generation,” *Nat Commun*, vol. 6, no. 1, Art. no. 1, Oct. 2015, doi: 10.1038/ncomms9668.
[32] S. Park and R. S. Ruoff, “Chemical methods for the production of graphenes,” *Nature Nanotech*, vol. 4, no. 4, Art. no. 4, Apr. 2009, doi: 10.1038/nnano.2009.58.
[33] Y. Shao, Z. Jiang, Q. Zhang, and J. Guan, “Progress in Nonmetal-Doped Graphene Electrocatalysts for the Oxygen Reduction Reaction,” *ChemSusChem*, vol. 12, no. 10, pp. 2133–2146, 2019, doi: 10.1002/cssc.201900060.
[34] C. Berger *et al.*, “Electronic Confinement and Coherence in Patterned Epitaxial Graphene,” *Science*, vol. 312, no. 5777, pp. 1191–1196, May 2006, doi: 10.1126/science.1125925.
[35] K. S. Novoselov *et al.*, “Electric Field Effect in Atomically Thin Carbon Films,” *Science*, vol. 306, no. 5696, pp. 666–669, Oct. 2004, doi: 10.1126/science.1102896.
[36] R. Ruoff, “Calling all chemists,” *Nature Nanotech*, vol. 3, no. 1, Art. no. 1, Jan. 2008, doi: 10.1038/nnano.2007.432.
[37] D. C. Marcano *et al.*, “Improved Synthesis of Graphene Oxide,” *ACS Nano*, vol. 4, no. 8, pp. 4806–4814, Aug. 2010, doi: 10.1021/nn1006368.
[38] S. Park *et al.*, “Aqueous Suspension and Characterization of Chemically Modified Graphene Sheets,” *Chem. Mater.*, vol. 20, no. 21, pp. 6592–6594, Nov. 2008, doi: 10.1021/cm801932u.
[39] S. Park *et al.*, “Colloidal Suspensions of Highly Reduced Graphene Oxide in a Wide Variety of Organic Solvents,” *Nano Lett.*, vol. 9, no. 4, pp. 1593–1597, Apr. 2009, doi: 10.1021/nl803798y.
[40] “Graphene Oxide, Highly Reduced Graphene Oxide, and Graphene: Versatile Building Blocks for Carbon-Based Materials - Compton - 2010 - Small - Wiley Online Library.” Accessed: Aug. 01, 2023. [Online]. Available: https://onlinelibrary.wiley.com/doi/full/10.1002/smll.200901934
[41] D. W. Boukhvalov and M. I. Katsnelson, “Chemical Functionalization of Graphene with Defects,” *Nano Lett.*, vol. 8, no. 12, pp. 4373–4379, Dec. 2008, doi: 10.1021/nl802234n.
[42] Y. Ito, W. Cong, Takeshi Fujita, Z. Tang, and M. Chen, “High Catalytic Activity of Nitrogen and Sulfur Co-Doped Nanoporous Graphene in the Hydrogen Evolution Reaction,” *Angewandte Chemie International Edition*, vol. 54, no. 7, pp. 2131–2136, 2015, doi: 10.1002/anie.201410050.
[43] T. Y. Ma, S. Dai, M. Jaroniec, and S. Z. Qiao, “Metal–Organic Framework Derived Hybrid Co3O4-Carbon Porous Nanowire Arrays as Reversible Oxygen Evolution Electrodes,” *J. Am. Chem. Soc.*, vol. 136, no. 39, pp. 13925–13931, Oct. 2014, doi: 10.1021/ja5082553.
[44] X.-X. Ma and X.-Q. He, “Cobalt oxide anchored on nitrogen and sulfur dual-doped graphene foam as an effective oxygen electrode catalyst in alkaline media,” *Applied Materials Today*, vol. 4, pp. 1–8, 2016, doi: 10.1016/j.apmt.2016.04.002.
[45] L. Qu, Y. Liu, J.-B. Baek, and L. Dai, “Nitrogen-Doped Graphene as Efficient Metal-Free Electrocatalyst for Oxygen Reduction in Fuel Cells,” *ACS Nano*, vol. 4, no. 3, pp. 1321–1326, Mar. 2010, doi: 10.1021/nn901850u.
[46] H. Wang, T. Maiyalagan, and X. Wang, “Review on Recent Progress in Nitrogen-Doped Graphene: Synthesis, Characterization, and Its Potential Applications,” *ACS Catal.*, vol. 2, no. 5, pp. 781–794, May 2012, doi: 10.1021/cs200652y.

[47] K. Gong, F. Du, Z. Xia, M. Durstock, and L. Dai, “Nitrogen-Doped Carbon Nanotube Arrays with High Electrocatalytic Activity for Oxygen Reduction,” *Science*, vol. 323, no. 5915, pp. 760–764, Feb. 2009, doi: 10.1126/science.1168049.

[48] D. Guo, R. Shibuya, C. Akiba, S. Saji, T. Kondo, and J. Nakamura, “Active sites of nitrogen-doped carbon materials for oxygen reduction reaction clarified using model catalysts,” *Science*, vol. 351, no. 6271, pp. 361–365, Jan. 2016, doi: 10.1126/science.aad0832.

[49] J. P. Paraknowitsch and A. Thomas, “Doping carbons beyond nitrogen: an overview of advanced heteroatom doped carbons with boron, sulphur and phosphorus for energy applications,” *Energy Environ. Sci.*, vol. 6, no. 10, pp. 2839–2855, Sep. 2013, doi: 10.1039/C3EE41444B.

[50] J. Liang, Y. Jiao, M. Jaroniec, and S. Z. Qiao, “Sulfur and Nitrogen Dual-Doped Mesoporous Graphene Electrocatalyst for Oxygen Reduction with Synergistically Enhanced Performance,” *Angewandte Chemie International Edition*, vol. 51, no. 46, pp. 11496–11500, 2012, doi: 10.1002/anie.201206720.

[51] Y. Su *et al.*, “Low-temperature synthesis of nitrogen/sulfur co-doped three-dimensional graphene frameworks as efficient metal-free electrocatalyst for oxygen reduction reaction,” *Carbon*, vol. 62, pp. 296–301, Oct. 2013, doi: 10.1016/j.carbon.2013.05.067.

[52] C. H. Choi, S. H. Park, and S. I. Woo, “Binary and Ternary Doping of Nitrogen, Boron, and Phosphorus into Carbon for Enhancing Electrochemical Oxygen Reduction Activity,” *ACS Nano*, vol. 6, no. 8, pp. 7084–7091, Aug. 2012, doi: 10.1021/nn3021234.

[53] C. H. Choi, M. W. Chung, S. H. Park, and S. I. Woo, “Additional doping of phosphorus and/or sulfur into nitrogen-doped carbon for efficient oxygen reduction reaction in acidic media,” *Phys. Chem. Chem. Phys.*, vol. 15, no. 6, pp. 1802–1805, Jan. 2013, doi: 10.1039/C2CP44147K.

[54] D. Jang *et al.*, “Production of P, N Co-doped Graphene-Based Materials by a Solution Process and Their Electrocatalytic Performance for Oxygen Reduction Reaction,” *ChemNanoMat*, vol. 4, no. 1, pp. 118–123, 2018, doi: 10.1002/cnma.201700241.

[55] J. Ozaki, T. Anahara, N. Kimura, and A. Oya, “Simultaneous doping of boron and nitrogen into a carbon to enhance its oxygen reduction activity in proton exchange membrane fuel cells,” *Carbon*, vol. 44, no. 15, pp. 3358–3361, Dec. 2006, doi: 10.1016/j.carbon.2006.08.022.

[56] Y. Ito, H.-J. Qiu, T. Fujita, Y. Tanabe, K. Tanigaki, and M. Chen, “Bicontinuous Nanoporous N-doped Graphene for the Oxygen Reduction Reaction,” *Advanced Materials*, vol. 26, no. 24, pp. 4145–4150, 2014, doi: 10.1002/adma.201400570.

[57] L. Zhang and Z. Xia, “Mechanisms of Oxygen Reduction Reaction on Nitrogen-Doped Graphene for Fuel Cells,” *J. Phys. Chem. C*, vol. 115, no. 22, pp. 11170–11176, Jun. 2011, doi: 10.1021/jp201991j.

[58] “Graphene-Based Materials for Energy Conversion - Sahoo - 2012 - Advanced Materials - Wiley Online Library.” Accessed: Aug. 04, 2023. [Online]. Available: https://onlinelibrary.wiley.com/doi/10.1002/adma.201104971

[59] Y. Liang *et al.*, “Co3O4 nanocrystals on graphene as a synergistic catalyst for oxygen reduction reaction,” *Nature Mater*, vol. 10, no. 10, Art. no. 10, Oct. 2011, doi: 10.1038/nmat3087.

[60] Z.-H. Sheng, L. Shao, J.-J. Chen, W.-J. Bao, F.-B. Wang, and X.-H. Xia, “Catalyst-Free Synthesis of Nitrogen-Doped Graphene via Thermal Annealing

Graphite Oxide with Melamine and Its Excellent Electrocatalysis," *ACS Nano*, vol. 5, no. 6, pp. 4350–4358, Jun. 2011, doi: 10.1021/nn103584t.
[61] L. Lai *et al.*, "Exploration of the active center structure of nitrogen-doped graphene-based catalysts for oxygen reduction reaction," *Energy & Environmental Science*, vol. 5, no. 7, pp. 7936–7942, 2012, doi: 10.1039/C2EE21802J.
[62] A. Zitolo *et al.*, "Identification of catalytic sites for oxygen reduction in iron- and nitrogen-doped graphene materials," *Nature Mater*, vol. 14, no. 9, Art. no. 9, Sep. 2015, doi: 10.1038/nmat4367.
[63] N. Solati *et al.*, "Pyridinic nitrogen induced compressed bilayer graphene for oxygen reduction reaction," *Materials Today Energy*, vol. 35, p. 101323, Jul. 2023, doi: 10.1016/j.mtener.2023.101323.
[64] T. Wang *et al.*, "Identifying the Active Site of N-Doped Graphene for Oxygen Reduction by Selective Chemical Modification," *ACS Energy Lett.*, vol. 3, no. 4, pp. 986–991, Apr. 2018, doi: 10.1021/acsenergylett.8b00258.
[65] H. W. Kim *et al.*, "Mechanisms of Two-Electron and Four-Electron Electrochemical Oxygen Reduction Reactions at Nitrogen-Doped Reduced Graphene Oxide," *ACS Catal.*, vol. 10, no. 1, pp. 852–863, Jan. 2020, doi: 10.1021/acscatal.9b04106.
[66] J. Li, R. Valenza, and S. Haussener, "In Situ Synthesis of CuxO/N Doped Graphdiyne with Pyridine N Configuration for Ammonia Production via Nitrate Reduction," *Small*, vol. 20, no. 33, p. 2310467, 2024, doi: 10.1002/smll.202310467.
[67] Y. Zhu *et al.*, "Sustainable nitrogen-doped carbons from coking wastewater and spent coffee grounds for electrocatalytic nitrate to ammonia conversion," *Journal of Environmental Chemical Engineering*, vol. 12, no. 4, p. 113132, Aug. 2024, doi: 10.1016/j.jece.2024.113132.
[68] J. P. Donahue, "Thermodynamic Scales for Sulfur Atom Transfer and Oxo-for-Sulfido Exchange Reactions," *Chem. Rev.*, vol. 106, no. 11, pp. 4747–4783, Nov. 2006, doi: 10.1021/cr050044w.
[69] "In situ Surface Chemistry Engineering of Cobalt-Sulfide Nanosheets for Improved Oxygen Evolution Activity | ACS Applied Energy Materials." Accessed: Dec. 04, 2022. [Online]. Available: https://pubs.acs.org/doi/10.1021/acsaem.9b00687
[70] M. S. Faber, M. A. Lukowski, Q. Ding, N. S. Kaiser, and S. Jin, "Earth-Abundant Metal Pyrites (FeS2, CoS2, NiS2, and Their Alloys) for Highly Efficient Hydrogen Evolution and Polysulfide Reduction Electrocatalysis," *J. Phys. Chem. C*, vol. 118, no. 37, pp. 21347–21356, Sep. 2014, doi: 10.1021/jp506288w.
[71] X. Liang *et al.*, "Recent Advances in Designing Efficient Electrocatalysts for Electrochemical Nitrate Reduction to Ammonia," *Small Structures*, vol. n/a, no. n/a, p. 2200202, doi: 10.1002/sstr.202200202.
[72] "Recent Advances in Electrocatalysts for Oxygen Reduction Reaction | Chemical Reviews." Accessed: Dec. 31, 2022. [Online]. Available: https://pubs.acs.org/doi/10.1021/acs.chemrev.5b00462
[73] Y. Jia *et al.*, "Efficient Nitrate-to-Ammonia Electroreduction at Cobalt Phosphide Nanoshuttles," *ACS Appl. Mater. Interfaces*, vol. 13, no. 38, pp. 45521–45527, Sep. 2021, doi: 10.1021/acsami.1c12512.
[74] K. Yang, S.-H. Han, C. Cheng, C. Guo, T. Li, and Y. Yu, "Unveiling the Reaction Mechanism of Nitrate Reduction to Ammonia Over Cobalt-Based Electrocatalysts," *J. Am. Chem. Soc.*, vol. 146, no. 19, pp. 12976–12983, May 2024, doi: 10.1021/jacs.3c13517.

[75] X. Wang *et al.*, "One-pot synthesis of nitrogen and sulfur co-doped graphene as efficient metal-free electrocatalysts for the oxygen reduction reaction," *Chem. Commun.*, vol. 50, no. 37, pp. 4839–4842, Apr. 2014, doi: 10.1039/C4CC00440J.
[76] S.-A. Wohlgemuth, R. J. White, M.-G. Willinger, M.-M. Titirici, and M. Antonietti, "A one-pot hydrothermal synthesis of sulfur and nitrogen doped carbon aerogels with enhanced electrocatalytic activity in the oxygen reduction reaction," *Green Chem.*, vol. 14, no. 5, pp. 1515–1523, May 2012, doi: 10.1039/C2GC35309A.
[77] P. A. Denis, R. Faccio, and A. W. Mombru, "Is It Possible to Dope Single-Walled Carbon Nanotubes and Graphene with Sulfur?," *ChemPhysChem*, vol. 10, no. 4, pp. 715–722, 2009, doi: 10.1002/cphc.200800592.
[78] Z. Yang *et al.*, "Sulfur-Doped Graphene as an Efficient Metal-free Cathode Catalyst for Oxygen Reduction," *ACS Nano*, vol. 6, no. 1, pp. 205–211, Jan. 2012, doi: 10.1021/nn203393d.
[79] N. Ramaswamy and S. Mukerjee, "Fundamental Mechanistic Understanding of Electrocatalysis of Oxygen Reduction on Pt and Non-Pt Surfaces: Acid versus Alkaline Media," *Advances in Physical Chemistry*, vol. 2012, pp. 1–17, Mar. 2012, doi: 10.1155/2012/491604.
[80] R. Sibul *et al.*, "Sulphur and nitrogen co-doped graphene-based electrocatalysts for oxygen reduction reaction in alkaline medium," *Electrochemistry Communications*, vol. 109, p. 106603, Dec. 2019, doi: 10.1016/j.elecom.2019.106603.
[81] S. Wang *et al.*, "BCN Graphene as Efficient Metal-Free Electrocatalyst for the Oxygen Reduction Reaction," *Angewandte Chemie International Edition*, vol. 51, no. 17, pp. 4209–4212, 2012, doi: 10.1002/anie.201109257.
[82] W. Ai *et al.*, "Nitrogen and Sulfur Codoped Graphene: Multifunctional Electrode Materials for High-Performance Li-Ion Batteries and Oxygen Reduction Reaction," *Advanced Materials*, vol. 26, no. 35, pp. 6186–6192, 2014, doi: 10.1002/adma.201401427.
[83] J. Xu, G. Dong, C. Jin, M. Huang, and L. Guan, "Sulfur and Nitrogen Co-Doped, Few-Layered Graphene Oxide as a Highly Efficient Electrocatalyst for the Oxygen-Reduction Reaction," *ChemSusChem*, vol. 6, no. 3, pp. 493–499, 2013, doi: 10.1002/cssc.201200564.
[84] H. Zhang, X. Liu, G. He, X. Zhang, S. Bao, and W. Hu, "Bioinspired synthesis of nitrogen/sulfur co-doped graphene as an efficient electrocatalyst for oxygen reduction reaction," *Journal of Power Sources*, vol. 279, pp. 252–258, Apr. 2015, doi: 10.1016/j.jpowsour.2015.01.016.
[85] S. C. Roy, A. W. Harding, A. E. Russell, and K. M. Thomas, "Spectroelectrochemical Study of the Role Played by Carbon Functionality in Fuel Cell Electrodes," *J. Electrochem. Soc.*, vol. 144, no. 7, p. 2323, Jul. 1997, doi: 10.1149/1.1837812.
[86] S. Ye, A. K. Vijh, and L. H. Dao, "A New Fuel Cell Electrocatalyst Based on Carbonized Polyacrylonitrile Foam: The Nature of Platinum-Support Interactions," *J. Electrochem. Soc.*, vol. 144, no. 1, p. 90, Jan. 1997, doi: 10.1149/1.1837369.
[87] O. Benabdallah *et al.*, "Cobalt hydroxide/heteroatom doped graphene composite as electrocalyst for oxygen reduction reaction," presented at the Proceedings of 2018 6th International Renewable and Sustainable Energy Conference, IRSEC 2018, 2018. doi: 10.1109/IRSEC.2018.8702979.

[88] C. Wei *et al.*, “A Three-Dimensionally Structured Electrocatalyst: Cobalt-Embedded Nitrogen-Doped Carbon Nanotubes/Nitrogen-Doped Reduced Graphene Oxide Hybrid for Efficient Oxygen Reduction,” *Chemistry – A European Journal*, vol. 23, no. 3, pp. 637–643, 2017, doi: 10.1002/chem.201604113.

[89] P. Cai, J. Huang, J. Chen, and Z. Wen, “Oxygen-Containing Amorphous Cobalt Sulfide Porous Nanocubes as High-Activity Electrocatalysts for the Oxygen Evolution Reaction in an Alkaline/Neutral Medium,” *Angewandte Chemie International Edition*, vol. 56, no. 17, pp. 4858–4861, 2017, doi: 10.1002/anie.201701280.

[90] L. Yao, K. E. Rivera-Cruz, P. M. Zimmerman, N. Singh, and C. C. L. McCrory, “Electrochemical CO2 Reduction to Methanol by Cobalt Phthalocyanine: Quantifying CO2 and CO Binding Strengths and Their Influence on Methanol Production,” *ACS Catal.*, vol. 14, no. 1, pp. 366–372, Jan. 2024, doi: 10.1021/acscatal.3c04957.

[91] S. Gupta, R. Fernandes, R. Patel, M. Spreitzer, and N. Patel, “A review of cobalt-based catalysts for sustainable energy and environmental applications,” *Applied Catalysis A: General*, vol. 661, p. 119254, Jul. 2023, doi: 10.1016/j.apcata.2023.119254.

[92] H. B. Yang *et al.*, “Nitrogen and sulfur Co-doped graphene inlaid with cobalt clusters for efficient oxygen reduction reaction,” *Materials Today Energy*, vol. 10, pp. 184–190, Dec. 2018, doi: 10.1016/j.mtener.2018.09.011.

[93] P. Ganesan, M. Prabu, J. Sanetuntikul, and S. Shanmugam, “Cobalt Sulfide Nanoparticles Grown on Nitrogen and Sulfur Codoped Graphene Oxide: An Efficient Electrocatalyst for Oxygen Reduction and Evolution Reactions,” *ACS Catal.*, vol. 5, no. 6, pp. 3625–3637, Jun. 2015, doi: 10.1021/acscatal.5b00154.

[94] Q. Liu, J. Jin, and J. Zhang, “NiCo2S4@graphene as a Bifunctional Electrocatalyst for Oxygen Reduction and Evolution Reactions,” *ACS Appl. Mater. Interfaces*, vol. 5, no. 11, pp. 5002–5008, Jun. 2013, doi: 10.1021/am4007897.

[95] Z. Luo *et al.*, “Preparation of Cobalt Sulfide Nanoparticle-Decorated Nitrogen and Sulfur Co-Doped Reduced Graphene Oxide Aerogel Used as a Highly Efficient Electrocatalyst for Oxygen Reduction Reaction,” *Small*, vol. 12, no. 43, pp. 5920–5926, Nov. 2016, doi: 10.1002/smll.201602615.

[96] V. Nallathambi, J.-W. Lee, S. P. Kumaraguru, G. Wu, and B. N. Popov, “Development of high performance carbon composite catalyst for oxygen reduction reaction in PEM Proton Exchange Membrane fuel cells,” *Journal of Power Sources*, vol. 183, no. 1, pp. 34–42, Aug. 2008, doi: 10.1016/j.jpowsour.2008.05.020.

[97] G. Gruenig, K. Wiesener, S. Gamburzev, I. Iliev, and A. Kaisheva, “Investigations of catalysts from the pyrolyzates of cobalt-containing and metal-free dibenzotetraazaannulenes on active carbon for oxygen electrodes in an acid medium,” *Journal of Electroanalytical Chemistry and Interfacial Electrochemistry*, vol. 159, no. 1, pp. 155–162, Dec. 1983, doi: 10.1016/S0022-0728(83)80321-0.

[98] Y. Guo, J. R. Stroka, B. Kandemir, C. E. Dickerson, and K. L. Bren, “Cobalt Metallopeptide Electrocatalyst for the Selective Reduction of Nitrite to Ammonium,” *J. Am. Chem. Soc.*, vol. 140, no. 49, pp. 16888–16892, Dec. 2018, doi: 10.1021/jacs.8b09612.

[99] W. He *et al.*, “Splicing the active phases of copper/cobalt-based catalysts achieves high-rate tandem electroreduction of nitrate to ammonia,” *Nat Commun*, vol. 13, no. 1, Art. no. 1, Mar. 2022, doi: 10.1038/s41467-022-28728-4.

[100] A. Wang, J. Li, and T. Zhang, “Heterogeneous single-atom catalysis,” *Nat Rev Chem*, vol. 2, no. 6, Art. no. 6, Jun. 2018, doi: 10.1038/s41570-018-0010-1.
[101] C. Zhu, S. Fu, Q. Shi, D. Du, and Y. Lin, “Single-Atom Electrocatalysts,” *Angewandte Chemie International Edition*, vol. 56, no. 45, pp. 13944–13960, 2017, doi: 10.1002/anie.201703864.
[102] Y. Chen *et al.*, “Isolated Single Iron Atoms Anchored on N-Doped Porous Carbon as an Efficient Electrocatalyst for the Oxygen Reduction Reaction,” *Angewandte Chemie - International Edition*, vol. 56, no. 24, pp. 6937–6941, 2017, doi: 10.1002/anie.201702473.
[103] L. Jiao, G. Wan, R. Zhang, H. Zhou, S.-H. Yu, and H.-L. Jiang, “From Metal–Organic Frameworks to Single-Atom Fe Implanted N-doped Porous Carbons: Efficient Oxygen Reduction in Both Alkaline and Acidic Media,” *Angewandte Chemie - International Edition*, vol. 57, no. 28, pp. 8525–8529, 2018, doi: 10.1002/anie.201803262.
[104] P. Yin *et al.*, “Single Cobalt Atoms with Precise N-Coordination as Superior Oxygen Reduction Reaction Catalysts,” *Angewandte Chemie - International Edition*, vol. 55, no. 36, pp. 10800–10805, 2016, doi: 10.1002/anie.201604802.
[105] R. Lin *et al.*, “Approaching Theoretical Performances of Electrocatalytic Hydrogen Peroxide Generation by Cobalt-Nitrogen Moieties,” *Angewandte Chemie*, vol. 135, no. 21, p. e202301433, 2023, doi: 10.1002/ange.202301433.
[106] J. Gao *et al.*, “Enabling Direct H2O2 Production in Acidic Media through Rational Design of Transition Metal Single Atom Catalyst,” *Chem*, vol. 6, no. 3, pp. 658–674, Mar. 2020, doi: 10.1016/j.chempr.2019.12.008.
[107] R. A. Sidik and A. B. Anderson, “Co9S8 as a Catalyst for Electroreduction of O2: Quantum Chemistry Predictions,” *J. Phys. Chem. B*, vol. 110, no. 2, pp. 936–941, Jan. 2006, doi: 10.1021/jp054487f.
[108] Y. Ren, S. You, Y. Wang, J. Yang, and Y. Liu, “Bioinspired Tandem Electrode for Selective Electrocatalytic Synthesis of Ammonia from Aqueous Nitrate,” *Environ. Sci. Technol.*, vol. 58, no. 4, pp. 2144–2152, Jan. 2024, doi: 10.1021/acs.est.3c09759.
[109] E. Murphy *et al.*, “Highly Durable and Selective Fe- and Mo-Based Atomically Dispersed Electrocatalysts for Nitrate Reduction to Ammonia via Distinct and Synergized NO2– Pathways,” *ACS Catal.*, vol. 12, no. 11, pp. 6651–6662, Jun. 2022, doi: 10.1021/acscatal.2c01367.
[110] X. Rui, H. Tan, and Q. Yan, “Nanostructured metal sulfides for energy storage,” *Nanoscale*, vol. 6, no. 17, pp. 9889–9924, Aug. 2014, doi: 10.1039/C4NR03057E.
[111] P. Wu *et al.*, “A N-doped graphene–cobalt nickel sulfide aerogel as a sulfur host for lithium–sulfur batteries,” *RSC Adv.*, vol. 9, no. 55, pp. 32247–32257, Oct. 2019, doi: 10.1039/C9RA05202J.
[112] J. Zhang, L. Yu, and X. W. D. Lou, “Embedding CoS2 nanoparticles in N-doped carbon nanotube hollow frameworks for enhanced lithium storage properties,” *Nano Res.*, vol. 10, no. 12, pp. 4298–4304, Dec. 2017, doi: 10.1007/s12274-016-1394-1.
[113] Y. Gu, Y. Xu, and Y. Wang, “Graphene-Wrapped CoS Nanoparticles for High-Capacity Lithium-Ion Storage,” *ACS Appl. Mater. Interfaces*, vol. 5, no. 3, pp. 801–806, Feb. 2013, doi: 10.1021/am3023652.
[114] X. Zhao, J. Jiang, Z. Xue, C. Yan, and T. Mu, “An ambient temperature, CO2-assisted solution processing of amorphous cobalt sulfide in a thiol/amine based quasi-ionic liquid for oxygen evolution catalysis,” *Chem. Commun.*, vol. 53, no. 68, pp. 9418–9421, Aug. 2017, doi: 10.1039/C7CC05503J.

[115] Y. Sun *et al.*, "Electrodeposited Cobalt-Sulfide Catalyst for Electrochemical and Photoelectrochemical Hydrogen Generation from Water," *J. Am. Chem. Soc.*, vol. 135, no. 47, pp. 17699–17702, Nov. 2013, doi: 10.1021/ja4094764.
[116] N. Wang, L. Li, D. Zhao, X. Kang, Z. Tang, and S. Chen, "Graphene Composites with Cobalt Sulfide: Efficient Trifunctional Electrocatalysts for Oxygen Reversible Catalysis and Hydrogen Production in the Same Electrolyte," *Small*, vol. 13, no. 33, p. 1701025, 2017, doi: 10.1002/smll.201701025.
[117] J. K. Nørskov *et al.*, "Origin of the Overpotential for Oxygen Reduction at a Fuel-Cell Cathode," *J. Phys. Chem. B*, vol. 108, no. 46, pp. 17886–17892, Nov. 2004, doi: 10.1021/jp047349j.
[118] A. M. Gómez-Marín and J. M. Feliu, "New Insights into the Oxygen Reduction Reaction Mechanism on Pt (111): A Detailed Electrochemical Study," *ChemSusChem*, vol. 6, no. 6, pp. 1091–1100, 2013, doi: 10.1002/cssc.201200847.
[119] T. Hu, C. Wang, M. Wang, C. M. Li, and C. Guo, "Theoretical Insights into Superior Nitrate Reduction to Ammonia Performance of Copper Catalysts," *ACS Catal.*, vol. 11, no. 23, pp. 14417–14427, Dec. 2021, doi: 10.1021/acscatal.1c03666.
[120] J. Wu and Y.-X. Yu, "Highly selective electroreduction of nitrate to ammonia on a Ru-doped tetragonal Co2P monolayer with low-limiting overpotential," *Catal. Sci. Technol.*, vol. 11, no. 21, pp. 7160–7170, Nov. 2021, doi: 10.1039/D1CY01217G.
[121] S. Fletcher, "Tafel slopes from first principles," *J Solid State Electrochem*, vol. 13, no. 4, pp. 537–549, Apr. 2009, doi: 10.1007/s10008-008-0670-8.
[122] J. Chlistunoff, "RRDE and Voltammetric Study of ORR on Pyrolyzed Fe/Polyaniline Catalyst. On the Origins of Variable Tafel Slopes," *J. Phys. Chem. C*, vol. 115, no. 14, pp. 6496–6507, Apr. 2011, doi: 10.1021/jp108350t.
[123] G.-F. Chen *et al.*, "Electrochemical reduction of nitrate to ammonia via direct eight-electron transfer using a copper–molecular solid catalyst," *Nat Energy*, vol. 5, no. 8, Art. no. 8, Aug. 2020, doi: 10.1038/s41560-020-0654-1.
[124] H. Gerischer, "Electron-transfer kinetics of redox reactions at the semiconductor/electrolyte contact. A new approach," *J. Phys. Chem.*, vol. 95, no. 3, pp. 1356–1359, Feb. 1991, doi: 10.1021/j100156a060.
[125] N. Ramaswamy and S. Mukerjee, "Influence of Inner- and Outer-Sphere Electron Transfer Mechanisms during Electrocatalysis of Oxygen Reduction in Alkaline Media," *J. Phys. Chem. C*, vol. 115, no. 36, pp. 18015–18026, Sep. 2011, doi: 10.1021/jp204680p.
[126] G.-F. Chen *et al.*, "Ammonia Electrosynthesis with High Selectivity under Ambient Conditions via a Li+ Incorporation Strategy," *J. Am. Chem. Soc.*, vol. 139, no. 29, pp. 9771–9774, Jul. 2017, doi: 10.1021/jacs.7b04393.
[127] J. Timoshenko *et al.*, "Steering the structure and selectivity of CO2 electroreduction catalysts by potential pulses," *Nat Catal*, vol. 5, no. 4, pp. 259–267, Apr. 2022, doi: 10.1038/s41929-022-00760-z.
[128] A. R. Singh *et al.*, "Electrochemical Ammonia Synthesis—The Selectivity Challenge," *ACS Catal.*, vol. 7, no. 1, pp. 706–709, Jan. 2017, doi: 10.1021/acscatal.6b03035.
[129] H. A. Gasteiger, J. E. Panels, and S. G. Yan, "Dependence of PEM fuel cell performance on catalyst loading," *Journal of Power Sources*, vol. 127, no. 1, pp. 162–171, Mar. 2004, doi: 10.1016/j.jpowsour.2003.09.013.
[130] W. Cai, X. Zhao, C. Liu, W. Xing, and J. Zhang, "2 - Electrode Kinetics of Electron-Transfer Reaction and Reactant Transport in Electrolyte Solution," in *Rotating Electrode Methods and Oxygen Reduction Electrocatalysts*, W. Xing, G.

Yin, and J. Zhang, Eds., Amsterdam: Elsevier, 2014, pp. 33–65. doi: 10.1016/B978-0-444-63278-4.00002-1.
[131] P. Wang, Z. Wang, L. Jia, and Z. Xiao, "Origin of the catalytic activity of graphite nitride for the electrochemical reduction of oxygen: geometric factors vs. electronic factors," *Phys. Chem. Chem. Phys.*, vol. 11, no. 15, pp. 2730–2740, Mar. 2009, doi: 10.1039/B818408A.
[132] Y. Zhou, T. Holme, J. Berry, T. R. Ohno, D. Ginley, and R. O'Hayre, "Dopant-Induced Electronic Structure Modification of HOPG Surfaces: Implications for High Activity Fuel Cell Catalysts," *J. Phys. Chem. C*, vol. 114, no. 1, pp. 506–515, Jan. 2010, doi: 10.1021/jp9088386.
[133] Z. Wang, D. Richards, and N. Singh, "Recent discoveries in the reaction mechanism of heterogeneous electrocatalytic nitrate reduction," *Catal. Sci. Technol.*, vol. 11, no. 3, pp. 705–725, Feb. 2021, doi: 10.1039/D0CY02025G.
[134] J. Guo *et al.*, "Mass Transport Modifies the Interfacial Electrolyte to Influence Electrochemical Nitrate Reduction," *ACS Sustainable Chemistry and Engineering*, vol. 11, no. 20, pp. 7882–7893, 2023, doi: 10.1021/acssuschemeng.3c01057.
[135] J.-Q. Chen, X.-X. Ye, D. Zhou, and Y.-X. Chen, "Roles of Copper in Nitrate Reduction at Copper-Modified Ru/C Catalysts," *J. Phys. Chem. C*, vol. 127, no. 6, pp. 2918–2928, Feb. 2023, doi: 10.1021/acs.jpcc.2c07813.
[136] D. Reyter, D. Bélanger, and L. Roué, "Study of the electroreduction of nitrate on copper in alkaline solution," *Electrochimica Acta*, vol. 53, no. 20, pp. 5977–5984, Aug. 2008, doi: 10.1016/j.electacta.2008.03.048.
[137] Y. Xiong, Y. Wang, J. Zhou, F. Liu, F. Hao, and Z. Fan, "Electrochemical Nitrate Reduction: Ammonia Synthesis and the Beyond," *Advanced Materials*, vol. n/a, no. n/a, p. 2304021, doi: 10.1002/adma.202304021.
[138] M. Duca and M. T. M. Koper, "Powering denitrification: the perspectives of electrocatalytic nitrate reduction," *Energy Environ. Sci.*, vol. 5, no. 12, pp. 9726–9742, Nov. 2012, doi: 10.1039/C2EE23062C.
[139] L. E. Harris, "The lower electronic states of nitrite and nitrate ion, nitromethane, nitramide, nitric acid, and nitrate esters," *The Journal of Chemical Physics*, vol. 58, no. 12, pp. 5615–5626, Jun. 1973, doi: 10.1063/1.1679185.
[140] Y. Wang *et al.*, "Enhanced Nitrate-to-Ammonia Activity on Copper–Nickel Alloys via Tuning of Intermediate Adsorption," *J. Am. Chem. Soc.*, vol. 142, no. 12, pp. 5702–5708, Mar. 2020, doi: 10.1021/jacs.9b13347.
[141] Z. Wang, S. D. Young, B. R. Goldsmith, and N. Singh, "Increasing electrocatalytic nitrate reduction activity by controlling adsorption through PtRu alloying," *Journal of Catalysis*, vol. 395, pp. 143–154, Mar. 2021, doi: 10.1016/j.jcat.2020.12.031.
[142] Y. Wang, W. Zhou, R. Jia, Y. Yu, and B. Zhang, "Unveiling the Activity Origin of a Copper-based Electrocatalyst for Selective Nitrate Reduction to Ammonia," *Angewandte Chemie International Edition*, vol. 59, no. 13, pp. 5350–5354, 2020, doi: 10.1002/anie.201915992.
[143] G. Zhang, X. Li, K. Chen, Y. Guo, D. Ma, and K. Chu, "Tandem Electrocatalytic Nitrate Reduction to Ammonia on MBenes", doi: 10.1002/anie.202300054.
[144] Y. Zhou, R. Duan, H. Li, M. Zhao, C. Ding, and C. Li, "Boosting Electrocatalytic Nitrate Reduction to Ammonia via Promoting Water Dissociation," *ACS Catal.*, vol. 13, no. 16, pp. 10846–10854, Aug. 2023, doi: 10.1021/acscatal.3c02951.

[145] A. J. Bard, L. R. Faulkner, and H. S. White, *Electrochemical Methods: Fundamentals and Applications*. John Wiley & Sons, 2022.
[146] "Identification of Active Edge Sites for Electrochemical H2 Evolution from MoS2 Nanocatalysts | Science." Accessed: Jul. 10, 2023. [Online]. Available: https://www.science.org/doi/10.1126/science.1141483
[147] Md. M. Hossain, T. Kawaguchi, K. Shimazu, and K. Nakata, "Reduction of nitrate on tin-modified palladium-platinum electrodes," *Journal of Electroanalytical Chemistry*, vol. 864, p. 114041, May 2020, doi: 10.1016/j.jelechem.2020.114041.
[148] C. Hammond, "Crystals and crystal structures," in *The Basics of Crystallography and Diffraction*, C. Hammond, Ed., Oxford University Press, 2015, p. 0. doi: 10.1093/acprof:oso/9780198738671.003.0001.
[149] L. G. Cançado *et al.*, "Quantifying Defects in Graphene via Raman Spectroscopy at Different Excitation Energies," *Nano Lett.*, vol. 11, no. 8, pp. 3190–3196, Aug. 2011, doi: 10.1021/nl201432g.
[150] A. C. Ferrari, "Raman spectroscopy of graphene and graphite: Disorder, electron–phonon coupling, doping and nonadiabatic effects," *Solid State Communications*, vol. 143, no. 1, pp. 47–57, Jul. 2007, doi: 10.1016/j.ssc.2007.03.052.
[151] J. F. Moulder and J. Chastain, Eds., *Handbook of X-ray photoelectron spectroscopy: a reference book of standard spectra for identification and interpretation of XPS data*, Update. Eden Prairie, Minn: Perkin-Elmer Corporation, 1992.
[152] T. Susi, T. Pichler, and P. Ayala, "X-ray photoelectron spectroscopy of graphitic carbon nanomaterials doped with heteroatoms," *Beilstein J. Nanotechnol.*, vol. 6, pp. 177–192, Jan. 2015, doi: 10.3762/bjnano.6.17.
[153] A. Z. Laila *et al.*, "Comparative study of a high-entropy metal disulfide and its parent compounds using x-ray absorption spectroscopy," *Phys. Rev. B*, vol. 109, no. 19, p. 195129, May 2024, doi: 10.1103/PhysRevB.109.195129.
[154] J. E. Vilasó-Cadre *et al.*, "Voltammetry and Related Electrochemical Methods Based on Low-Cost Instrumentation: a Review from Basic to Advanced," *J Anal Chem*, vol. 79, no. 5, pp. 520–539, May 2024, doi: 10.1134/S1061934824050150.
[155] G. Wiberg, K. Mayhofer, and M. Arenz, "Investigation of the Oxygen Reduction Activity of non-Platinum Catalysts - a RDE Methodology," *ECS Trans.*, vol. 19, no. 31, p. 37, Nov. 2009, doi: 10.1149/1.3271360.
[156] E. S. F. Cardoso, G. V. Fortunato, and G. Maia, "Use of Rotating Ring-Disk Electrodes to Investigate Graphene Nanoribbon Loadings for the Oxygen Reduction Reaction in Alkaline Medium," *ChemElectroChem*, vol. 5, no. 13, pp. 1691–1701, 2018, doi: 10.1002/celc.201800331.
[157] C. C. L. McCrory, S. Jung, J. C. Peters, and T. F. Jaramillo, "Benchmarking Heterogeneous Electrocatalysts for the Oxygen Evolution Reaction," *J. Am. Chem. Soc.*, vol. 135, no. 45, pp. 16977–16987, Nov. 2013, doi: 10.1021/ja407115p.
[158] S. Wang, J. Zhang, O. Gharbi, V. Vivier, M. Gao, and M. E. Orazem, "Electrochemical impedance spectroscopy," *Nat Rev Methods Primers*, vol. 1, no. 1, Art. no. 1, Jun. 2021, doi: 10.1038/s43586-021-00039-w.
[159] B. Bera, A. Chakraborty, T. Kar, P. Leuaa, and M. Neergat, "Density of States, Carrier Concentration, and Flat Band Potential Derived from Electrochemical Impedance Measurements of N-Doped Carbon and Their Influence on Electrocatalysis of Oxygen Reduction Reaction," *J. Phys. Chem. C*, vol. 121, no. 38, pp. 20850–20856, Sep. 2017, doi: 10.1021/acs.jpcc.7b06735.

[160] Z. P. Cano *et al.*, “Batteries and fuel cells for emerging electric vehicle markets,” *Nat Energy*, vol. 3, no. 4, Art. no. 4, Apr. 2018, doi: 10.1038/s41560-018-0108-1.
[161] R. L. Borup *et al.*, “Recent developments in catalyst-related PEM fuel cell durability,” *Current Opinion in Electrochemistry*, vol. 21, pp. 192–200, Jun. 2020, doi: 10.1016/j.coelec.2020.02.007.
[162] B. Pivovar, “Catalysts for fuel cell transportation and hydrogen related uses,” *Nat Catal*, vol. 2, no. 7, Art. no. 7, Jul. 2019, doi: 10.1038/s41929-019-0320-9.
[163] I. E. L. Stephens, J. Rossmeisl, and I. Chorkendorff, “Toward sustainable fuel cells,” *Science*, vol. 354, no. 6318, pp. 1378–1379, Dec. 2016, doi: 10.1126/science.aal3303.
[164] “The Priority and Challenge of High-Power Performance of Low-Platinum Proton-Exchange Membrane Fuel Cells | The Journal of Physical Chemistry Letters.” Accessed: Jul. 25, 2023. [Online]. Available: https://pubs.acs.org/doi/full/10.1021/acs.jpclett.6b00216
[165] B. James and S. Analysis, “Fuel Cell Systems Analysis”.
[166] M. S. Wilson and S. Gottesfeld, “Thin-film catalyst layers for polymer electrolyte fuel cell electrodes,” *J Appl Electrochem*, vol. 22, no. 1, pp. 1–7, Jan. 1992, doi: 10.1007/BF01093004.
[167] “Catalyzing the Hydrogen Evolution Reaction (HER) with Molybdenum Sulfide Nanomaterials | ACS Catalysis.” Accessed: Jul. 10, 2023. [Online]. Available: https://pubs.acs.org/doi/10.1021/cs500923c
[168] “Activity benchmarks and requirements for Pt, Pt-alloy, and non-Pt oxygen reduction catalysts for PEMFCs - ScienceDirect.” Accessed: Jul. 11, 2023. [Online]. Available: https://www.sciencedirect.com/science/article/pii/S0926337304004941
[169] X. X. Wang, M. T. Swihart, and G. Wu, “Achievements, challenges and perspectives on cathode catalysts in proton exchange membrane fuel cells for transportation,” *Nat Catal*, vol. 2, no. 7, Art. no. 7, Jul. 2019, doi: 10.1038/s41929-019-0304-9.
[170] Y. Shao, J.-P. Dodelet, G. Wu, and P. Zelenay, “PGM-Free Cathode Catalysts for PEM Fuel Cells: A Mini-Review on Stability Challenges,” *Advanced Materials*, vol. 31, no. 31, p. 1807615, 2019, doi: 10.1002/adma.201807615.
[171] T. Toda, H. Igarashi, H. Uchida, and M. Watanabe, “Enhancement of the Electroreduction of Oxygen on Pt Alloys with Fe, Ni, and Co,” *J. Electrochem. Soc.*, vol. 146, no. 10, p. 3750, Oct. 1999, doi: 10.1149/1.1392544.
[172] M. Kato *et al.*, “Enhancement of Electrocatalytic Oxygen Reduction Activity and Durability of Pt–Ni Rhombic Dodecahedral Nanoframes by Anchoring to Nitrogen-Doped Carbon Support,” *ACS Omega*, vol. 3, no. 8, pp. 9052–9059, Aug. 2018, doi: 10.1021/acsomega.8b01373.
[173] U. A. Paulus *et al.*, “Oxygen Reduction on Carbon-Supported Pt−Ni and Pt−Co Alloy Catalysts,” *J. Phys. Chem. B*, vol. 106, no. 16, pp. 4181–4191, Apr. 2002, doi: 10.1021/jp013442l.
[174] L. Chong *et al.*, “Ultralow-loading platinum-cobalt fuel cell catalysts derived from imidazolate frameworks,” *Science*, vol. 362, no. 6420, pp. 1276–1281, Dec. 2018, doi: 10.1126/science.aau0630.
[175] J. Greeley *et al.*, “Alloys of platinum and early transition metals as oxygen reduction electrocatalysts,” *Nature Chem*, vol. 1, no. 7, Art. no. 7, Oct. 2009, doi: 10.1038/nchem.367.

[176] F. Xiao *et al.*, “Atomically dispersed Pt and Fe sites and Pt–Fe nanoparticles for durable proton exchange membrane fuel cells,” *Nat Catal*, vol. 5, no. 6, Art. no. 6, Jun. 2022, doi: 10.1038/s41929-022-00796-1.
[177] B. Lim *et al.*, “Pd-Pt Bimetallic Nanodendrites with High Activity for Oxygen Reduction,” *Science*, vol. 324, no. 5932, pp. 1302–1305, Jun. 2009, doi: 10.1126/science.1170377.
[178] M. Li *et al.*, “Ultrafine jagged platinum nanowires enable ultrahigh mass activity for the oxygen reduction reaction,” *Science*, vol. 354, no. 6318, pp. 1414–1419, Dec. 2016, doi: 10.1126/science.aaf9050.
[179] G. Wu, K. L. More, C. M. Johnston, and P. Zelenay, “High-Performance Electrocatalysts for Oxygen Reduction Derived from Polyaniline, Iron, and Cobalt,” *Science*, vol. 332, no. 6028, pp. 443–447, Apr. 2011, doi: 10.1126/science.1200832.
[180] F. Jaouen *et al.*, “Cross-Laboratory Experimental Study of Non-Noble-Metal Electrocatalysts for the Oxygen Reduction Reaction,” *ACS Appl. Mater. Interfaces*, vol. 1, no. 8, pp. 1623–1639, Aug. 2009, doi: 10.1021/am900219g.
[181] H. T. Chung *et al.*, “Direct atomic-level insight into the active sites of a high-performance PGM-free ORR catalyst,” *Science*, vol. 357, no. 6350, pp. 479–484, Aug. 2017, doi: 10.1126/science.aan2255.
[182] M. Lefèvre, E. Proietti, F. Jaouen, and J.-P. Dodelet, “Iron-Based Catalysts with Improved Oxygen Reduction Activity in Polymer Electrolyte Fuel Cells,” *Science*, vol. 324, no. 5923, pp. 71–74, Apr. 2009, doi: 10.1126/science.1170051.
[183] A. Mehmood *et al.*, “High loading of single atomic iron sites in Fe–NC oxygen reduction catalysts for proton exchange membrane fuel cells,” *Nat Catal*, vol. 5, no. 4, Art. no. 4, Apr. 2022, doi: 10.1038/s41929-022-00772-9.
[184] M. Gong, A. Mehmood, B. Ali, K.-W. Nam, and A. Kucernak, “Oxygen Reduction Reaction Activity in Non-Precious Single-Atom (M–N/C) Catalysts─Contribution of Metal and Carbon/Nitrogen Framework-Based Sites,” *ACS Catal.*, vol. 13, no. 10, pp. 6661–6674, May 2023, doi: 10.1021/acscatal.3c00356.
[185] X. Xie *et al.*, “Performance enhancement and degradation mechanism identification of a single-atom Co–N–C catalyst for proton exchange membrane fuel cells,” *Nat Catal*, vol. 3, no. 12, Art. no. 12, Dec. 2020, doi: 10.1038/s41929-020-00546-1.
[186] Y. He, S. Liu, C. Priest, Q. Shi, and G. Wu, “Atomically dispersed metal–nitrogen–carbon catalysts for fuel cells: advances in catalyst design, electrode performance, and durability improvement,” *Chemical Society Reviews*, vol. 49, no. 11, pp. 3484–3524, 2020, doi: 10.1039/C9CS00903E.
[187] X. Wan *et al.*, “Fe–N–C electrocatalyst with dense active sites and efficient mass transport for high-performance proton exchange membrane fuel cells,” *Nat Catal*, vol. 2, no. 3, Art. no. 3, Mar. 2019, doi: 10.1038/s41929-019-0237-3.
[188] J. Wu *et al.*, “Simultaneously Incorporating Atomically Dispersed Co-Nx Sites with Graphitic Carbon Layer-Wrapped Co9S8 Nanoparticles for Oxygen Reduction in Acidic Electrolyte,” *ChemElectroChem*, vol. 10, no. 12, p. e202300110, 2023, doi: 10.1002/celc.202300110.
[189] F. Liu *et al.*, “Fe/Co dual metal catalysts modulated by S-ligands for efficient acidic oxygen reduction in PEMFC,” *Science Advances*, vol. 9, no. 23, p. eadg0366, Jun. 2023, doi: 10.1126/sciadv.adg0366.

[190] A. A. Gewirth and M. S. Thorum, “Electroreduction of Dioxygen for Fuel-Cell Applications: Materials and Challenges,” *Inorg. Chem.*, vol. 49, no. 8, pp. 3557–3566, Apr. 2010, doi: 10.1021/ic9022486.

[191] V. C. A. Ficca *et al.*, “Exchange Current Density as an Effective Descriptor of Poisoning of Active Sites in Platinum Group Metal-free Electrocatalysts for Oxygen Reduction Reaction,” *ACS Catal.*, vol. 13, no. 4, pp. 2162–2175, Feb. 2023, doi: 10.1021/acscatal.2c05222.

[192] W. Jin, H. Du, S. Zheng, H. Xu, and Y. Zhang, “Comparison of the Oxygen Reduction Reaction between NaOH and KOH Solutions on a Pt Electrode: The Electrolyte-Dependent Effect,” *J. Phys. Chem. B*, vol. 114, no. 19, pp. 6542–6548, May 2010, doi: 10.1021/jp102367u.

[193] E. Proietti *et al.*, “Iron-based cathode catalyst with enhanced power density in polymer electrolyte membrane fuel cells,” *Nat Commun*, vol. 2, no. 1, Art. no. 1, Aug. 2011, doi: 10.1038/ncomms1427.

[194] L. Osmieri, D. A. Cullen, H. T. Chung, R. K. Ahluwalia, and K. C. Neyerlin, “Durability evaluation of a Fe–N–C catalyst in polymer electrolyte fuel cell environment via accelerated stress tests,” *Nano Energy*, vol. 78, p. 105209, Dec. 2020, doi: 10.1016/j.nanoen.2020.105209.

[195] C. Walling, “Fenton’s reagent revisited,” *Acc. Chem. Res.*, vol. 8, no. 4, pp. 125–131, Apr. 1975, doi: 10.1021/ar50088a003.

[196] R. Chenitz *et al.*, “A specific demetalation of Fe–N4 catalytic sites in the micropores of NC_Ar + NH3 is at the origin of the initial activity loss of the highly active Fe/N/C catalyst used for the reduction of oxygen in PEM fuel cells,” *Energy Environ. Sci.*, vol. 11, no. 2, pp. 365–382, Feb. 2018, doi: 10.1039/C7EE02302B.

[197] M. M. M. Alyobi, C. J. Barnett, and R. J. Cobley, “Effects of thermal annealing on the properties of mechanically exfoliated suspended and on-substrate few-layer graphene,” *Crystals*, vol. 7, no. 11, 2017, doi: 10.3390/cryst7110349.

[198] Y.-B. Sun *et al.*, “One-step synthesis of S, N dual-element doped rGO as an efficient electrocatalyst for ORR,” *Journal of Electroanalytical Chemistry*, vol. 940, 2023, doi: 10.1016/j.jelechem.2023.117489.

[199] H. B. Yang *et al.*, “Identification of catalytic sites for oxygen reduction and oxygen evolution in N-doped graphene materials: Development of highly efficient metal-free bifunctional electrocatalyst,” *Science Advances*, vol. 2, no. 4, p. e1501122, Apr. 2016, doi: 10.1126/sciadv.1501122.

[200] Z. Xiang, X. Zhou, G. Wan, G. Zhang, and D. Cao, “Improving Energy Conversion Efficiency of Dye-Sensitized Solar Cells by Modifying TiO2 Photoanodes with Nitrogen-Reduced Graphene Oxide,” *ACS Sustainable Chem. Eng.*, vol. 2, no. 5, pp. 1234–1240, May 2014, doi: 10.1021/sc5000732.

[201] T. N. Blanton and D. Majumdar, “X-ray diffraction characterization of polymer intercalated graphite oxide,” *Powder Diffraction*, vol. 27, no. 2, pp. 104–107, Jun. 2012, doi: 10.1017/S0885715612000292.

[202] Y. Guo, L. Gan, C. Shang, E. Wang, and J. Wang, “A Cake-Style CoS2@MoS2/RGO Hybrid Catalyst for Efficient Hydrogen Evolution,” *Advanced Functional Materials*, vol. 27, no. 5, p. 1602699, 2017, doi: 10.1002/adfm.201602699.

[203] T. Wang, L.-X. Wang, D.-L. Wu, W. Xia, and D.-Z. Jia, “Interaction between Nitrogen and Sulfur in Co-Doped Graphene and Synergetic Effect in Supercapacitor,” *Sci Rep*, vol. 5, no. 1, Art. no. 1, Apr. 2015, doi: 10.1038/srep09591.

[204] K. Zhang, L. L. Zhang, X. S. Zhao, and J. Wu, “Graphene/Polyaniline Nanofiber Composites as Supercapacitor Electrodes,” *Chem. Mater.*, vol. 22, no. 4, pp. 1392–1401, Feb. 2010, doi: 10.1021/cm902876u.

[205] M. A. Pimenta, G. Dresselhaus, M. S. Dresselhaus, L. G. Cançado, A. Jorio, and R. Saito, “Studying disorder in graphite-based systems by Raman spectroscopy,” *Phys. Chem. Chem. Phys.*, vol. 9, no. 11, pp. 1276–1290, Mar. 2007, doi: 10.1039/B613962K.

[206] A. C. Ferrari and D. M. Basko, “Raman spectroscopy as a versatile tool for studying the properties of graphene,” *Nature Nanotech*, vol. 8, no. 4, pp. 235–246, Apr. 2013, doi: 10.1038/nnano.2013.46.

[207] H. Wang, Y. Wang, X. Cao, M. Feng, and G. Lan, “Vibrational properties of graphene and graphene layers,” *Journal of Raman Spectroscopy*, vol. 40, no. 12, pp. 1791–1796, 2009, doi: 10.1002/jrs.2321.

[208] D. M. Basko, S. Piscanec, and A. C. Ferrari, “Electron-electron interactions and doping dependence of the two-phonon Raman intensity in graphene,” *Phys. Rev. B*, vol. 80, no. 16, p. 165413, Oct. 2009, doi: 10.1103/PhysRevB.80.165413.

[209] Q. Wu, X. Zhou, J. Xu, F. Cao, and C. Li, “Adenine Derivative Host with Interlaced 2D Structure and Dual Lithiophilic–Sulfiphilic Sites to Enable High-Loading Li–S Batteries,” *ACS Nano*, vol. 13, no. 8, pp. 9520–9532, Aug. 2019, doi: 10.1021/acsnano.9b04519.

[210] L. Zhu *et al.*, “Investigation of CoS2-based thin films as model catalysts for the oxygen reduction reaction,” *Journal of Catalysis*, vol. 258, no. 1, pp. 235–242, Aug. 2008, doi: 10.1016/j.jcat.2008.06.016.

[211] B. Dutta *et al.*, “Partial Surface Selenization of Cobalt Sulfide Microspheres for Enhancing the Hydrogen Evolution Reaction,” *ACS Catal.*, vol. 9, no. 1, pp. 456–465, Jan. 2019, doi: 10.1021/acscatal.8b02904.

[212] I. Uhlig, R. Szargan, H. W. Nesbitt, and K. Laajalehto, “Surface states and reactivity of pyrite and marcasite,” *Applied Surface Science*, vol. 179, no. 1, pp. 222–229, Jul. 2001, doi: 10.1016/S0169-4332(01)00283-5.

[213] G. Zhou *et al.*, “Fibrous Hybrid of Graphene and Sulfur Nanocrystals for High-Performance Lithium–Sulfur Batteries,” *ACS Nano*, vol. 7, no. 6, pp. 5367–5375, Jun. 2013, doi: 10.1021/nn401228t.

[214] T. Kato, Y. Yamada, Y. Nishikawa, T. Otomo, H. Sato, and S. Sato, “Origins of peaks of graphitic and pyrrolic nitrogen in N1s X-ray photoelectron spectra of carbon materials: quaternary nitrogen, tertiary amine, or secondary amine?,” *J Mater Sci*, vol. 56, no. 28, pp. 15798–15811, Oct. 2021, doi: 10.1007/s10853-021-06283-5.

[215] T. Schiros *et al.*, “Connecting Dopant Bond Type with Electronic Structure in N-Doped Graphene,” *Nano Lett.*, vol. 12, no. 8, pp. 4025–4031, Aug. 2012, doi: 10.1021/nl301409h.

[216] N. SpÄƒtaru and F. G. BÄƒnicÄƒ, “Catalytic hydrogen evolution in cathodic stripping voltammetry on a mercury electrode in the presence of cobalt(ii) ion and phenylthiourea or thiourea,” *Analyst*, vol. 126, no. 11, pp. 1907–1911, Nov. 2001, doi: 10.1039/b104606n.

[217] I. G. Casella and M. Gatta, “Study of the electrochemical deposition and properties of cobalt oxide species in citrate alkaline solutions,” *Journal of Electroanalytical Chemistry*, vol. 534, no. 1, pp. 31–38, Oct. 2002, doi: 10.1016/S0022-0728(02)01100-2.

[218] D. Huang, Y. Luo, S. Li, B. Zhang, Y. Shen, and M. Wang, "Active catalysts based on cobalt oxide@cobalt/N-C nanocomposites for oxygen reduction reaction in alkaline solutions," *Nano Res.*, vol. 7, no. 7, pp. 1054–1064, Jul. 2014, doi: 10.1007/s12274-014-0468-1.

[219] Y. Liang *et al.*, "Oxygen Reduction Electrocatalyst Based on Strongly Coupled Cobalt Oxide Nanocrystals and Carbon Nanotubes," *J. Am. Chem. Soc.*, vol. 134, no. 38, pp. 15849–15857, Sep. 2012, doi: 10.1021/ja305623m.

[220] A. J. Appleby and M. Savy, "Kinetics of oxygen reduction reactions involving catalytic decomposition of hydrogen peroxide: Application to porous and rotating ring-disk electrodes," *Journal of Electroanalytical Chemistry and Interfacial Electrochemistry*, vol. 92, no. 1, pp. 15–30, Sep. 1978, doi: 10.1016/S0022-0728(78)80113-2.

[221] T. S. Olson, S. Pylypenko, J. E. Fulghum, and P. Atanassov, "Bifunctional Oxygen Reduction Reaction Mechanism on Non-Platinum Catalysts Derived from Pyrolyzed Porphyrins," *J. Electrochem. Soc.*, vol. 157, no. 1, p. B54, Nov. 2009, doi: 10.1149/1.3248003.

[222] J. Zheng, Y. Yan, and B. Xu, "Correcting the Hydrogen Diffusion Limitation in Rotating Disk Electrode Measurements of Hydrogen Evolution Reaction Kinetics," *J. Electrochem. Soc.*, vol. 162, no. 14, p. F1470, Oct. 2015, doi: 10.1149/2.0501514jes.

[223] M. L. Perry, J. Newman, and E. J. Cairns, "Mass Transport in Gas-Diffusion Electrodes: A Diagnostic Tool for Fuel-Cell Cathodes," *J. Electrochem. Soc.*, vol. 145, no. 1, p. 5, Jan. 1998, doi: 10.1149/1.1838202.

[224] D. Barrera, M. Florent, K. Sapag, and T. J. Bandosz, "Insight into the Mechanism of Oxygen Reduction Reaction on Micro/Mesoporous Carbons: Ultramicropores versus Nitrogen-Containing Catalytic Centers in Ordered Pore Structure," *ACS Appl. Energy Mater.*, vol. 2, no. 10, pp. 7412–7424, Oct. 2019, doi: 10.1021/acsaem.9b01427.

[225] A. A. Kulikovsky and M. Eikerling, "Analytical solutions for impedance of the cathode catalyst layer in PEM fuel cell: Layer parameters from impedance spectrum without fitting," *Journal of Electroanalytical Chemistry*, vol. 691, pp. 13–17, Feb. 2013, doi: 10.1016/j.jelechem.2012.12.002.

[226] H. Gerischer, "An interpretation of the double layer capacity of graphite electrodes in relation to the density of states at the Fermi level," *J. Phys. Chem.*, vol. 89, no. 20, pp. 4249–4251, Sep. 1985, doi: 10.1021/j100266a020.

[227] J. D. Wiggins-Camacho and K. J. Stevenson, "Effect of Nitrogen Concentration on Capacitance, Density of States, Electronic Conductivity, and Morphology of N-Doped Carbon Nanotube Electrodes," *J. Phys. Chem. C*, vol. 113, no. 44, pp. 19082–19090, Nov. 2009, doi: 10.1021/jp907160v.

[228] R. Samal, S. Mondal, A. S. Gangan, B. Chakraborty, and C. S. Rout, "Comparative electrochemical energy storage performance of cobalt sulfide and cobalt oxide nanosheets: experimental and theoretical insights from density functional theory simulations," *Phys. Chem. Chem. Phys.*, vol. 22, no. 15, pp. 7903–7911, Apr. 2020, doi: 10.1039/C9CP06434F.

[229] V. Smil, "Detonator of the population explosion," *Nature*, vol. 400, no. 6743, pp. 415–415, Jul. 1999, doi: 10.1038/22672.

[230] N. Cao and G. Zheng, "Aqueous electrocatalytic N2 reduction under ambient conditions," *Nano Res.*, vol. 11, no. 6, pp. 2992–3008, Jun. 2018, doi: 10.1007/s12274-018-1987-y.

[231] R. Lan, J. T. S. Irvine, and S. Tao, “Ammonia and related chemicals as potential indirect hydrogen storage materials,” *International Journal of Hydrogen Energy*, vol. 37, no. 2, pp. 1482–1494, Jan. 2012, doi: 10.1016/j.ijhydene.2011.10.004.
[232] J. W. Erisman, M. A. Sutton, J. Galloway, Z. Klimont, and W. Winiwarter, “How a century of ammonia synthesis changed the world,” *Nature Geosci*, vol. 1, no. 10, Art. no. 10, Oct. 2008, doi: 10.1038/ngeo325.
[233] J. G. Chen *et al.*, “Beyond fossil fuel–driven nitrogen transformations,” *Science*, vol. 360, no. 6391, p. eaar6611, May 2018, doi: 10.1126/science.aar6611.
[234] J. N. Galloway *et al.*, “Transformation of the Nitrogen Cycle: Recent Trends, Questions, and Potential Solutions,” *Science*, vol. 320, no. 5878, pp. 889–892, May 2008, doi: 10.1126/science.1136674.
[235] G. Soloveichik, “Electrochemical synthesis of ammonia as a potential alternative to the Haber–Bosch process,” *Nat Catal*, vol. 2, no. 5, pp. 377–380, May 2019, doi: 10.1038/s41929-019-0280-0.
[236] X. Cui, C. Tang, and Q. Zhang, “A Review of Electrocatalytic Reduction of Dinitrogen to Ammonia under Ambient Conditions,” *Advanced Energy Materials*, vol. 8, no. 22, p. 1800369, 2018, doi: 10.1002/aenm.201800369.
[237] X. Fu *et al.*, “Calcium-mediated nitrogen reduction for electrochemical ammonia synthesis,” *Nat. Mater.*, vol. 23, no. 1, pp. 101–107, Jan. 2024, doi: 10.1038/s41563-023-01702-1.
[238] M.-M. Shi *et al.*, “Au Sub-Nanoclusters on TiO2 toward Highly Efficient and Selective Electrocatalyst for N2 Conversion to NH3 at Ambient Conditions,” *Advanced Materials*, vol. 29, no. 17, p. 1606550, 2017, doi: 10.1002/adma.201606550.
[239] Y. Wang *et al.*, “Generating Defect-Rich Bismuth for Enhancing the Rate of Nitrogen Electroreduction to Ammonia,” *Angewandte Chemie International Edition*, vol. 58, no. 28, pp. 9464–9469, 2019, doi: 10.1002/anie.201903969.
[240] S. J. Blair *et al.*, “Lithium-Mediated Electrochemical Nitrogen Reduction: Tracking Electrode–Electrolyte Interfaces via Time-Resolved Neutron Reflectometry,” *ACS Energy Lett.*, vol. 7, no. 6, pp. 1939–1946, Jun. 2022, doi: 10.1021/acsenergylett.1c02833.
[241] X. Guo, J. Gu, S. Lin, S. Zhang, Z. Chen, and S. Huang, “Tackling the Activity and Selectivity Challenges of Electrocatalysts toward the Nitrogen Reduction Reaction via Atomically Dispersed Biatom Catalysts,” *J. Am. Chem. Soc.*, vol. 142, no. 12, pp. 5709–5721, Mar. 2020, doi: 10.1021/jacs.9b13349.
[242] L. Zhang *et al.*, “Electrochemical Ammonia Synthesis via Nitrogen Reduction Reaction on a MoS2 Catalyst: Theoretical and Experimental Studies,” *Advanced Materials*, vol. 30, no. 28, p. 1800191, 2018, doi: 10.1002/adma.201800191.
[243] J. Bjarke Valbæk Mygind *et al.*, “Is Ethanol Essential for the Lithium-Mediated Nitrogen Reduction Reaction?,” *ChemSusChem*, vol. 16, no. 22, p. e202301011, 2023, doi: 10.1002/cssc.202301011.
[244] X. Fu *et al.*, “Continuous-flow electrosynthesis of ammonia by nitrogen reduction and hydrogen oxidation,” *Science*, vol. 379, no. 6633, pp. 707–712, Feb. 2023, doi: 10.1126/science.adf4403.
[245] C. Tang and S.-Z. Qiao, “How to explore ambient electrocatalytic nitrogen reduction reliably and insightfully,” *Chem. Soc. Rev.*, vol. 48, no. 12, pp. 3166–3180, Jun. 2019, doi: 10.1039/C9CS00280D.
[246] B. H. R. Suryanto, H.-L. Du, D. Wang, J. Chen, A. N. Simonov, and D. R. MacFarlane, “Challenges and prospects in the catalysis of electroreduction of

nitrogen to ammonia," *Nat Catal*, vol. 2, no. 4, Art. no. 4, Apr. 2019, doi: 10.1038/s41929-019-0252-4.
[247] S. Z. Andersen *et al.*, "A rigorous electrochemical ammonia synthesis protocol with quantitative isotope measurements," *Nature*, vol. 570, no. 7762, Art. no. 7762, Jun. 2019, doi: 10.1038/s41586-019-1260-x.
[248] V. Rosca, M. Duca, M. T. de Groot, and M. T. M. Koper, "Nitrogen Cycle Electrocatalysis," *Chem. Rev.*, vol. 109, no. 6, pp. 2209–2244, Jun. 2009, doi: 10.1021/cr8003696.
[249] P. H. van Langevelde, I. Katsounaros, and M. T. M. Koper, "Electrocatalytic Nitrate Reduction for Sustainable Ammonia Production," *Joule*, vol. 5, no. 2, pp. 290–294, Feb. 2021, doi: 10.1016/j.joule.2020.12.025.
[250] E. Abascal, L. Gómez-Coma, I. Ortiz, and A. Ortiz, "Global diagnosis of nitrate pollution in groundwater and review of removal technologies," *Science of The Total Environment*, vol. 810, p. 152233, Mar. 2022, doi: 10.1016/j.scitotenv.2021.152233.
[251] E. A. Davidson *et al.*, "Excess nitrogen in the U.S. environment: Trends, risks, and solutions," *Issues in Ecology*, no. 15, 2011, [Online]. Available: https://pubs.usgs.gov/publication/70032270
[252] W. A. Tarpeh and X. Chen, "Making wastewater obsolete: Selective separations to enable circular water treatment," *Environmental Science and Ecotechnology*, vol. 5, p. 100078, Jan. 2021, doi: 10.1016/j.ese.2021.100078.
[253] J. M. McEnaney *et al.*, "Electrolyte Engineering for Efficient Electrochemical Nitrate Reduction to Ammonia on a Titanium Electrode," *ACS Sustainable Chem. Eng.*, vol. 8, no. 7, pp. 2672–2681, Feb. 2020, doi: 10.1021/acssuschemeng.9b05983.
[254] I. Katsounaros, "On the assessment of electrocatalysts for nitrate reduction," *Current Opinion in Electrochemistry*, vol. 28, p. 100721, Aug. 2021, doi: 10.1016/j.coelec.2021.100721.
[255] J. Sun *et al.*, "A hybrid plasma electrocatalytic process for sustainable ammonia production," *Energy Environ. Sci.*, vol. 14, no. 2, pp. 865–872, Feb. 2021, doi: 10.1039/D0EE03769A.
[256] R. D. Milton and S. D. Minteer, "Enzymatic Bioelectrosynthetic Ammonia Production: Recent Electrochemistry of Nitrogenase, Nitrate Reductase, and Nitrite Reductase," *ChemPlusChem*, vol. 82, no. 4, pp. 513–521, 2017, doi: 10.1002/cplu.201600442.
[257] D. F. Abbott *et al.*, "Understanding the Synergy between Fe and Mo Sites in the Nitrate Reduction Reaction on a Bio-Inspired Bimetallic MXene Electrocatalyst," *Angewandte Chemie International Edition*, vol. 62, no. 51, p. e202313746, 2023, doi: 10.1002/anie.202313746.
[258] P. Li, R. Li, Y. Liu, M. Xie, Z. Jin, and G. Yu, "Pulsed Nitrate-to-Ammonia Electroreduction Facilitated by Tandem Catalysis of Nitrite Intermediates," *J. Am. Chem. Soc.*, vol. 145, no. 11, pp. 6471–6479, Mar. 2023, doi: 10.1021/jacs.3c00334.
[259] O. Q. Carvalho *et al.*, "Role of Electronic Structure on Nitrate Reduction to Ammonium: A Periodic Journey," *J. Am. Chem. Soc.*, vol. 144, no. 32, pp. 14809–14818, Aug. 2022, doi: 10.1021/jacs.2c05673.
[260] H. Liu *et al.*, "Low-Coordination Rhodium Catalysts for an Efficient Electrochemical Nitrate Reduction to Ammonia," *ACS Catal.*, pp. 1513–1521, Jan. 2023, doi: 10.1021/acscatal.2c03004.

[261] L. Chen *et al.*, “Electrochemical Reduction of CO2 at Metal Electrodes in a Distillable Ionic Liquid,” *ChemSusChem*, vol. 9, no. 11, pp. 1271–1278, 2016, doi: 10.1002/cssc.201600359.
[262] L. Chen, F. Li, C. L. Bentley, M. Horne, A. M. Bond, and J. Zhang, “Electrochemical Reduction of CO2 with an Oxide-Derived Lead Nano-Coralline Electrode in Dimcarb,” *ChemElectroChem*, vol. 4, no. 6, pp. 1402–1410, 2017, doi: 10.1002/celc.201700217.
[263] K. Jiang *et al.*, “Metal ion cycling of Cu foil for selective C–C coupling in electrochemical CO2 reduction,” *Nat Catal*, vol. 1, no. 2, pp. 111–119, Feb. 2018, doi: 10.1038/s41929-017-0009-x.
[264] N. Benzbiria, M. Zertoubi, and M. Azzi, “Influence of copper surface pretreatment on the kinetics of oxygen reduction reaction in 0.5 M NaCl solution: Surface characterization and electrochemical studies,” *Applied Surface Science Advances*, vol. 4, p. 100069, Jun. 2021, doi: 10.1016/j.apsadv.2021.100069.
[265] N. Zhou, Z. Wang, N. Zhang, D. Bao, H. Zhong, and X. Zhang, “Potential-Induced Synthesis and Structural Identification of Oxide-Derived Cu Electrocatalysts for Selective Nitrate Reduction to Ammonia,” *ACS Catal.*, vol. 13, no. 11, pp. 7529–7537, Jun. 2023, doi: 10.1021/acscatal.3c01315.
[266] Y. Bu, C. Wang, W. Zhang, X. Yang, J. Ding, and G. Gao, “Electrical Pulse-Driven Periodic Self-Repair of Cu-Ni Tandem Catalyst for Efficient Ammonia Synthesis from Nitrate,” *Angewandte Chemie International Edition*, vol. 62, no. 24, p. e202217337, 2023, doi: 10.1002/anie.202217337.
[267] Y. Huang *et al.*, “Pulsed electroreduction of low-concentration nitrate to ammonia,” *Nat Commun*, vol. 14, no. 1, p. 7368, Nov. 2023, doi: 10.1038/s41467-023-43179-1.
[268] T. H. Wan, M. Saccoccio, C. Chen, and F. Ciucci, “Influence of the Discretization Methods on the Distribution of Relaxation Times Deconvolution: Implementing Radial Basis Functions with DRTtools,” *Electrochimica Acta*, vol. 184, pp. 483–499, Dec. 2015, doi: 10.1016/j.electacta.2015.09.097.
[269] B. Gupta, N. Kumar, K. Panda, V. Kanan, S. Joshi, and I. Visoly-Fisher, “Role of oxygen functional groups in reduced graphene oxide for lubrication,” *Sci Rep*, vol. 7, no. 1, Art. no. 1, Mar. 2017, doi: 10.1038/srep45030.
[270] L. Stobinski *et al.*, “Graphene oxide and reduced graphene oxide studied by the XRD, TEM and electron spectroscopy methods,” *Journal of Electron Spectroscopy and Related Phenomena*, vol. 195, pp. 145–154, Aug. 2014, doi: 10.1016/j.elspec.2014.07.003.
[271] M. Rashad, M. Rüsing, G. Berth, K. Lischka, and A. Pawlis, “CuO and Co3O4 Nanoparticles: Synthesis, Characterizations, and Raman Spectroscopy,” *Journal of Nanomaterials*, vol. 2013, no. 1, p. 714853, 2013, doi: 10.1155/2013/714853.
[272] C. Wang, S. Hu, X. Han, W. Huang, and L. Tian, “Controlled Synthesis and Microwave Absorption Property of Chain-Like Co Flower,” *PLOS ONE*, vol. 8, no. 2, p. e55928, Feb. 2013, doi: 10.1371/journal.pone.0055928.
[273] D. K. Bora, X. Cheng, M. Kapilashrami, P. A. Glans, Y. Luo, and J.-H. Guo, “Influence of crystal structure, ligand environment and morphology on Co L-edge XAS spectral characteristics in cobalt compounds,” *Journal of Synchrotron Radiation*, vol. 22, no. 6, pp. 1450–1458, Nov. 2015, doi: 10.1107/S1600577515017178.

[274] W. A. I. Goddard and C. B. I. Musgrave, “Electrochemical Nitrate Reduction Catalyzed by Two-Dimensional Transition Metal Borides,” *J. Phys. Chem. Lett.*, vol. 15, no. 7, pp. 1899–1907, Feb. 2024, doi: 10.1021/acs.jpclett.4c00054.
[275] Y. Tong *et al.*, “Spin-State Regulation of Perovskite Cobaltite to Realize Enhanced Oxygen Evolution Activity,” *Chem*, vol. 3, no. 5, pp. 812–821, Nov. 2017, doi: 10.1016/j.chempr.2017.09.003.
[276] A. Mikhailov *et al.*, “N, O and F K-edges XAS and DFT combination for the exploration of linkage isomers of coordinated nitric oxide in a ruthenium nitrosyl complex”.
[277] D. A. Harrington and B. E. Conway, “ac Impedance of Faradaic reactions involving electrosorbed intermediates—I. Kinetic theory,” *Electrochimica Acta*, vol. 32, no. 12, pp. 1703–1712, Dec. 1987, doi: 10.1016/0013-4686(87)80005-1.
[278] A. E. Bolzán and L. M. Gassa, “Comparative EIS study of the adsorption and electro-oxidation of thiourea and tetramethylthiourea on gold electrodes,” *J Appl Electrochem*, vol. 44, no. 2, pp. 279–292, Feb. 2014, doi: 10.1007/s10800-013-0621-7.
[279] H. Liu *et al.*, “Electrocatalytic Nitrate Reduction on Oxide-Derived Silver with Tunable Selectivity to Nitrite and Ammonia,” *ACS Catal.*, vol. 11, no. 14, pp. 8431–8442, Jul. 2021, doi: 10.1021/acscatal.1c01525.
[280] S. Feliu, “Electrochemical Impedance Spectroscopy for the Measurement of the Corrosion Rate of Magnesium Alloys: Brief Review and Challenges,” *Metals*, vol. 10, no. 6, Art. no. 6, Jun. 2020, doi: 10.3390/met10060775.
[281] C. Li, Z. Peng, and J. Huang, “Impedance Response of Electrochemical Interfaces: Part IV─Low-Frequency Inductive Loop for a Single-Electron Reaction,” *J. Phys. Chem. C*, vol. 127, no. 33, pp. 16367–16373, Aug. 2023, doi: 10.1021/acs.jpcc.3c02830.